

Final Report

Laboratory and Numerical Investigation of Hydraulic Fracture Propagation and Permeability Evolution in Heterogeneous and Anisotropic Shale

FWP ESD 14084

Principal Investigator: Seiji Nakagawa, (510) 486-7894, snakagawa@lbl.gov

Co.-PI: Jonny Rutqvist
Tim Kneafsey
Kunhwi Kim
Jens Birkholzer
Hele Prieto
Lawrence Berkeley National Laboratory

Submitted to:
U.S. Department of Energy
National Energy Technology Laboratory
DOE Project Manager: Stephen Henry
Phone: (304) 285-2083
Email Stephen.Henry@netl.doe.gov

Table of Contents

- 1. Executive Summary..... 8
- 2. Project Accomplishments 9
 - 2.1 Task 2.0 Laboratory Experiments..... 9
 - 2.1.1 Subtask 2.1–Preparation of true triaxial test setups (Phase I) 9
 - 2.1.2 Subtask 2.2–Preparation of rock samples containing complex heterogeneities (Phase I)..... 12
 - 2.1.3 Subtask 2.3–Preliminary hydraulic fracturing experiment (Phase I) 14
 - 2.1.4 Subtask 2.4– Hydraulic fracturing visualization I: Stress and texture anisotropy effect (Phase II) 27
 - 2.1.5 Subtask 2.4– Hydraulic fracturing visualization II: Fluid viscosity/injection rate effect 41
 - 2.1.6 Final remarks on the laboratory experiments 51
 - 2.2 Task 3.0 Numerical Modeling 54
 - 2.2.1 Subtask 3.1–Code modification and verification of TOUGH-RBSN hydraulic fracturing algorithms (Phase I) 54
 - 2.2.2 Subtask 3.2–Numerical model setup and preliminary simulation of complex hydraulic fracturing (Phase I)..... 56
 - 2.2.3 Subtask 3.3–Model prediction of laboratory hydraulic fracturing experiments (Phase I) 60
 - 2.2.4 Subtask 3.4–Interpretative numerical modeling of laboratory experiments (Phase II) 61
 - 2.2.5 Subtask 3.5 – Simulation of Mont Terri Hydraulic Fracturing Experiment (Phase II) 66
 - 2.3 Task 4.0 – Final Synthesis of Experimental and Numerical Modeling Results (Phase II) 74
 - 2.3.1 General remarks on the agreement and discrepancies between the laboratory experiments and numerical modeling 74
 - 2.3.2 Remarks on fluid injection rate and hydraulic fracturing 75
 - 2.3.3 Remarks on the scaling—Applying laboratory experiments to the field, and changing scales in the numerical modeling..... 75
 - 2.3.4 Remarks on fluid-sensitivity and swelling of shale 76
- 3. Publications and presentations (incl. planned)..... 77
- 4. Budget summary..... 77
- 5. References 78

List of Figures

Figure 2.1. A polyaxial (true-triaxial) loading system for optical hydraulic fracturing visualization. A transparent sample containing preexisting fractures is used. For the 2.5D fracture network model shown here, the fractures can be illuminated using a laser sheet to improve the visibility.....	10
Figure 2.2. Reassembled and modified portable, X-ray transparent (through a window) true-triaxial test cell. From the left, a rectangular, fractured glass sample surrounded by modified platens (a), jacketed sample with attached loading buttons (b), and assembled cell for leak/X-ray transparency testing (c)...	10
Figure 2.3. Old (left) and new (right) loading platens. The internal platens were modified to reduce excessive platen flexures during application of load using side pistons in the setup.	11
Figure 2.4. X-ray scanning test of the test cell. Because of the low energy of the medical X-ray CT machine, steel sections and parts (except for the small fitting) of the cell are mostly opaque. However, the section between the two reaction rings provides a “window” for monitoring the growth of hydraulic fractures during the experiment.....	11
Figure 2.5. X-ray tomography images of the sample section. Through the “window,” the sample inside the cell is visible. Note that the black circle at the center of the rectangular sample is an analogue borehole. Very thin preexisting fractures in the glass block, however, are largely not visible, because of the resolution of the equipment (CT boxel size ~0.5mm).	12
Figure 2.6. Three different techniques for producing preexisting fractures in rock/analogue rock samples.	13
Figure 2.7. The sample preparation technique using the glass heating/cooling has been used to produce heterogeneous samples for the tests using the portable true-triaxial cell with X-ray CT imaging (a). The density and strength of the fractures in glass samples can be varied by changing the temperature difference during the initial fracturing, and the heating temperature and the duration of the subsequent reheating (b, samples in the rear rows).....	14
Figure 2.8. Visualization of hydraulic fracturing within a glass cube containing a network of model fractures.....	14
Figure 2.9. Non-planar geometry of hydraulic fractures produced in a fractured reservoir model in a glass cube. The fracture orientation, generally, is in the maximal principal stress direction, as expected.	15
Figure 2.10. Pre-cracking of a borehole using a mechanical loading technique	15
Figure 2.11. Motor-driven, miniature high-pressure fluid injection device (initial model).....	16
Figure 2.12. Improved, lower-speed system with a fluid-volume measurement capability.....	16
Figure 2.13. Liquid metal injection experiments into intact glass cubes for visualization of controlled hydraulic fracture growth	16
Figure 2.14. Pressure histories during hydraulic fracturing experiments. The pump rate (given in V) is not calibrated to actual flow rates. The size of the pre-induced crack (flaw) determines the breakdown pressure as well as the pressure decline rate which is related to the speed of fracture propagation. Note that the pressure drop in an intact sample (a) is instantaneous.....	17
Figure 2.15. Reduced-speed fracture growths in Sample #7. The total growth time is ~20 seconds.	18

Figure 2.16. Pressure histories during a hydraulic fracturing experiment with glycerol. The pump rate (given in V) is not calibrated to actual flow rate. Compared to the low-viscosity-fracturing fluid results in Figure 2.14, fracture propagation is much slower, and the peak injection pressure (breakdown pressure) higher. The flaw size was similar to the medium-size flaws in Test#7. 18

Figure 2.17. (Enhanced) Visual images of hydraulic fracture growth during the experiment. The total sequence here is ~20 seconds. The fracture front is barely visible. 19

Figure 2.18. Images of hydraulic fractures after the experiment. At shallow angles, the hydraulic fractures can be easily seen (a,b). In contrast, from the direction near-perpendicular to the fracture plane, they are hardly visible (c). 19

Figure 2.19. Enhanced visualization of hydraulically produced fractures using a glycerol-sulforhodamine B mixture. 19

Figure 2.20. Enhanced visualization of hydraulically produced fractures using a glycerol-sulforhodamine B mixture. 20

Figure 2.21. Top (left) and side (right) images of hydraulic fracturing in an intact glass cube subjected to anisotropic stress. Green-blue light was introduced in the glass cube, resulting in fluorescence of sulforhodamine B dissolved in glycerol. Thanks to the high viscosity of the fracturing fluid (~1,100 cP) and very small fracture aperture, the experiment time is very long. 21

Figure 2.22. Time-injection pressure/volume history (left) and pressure-injection volume (right) results for hydraulic fracturing of an intact block. 22

Figure 2.23. Laser-sheet-assisted visualization of hydraulic fracturing in a sample containing a 3D-laser-etched fractured reservoir model. The image above is a reflection of a sample being tested within a true-triaxial loading frame, in a diagonal mirror embedded on a transparent loading block. 22

Figure 2.24. Before and after images of prefractured glass block injected with liquid metal (the silver-colored fluid in the images). Although optically visible, the fractures injected with the metal did not appear clearly in the X-ray CT images. 23

Figure 2.25. X-ray CT images during a hydraulic fracturing experiment inside a true-triaxial cell, with a liquid-metal injection fluid (only the slices at one location are shown, although the actual images was conducted for a 1.3-inch wide strip). Although the fluid was injected into the fractures and leaked to the outer surface of the prefractured glass block, the fluid within the fractures was not visible due to poor signal-to-noise ratio of the images. 24

Figure 2.26. Three orthogonal X-ray CT cross sections of a thermally fractured block. The color look up table is inverted from normal, thus bright here indicates low density. 25

Figure 2.27. Fractures from Figure 2.26 extracted using Connected Component Analysis. 25

Figure 2.28. X-ray CT images of Mancos shale block (cutting through the sample in-and-out of the paper) with failed attempts to drill 1/8"-dia analogue boreholes. Broken bits can be seen as bright white spots (high density) at the ends of the incomplete, blind holes. Numerous pervasive fractures were also produced in the process. 26

Figure 2.29. Mancos shale block prepared for hydraulic fracturing experiment using liquid metal (left). The sample leaked the fluid during the pre-experiment fluid injection stage. X-ray CT images (center and right) show the fluid penetrated into drilling-induced fractures and, possibly, preexisting shrinkage fractures. 27

Figure 2.30. Stress and texture anisotropy and hydraulic fracturing orientations. In the “Previous test,” the maximum horizontal stress was applied in the horizontal direction (a) while in the “New test,” it was applied in the vertical direction in the images (b). (Note that these would be top-down views of the samples during the experiment.) Although the fracture orientations were not well defined in the previous test (possibly because of uneven application of confining stress), in both cases, the fracture orientations align with the direction of the maximum horizontal stress. 28

Figure 2.31. Principal stresses with respect to the bedding plane texture of a Mancos Shale block used for the hydraulic fracturing/X-ray CT imaging experiment..... 29

Figure 2.32. Experiment in progress. A rectangular block is surrounded by aluminum platens to form a cylindrical sample (upper left) which is jacketed and installed in the true-triaxial vessel (upper right and lower left). During the experiment, three principal stresses, injection pressure, and injected fluid volume are monitored (lower right). 29

Figure 2.33. Injection pressure and volume during a hydraulic fracturing experiment in a true-triaxial cell 30

Figure 2.34. View perspectives. 31

Figure 2.35. Three-direction views of scans 10-17 showing fracture pressures increasing from 334 to 1860 through Scan 15 (first 6 images) and decreasing to 1118 psi over the last two scans..... 32

Figure 2.36. Correlated results for the hydraulic fracturing test (pressure vs. injection volume) and the X-ray CT images. 33

Figure 2.37. Mancos Shale block after a hydraulic fracture visualization experiment. The four sides of the block are shown. The fracture propagated along the bedding planes, but also along some of the preexisting fractures. 34

Figure 2.38. Top (left) and side (right) images of hydraulic fracturing in a glass cube containing “standard” fracture model injected with high-viscosity fluid. 35

Figure 2.39. Top (left) and side (right) images of hydraulic fracturing in a glass cube containing “tall” fracture model injected with high-viscosity fluid. 36

Figure 2.40. Fracturing of a “standard” height fractured reservoir model (H=0.25”). Hydraulic fractures are mostly propagating within intact matrix. The preexisting fractures are activated when the hydraulic fracture encounter a preexisting fracture at a shallow angle (see upper branch). Some high-angle fractures, however, were also activated but are not extensive. 37

Figure 2.41. Fracturing of a “tall” fractured reservoir model (H=0.5”). Hydraulic fractures primarily followed the preexisting fractures. Note that the isolated fracture in near the bottom was in fact connected to the near-borehole part of the hydraulic fracture via fractures in the intact part of the sample surrounding the fractured layer. 37

Figure 2.42. Time-injection pressure/volume history (left column) and pressure-injection volume (right column) results for hydraulic fracturing of an intact block. The top row is for the “standard height” fractures (a), and the bottom row is for the “tall” fractures (b). The injection volume record is irregular because of a slipped displacement sensor. 38

Figure 2.43. Interactions between hydraulic fractures (in red fluorescent light from the injected glycerol). All the experiments were conducted under anisotropic stress (4.8 MPa/7.2 MPa/9.6 MPa) and with an injection rate of 0.425 $\mu\text{L}/\text{min}$ 39

Figure 2.44. Top (left) and side (right) images of hydraulic fracturing in a glass cube containing “weaker” fracture model injected with high-viscosity fluid. 40

Figure 2.45. Fracturing of a “weaker” fractured reservoir model. (Compare to the “standard” model in Figure 2.40.) 41

Figure 2.46. Time-injection pressure/volume history (left) and pressure-injection volume (right) results for hydraulic fracturing of a block containing “weaker” fractures. 41

Figure 2.47. Top (left) and side (right) images of hydraulic fracturing in a glass cube containing “standard” fracture model injected with low-viscosity fluid (water). Because of the small refraction index contrast, the induced fractures are difficult to see, particularly for the side views. 42

Figure 2.48. Because of the lack of (or very weak) fluorescence, the hydraulic fracture cannot be color tagged. However, from the differences in the brightness of the laser-illuminated, pre-existing fracture patterns, it can be seen that the hydraulic fracture was not affected by the preexisting fractures..... 43

Figure 2.49. Time-injection pressure/volume history (left) and pressure-injection volume (right) results for hydraulic fracturing of a block containing “standard” fractures injected with water. 43

Figure 2.50. Top (left) and side (right) images of hydraulic fracturing in a glass cube containing “standard” fracture model injected with low-viscosity fluid (water). The speed of injection was approximately 30 times faster than the case shown in Figure 2.38. 44

Figure 2.51. Fracturing of a “standard” fractured reservoir model at a fast injection rate. (Compare to the “standard” model in Figure 2.40.) The induced hydraulic fracture was not affected by the preexisting fractures at all. 45

Figure 2.52. At early times during fast injection of highly viscous fluid (right), a (near-)vacuum-filled zone behind the fracture front can be seen, preceding the fluid front. This zone was not observed for slower injection of the same fluid (left). 45

Figure 2.53. Time-injection pressure/volume history (left) and pressure-injection volume (right) results for hydraulic fracturing of a block containing “standard” fractures, with fast (30x) injection of glycerol 46

Figure 2.54. Randomly fractured soda-lime glass cube samples. The temperature values indicate the re-heating temperature of original blocks which had a similar population of contraction-induced fractures. 46

Figure 2.55. Randomly fractured soda-lime glass cube samples. The temperature values indicate the re-heating temperature of original blocks which had a similar population of contraction-induced fractures. 47

Figure 2.56. Injection pressure-volume relationships measured in various tests. The “slow” injection test was conducted at a rate of 0.425 $\mu\text{L}/\text{min}$, while the “fast” injection test was conducted at 20 times that rate. 48

Figure 2.57. Observed hydraulically induced fracture images enhanced by fluorescence induced by long-wavelength UV light. 48

Figure 2.58. Hydraulic fracturing within “weak” fractured block. Different fracturing behavior in glass samples containing fracture networks with similar fracture properties, subjected to either “slow” or “fast” injection of fracturing fluid. Sample with fast injection, which exhibited well-defined, flat hydraulic fractures, showed planar fracture fronts which were not filled with the fracturing fluid. 49

Figure 2.59. Possible mechanisms for the different fracturing behavior cause by slow and fast injection. The low fluid pressure near the leading edge of propagating hydraulic fractures may fail to activate the weak, preexisting interfaces (fractures), resulting in “crossing” of the hydraulic fractures across the interfaces and continued fracturing of the intact matrix. 49

Figure 2.60. A 12-channel acoustic emission monitoring system (AMSY-6, Vallen Systems) integrated with the true-triaxial hydraulic fracturing visualization system. 50

Figure 2.61. Acoustic emission count history for the “fast” injection experiment. The AE events are grouped by time with 150 s intervals. 51

Figure 2.62 Correlated views of AE locations (top) and the visualized images of hydraulic fracturing in both top view (middle row) (similar angle of view as the AE plots) and side view (bottom row). 51

Figure 2.63 Platen displacements correlated with the hydraulic fracturing of “strong” block by “fast injection” (same as the sample used in Figure 2.62). Note that the platen displacements are very small (less than 0.5 microns for the 10cm cube sample) and the data is very noisy. The original data also contained strong drifts in time, which were corrected in this figure. 53

Figure 3.1. Uniaxial compression tests: a) schematic drawing for the test program; and b) stress-strain curves with various orientations of bedding plane with regard to the loading axis. 55

Figure 3.2. Fracture patterns in deformed shapes of the model. Note that the mesh geometry is identical, but the bedding orientation is internally changed in the simulations. 55

Figure 3.3. KGD model test: a) model set up; and b) aperture width profiles along the fracture. 56

Figure 3.4. Initial demonstration model simulations of fracture propagation through a discrete fracture network..... 57

Figure 3.5. a) Discrete fracture network of a glass sample; and mapping of the fracture geometry onto unstructured Voronoi grid with different mesh density: b) 5000 cells and c) 10000 cells, approximately. 57

Figure 3.6. a) hydraulic fracturing which mostly follows the pre-existing fractures; and b) contour plot of pressure distribution at the same time step. 59

Figure 3.7. Pressure evolution at the borehole with different compressibility coefficients for the borehole domain. Note that the other parameters and conditions are identical in these two cases. 59

Figure 3.8. Introduction of initial notches around the borehole. The location of the notches was determined by the resulting hydraulic fractures (illustrated by red lines) without notch..... 60

Figure 3.9. Comparison of pressure evolutions according to the presence of the initial notches..... 61

Figure 3.10 Pressure evolutions at the borehole for different fluid injections. 63

Figure 3.11 Contour plots of pressure distributions: a) glycerol injection; b) water injection. 64

Figure 3.12 Hydraulic fracture patterns: a) glycerol injection; b) water injection. 65

Figure 3.13. Schematic of a penny-shaped propagating fracture according to Geertsma and de Klerk (1969). 67

Figure 3.14. (a) Borehole layout at the GP-A/GS experiment and (b) pressure responses in the injection borehole section (BGS2-Z2) and the monitoring borehole section (BGS1-Z1) during breakdown and two reopening cycles (Enachescu et al. 2002). 67

Figure 3.15. Evolution of pressure in BGS2-Z2 (injection interval) and deformations in BGS3 and BGS4 during breakdown and two reopening cycles (Enachescu et al. 2002).	68
Figure 3.16. Details of pressure and deformation responses in the injection borehole BGS2 and the monitoring boreholes BGS1, BGS3 and BGS4 from Daneshy et al. (2004) here with some comments added.	69
Figure 3.17. Pressure and aperture profiles constructed from the information in Figure 3.16.....	70
Figure 3.18. Empirical relation between injection volume and fracture length based on penny-shaped fracture mechanics model and observations at the GP-A/GS experiments.	71
Figure 3.19. Conceptual model of possible cross-bedding fracture propagation at the GP-A/GS experiment (Daneshy et al. 2004).....	71
Figure 3.20. TOUGH-RBSN modeling of intermediate scale fracture propagation through an anisotropic medium. Dashed line shows direction of bedding planes. The injection rate is 10 time higher for the results shown in (a).	72
Figure 3.21. (a) Model discretization with prescription of discontinuities; (b) Resulting hydraulic fracture propagation overlaid onto the Voronoi grid.....	73
Figure 4.1. Swelling and fracture closure in a pre-fractured Opalinus Clay core sample. X-ray images of core cross sections are shown. Core length=4 inches (10.24 cm). The injected fluid is a synthetic in-situ brine. The vertical fractures in the core (which did not close in the after-injection images) are filled with epoxy (which do not show in the X-ray images because of its low density).	76

List of Tables

Table 2.1. CT operational parameters.	31
Table 2.2. Scan times and experiment conditions.....	31
Table 2.3. Assessment of permeability changes.....	53
Table 3.1 Hydrological properties of matrix, fracture, and borehole domains.....	62
Table 4.1. An example of matched experimental conditions at different scales.....	76

1. Executive Summary

For efficient and economical production of oil and gas from low-permeability rock, reservoir stimulation using hydraulic fracturing needs to take advantage of preexisting natural fractures to increase their drainage footprint. Both open and sealed fractures as well as other heterogeneities, such as inclusions and mineral grain boundaries, and anisotropy of the rock fabric play vital roles, because these features interfere with the propagation of hydraulic fractures, causing kinking and branching, and resulting in a complex fracture network. The primary objectives of the project are (1) to improve understanding of how initial rock heterogeneity affects the dynamic and static properties of hydraulically induced fractures and (2) to improve and develop tested capability for numerically simulating coupled flow and fracture propagation processes.

To meet these goals, this project performed a combination of laboratory visualization (optically and/or using X-ray CT) experiments of hydraulic fracturing and numerical modeling of the coupled mechanical hydrological processes. The experiments were conducted on natural (shale) and analogue rock samples (soda-lime glass) with preexisting cracks and layers. The experimental work was integrated with numerical modeling using LBNL's hybrid TOUGH-RBSN (RBSN=Rigid-Body-Spring-Network) Code which is well suited for problems involving dynamic fracture propagation in response to fluid injection. To upscale the effects observed at the core scale to the small field scale, the code was also applied to simulate the in-situ hydraulic fracturing experiments conducted at the Mont Terri underground research laboratory in Switzerland. Through these research tasks, the project aims to produce quantitative experimental data including visual images of complex hydraulic fracturing at the laboratory scale and predictive numerical simulation capability which is validated by the laboratory data and available field data.

The 1.5-year project produced a number of new experimental techniques and data, and numerical simulation tools for coupled mechanical-hydrological behavior of rock containing discrete fractures. The key products of the experimental research are: (1) different techniques for producing artificial pre-fractured natural and analogue rock samples; (2) experimental setups for laboratory hydraulic fracturing under the true-triaxial stress state; (3) optical visualization techniques and the experimental results, including enhancement method using fluorescent dye and laser light; (4) experimental setups for seismic (acoustic emission) monitoring and the test results correlated with optical visualization; (5) X-ray CT images of hydraulic fracturing in heterogeneous and anisotropic shale samples. The main products of the numerical modeling effort are: (1) a TOUGH-RBSN code for hydraulic fracturing problems; (2) simulation capability and modeling method for strongly anisotropic rocks (such as shale); (3) comparison of model-predicted hydraulic fractures and laboratory fractures for the same background fracture geometry.

In this final report, we provide a description of the results obtained in this project, including the most recent progresses made in the final reporting period (FY16 Q2 January 1 through March 31).

2. Project Accomplishments

In the following, we will describe the experimental and numerical methods and tools developed in this project, and the obtained results. Although most of these results have been previously reported in the quarterly and annual reports, we will include them here for completeness. Newly obtained results during the final reporting period (FY16 Q2 January 1 through March 31) are also included. These are:

- X-ray CT imaging of hydraulic fracture growth in shale sample (Subtask 2.4, Milestone M6),
- Further analysis of Mont Terri in-situ hydraulic fracture field experiments and TOUGH-RBSN simulations (Subtask 3.4),
- Synthesis of laboratory experiments and numerical modeling (Task 4.0, Milestone M9),

with which we meet all the project milestones.

2.1 Task 2.0 Laboratory Experiments

The laboratory experiments use optical or real-time X-ray CT imaging to examine the evolution of hydraulic fractures in heterogeneous rock (and rock analogues) in the laboratory. In the Phase I of the project, we developed methods for fabricating test samples containing preexisting fractures with precise geometry and samples with fractures with a random fracture network with more complex geometry. We also developed methods for enhancing the optical images of hydraulic fractures based upon fluorescent dye injection combined with UV/laser illumination. True-triaxial loading systems for both optical visualization and X-ray CT imaging were assembled, then used in Phase II for conducting optical and X-ray CT visualization of hydraulic fracturing in transparent glass samples and natural shale samples.

2.1.1 Subtask 2.1–Preparation of true triaxial test setups (Phase I)

For the optical visualization tests, we used a polyaxial loading frame with three sets of perpendicular hydraulic rams. Spacer plates required for the testing were fabricated of both alloy steel and acrylic, with proper dimensions for our samples. We also fabricated a series of transparent acrylic block containing a diagonal mirror. When used as a loading platen at the top of a transparent sample, the block provides an image of fractures viewed from the top (Figure 2.1). Additionally, using a port hole in the side load frame, the sample can also viewed from the side through a transparent, acrylic side-loading block. The system was fitted with a linear laser illumination (line pattern can be generated via diffraction gratings) which improved visibility of 2.5D fracture model within a transparent soda-lime glass cube. Later, this visualization setup was upgraded using fluorescent dye visual enhancement and concurrent AE monitoring.

For the X-ray CT visualization within a triaxial pressure vessel, we reassembled our existing test system that allows application of three independent principal stresses (Figure 2.2). During the process, we realized that the aluminum loading platens previously used for borehole breakout and sanding study in weakly cemented sand may be too compliant to be used for stiff rocks including shales. To reduce the flexures of the loading platens, we redesigned and fabricated platens that are 50% thicker than the originals (Figure 2.3). Although this slightly reduces the size of rectangular samples used in the experiments from 3"×3"×6" to 2.5"×2.5"×6," we decided the modification was necessary.

Using the modified setup, we conducted an initial leak test on a rectangular, fractured glass block with a center borehole shown in Figure 2.2. The sample was jacketed and installed in the cell, and confining pressure of 1,000 psi and axial stress of 1,000 psi were applied. Additionally, side pistons applied 1,000 psi of extra stress to the sample in the vertical direction. The test confirmed that the leak from the system was negligible. One issue that was identified during the test was excess slips of the aluminum platens along the nylon sheets on the sample. These sheets were inserted to reduce the friction between a sample and the platens, but small differences in the piston forces resulted in uneven displacements among the lateral pistons and in excess lateral slip of the platens. This problem was solved by using a thin, soft rubber sheet on the sides of the plates on which the maximum principal stress was applied through the miniature pistons.

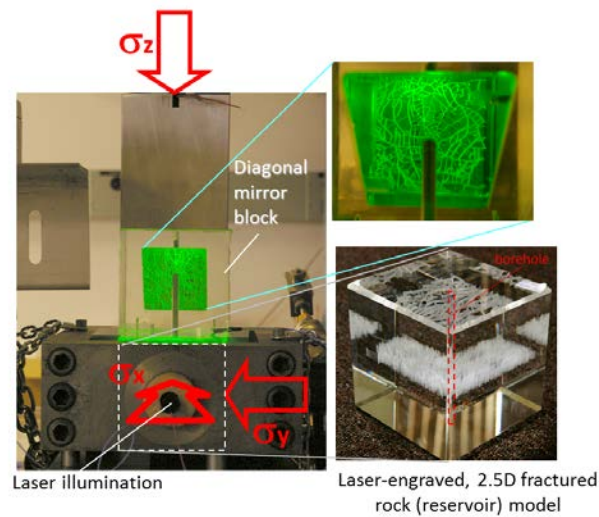


Figure 2.1. A polyaxial (true-triaxial) loading system for optical hydraulic fracturing visualization. A transparent sample containing preexisting fractures is used. For the 2.5D fracture network model shown here, the fractures can be illuminated using a laser sheet to improve the visibility.

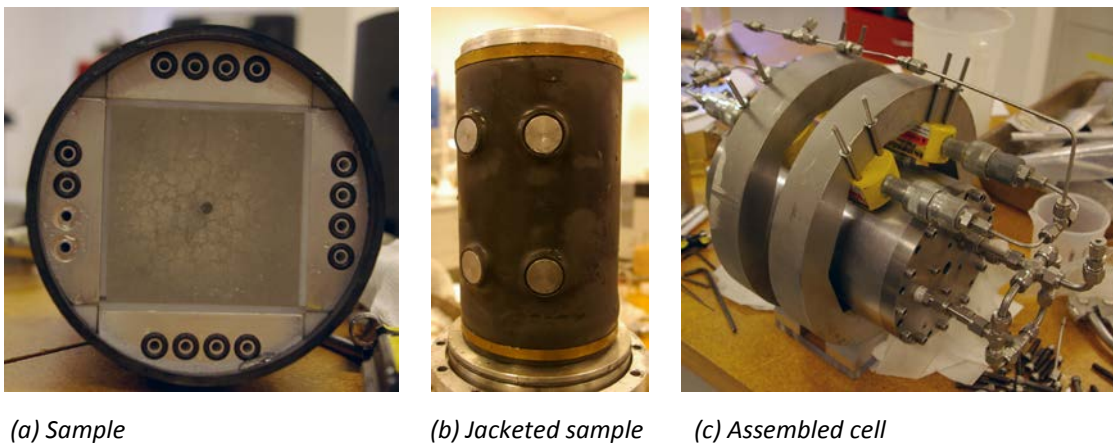


Figure 2.2. Reassembled and modified portable, X-ray transparent (through a window) true-triaxial test cell. From the left, a rectangular, fractured glass sample surrounded by modified platens (a), jacketed sample with attached loading buttons (b), and assembled cell for leak/X-ray transparency testing (c).

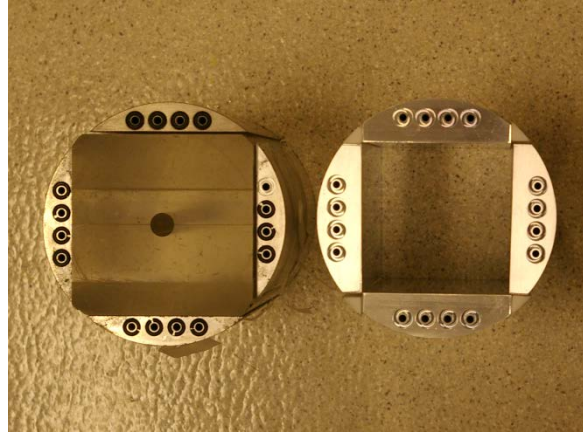


Figure 2.3. Old (left) and new (right) loading platens. The internal platens were modified to reduce excessive platen flexures during application of load using side pistons in the setup.

Once the leak test was completed, we conducted X-ray CT scans to check the visibility of the sample in the cell (Figure 2.4). With this setup, we cannot see the entire sample because the lateral steel frames block the X-ray. However, a part of the sample (about 1.3 inch wide middle section) can be imaged tomographically through a “window” between the two rings. Figure 2.5 shows a series of sequential image slices within this window, and a contrast-enhanced image for one of the slices. The sample containing a single borehole in the middle was clearly visualized. However, the very thin fractures in the sample (produced by heating and cooling of the glass block) were not apparent. This is primarily because the resolution of the medical X-ray CT machine is not sufficient for resolving the few-micron-thick fractures. During the hydraulic fracturing experiments, however, we will be using high-density fluids (metal) to enhance the contrast of the fracture image.

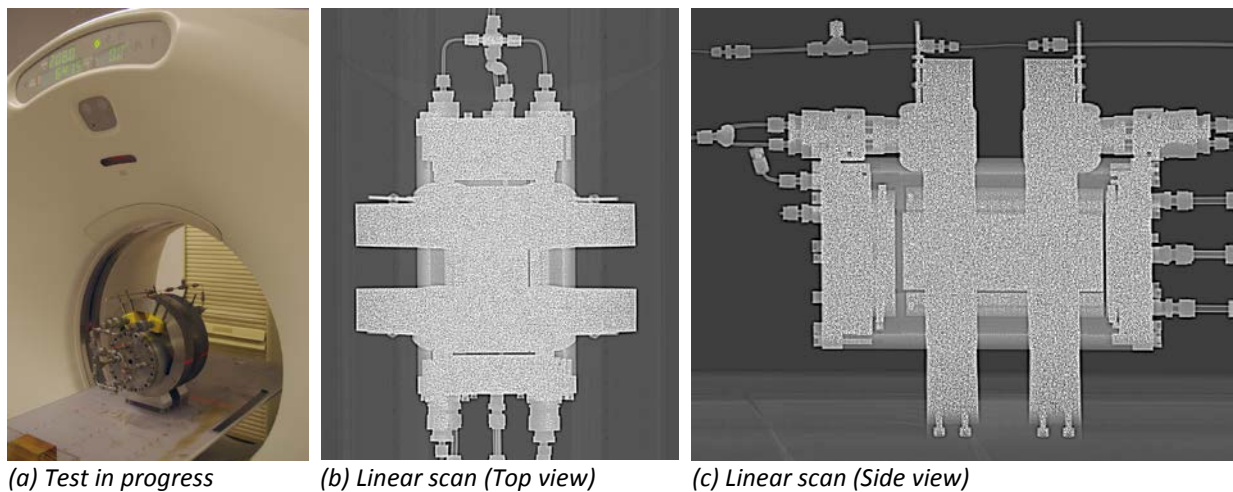


Figure 2.4. X-ray scanning test of the test cell. Because of the low energy of the medical X-ray CT machine, steel sections and parts (except for the small fitting) of the cell are mostly opaque. However, the section between the two reaction rings provides a “window” for monitoring the growth of hydraulic fractures during the experiment.

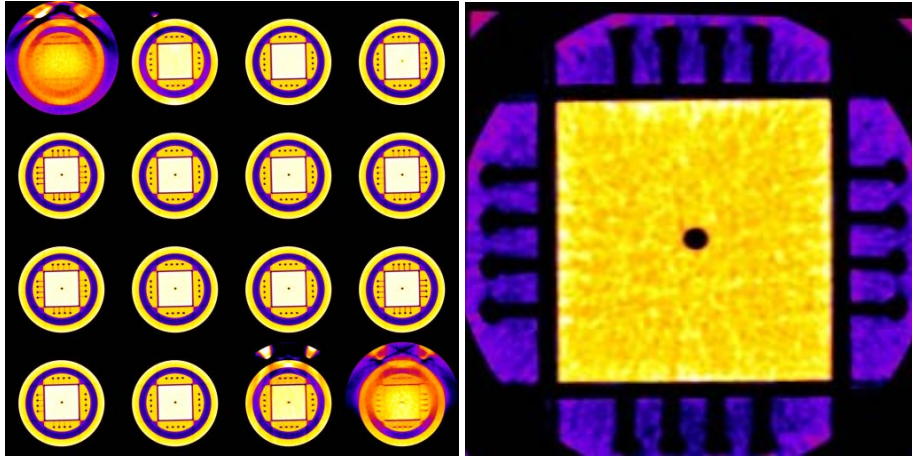


Figure 2.5. X-ray tomography images of the sample section. Through the “window,” the sample inside the cell is visible. Note that the black circle at the center of the rectangular sample is an analogue borehole. Very thin preexisting fractures in the glass block, however, are largely not visible, because of the resolution of the equipment (CT voxel size $\sim 0.5\text{mm}$).

2.1.2 Subtask 2.2–Preparation of rock samples containing complex heterogeneities (Phase I)

This task (1) developed and identified the methods for producing synthetic or natural rock samples containing heterogeneities, particularly in the form of preexisting fractures as in shales, and (2) fabricated samples for the experiments. The experiments conducted in this project required samples containing strong heterogeneities (cracks, inclusions, layers). Our initial attempt to produce such samples using a stack of fractured glass plates (as described in the SOPO) was not successful. Instead, we sought for alternate methods, and successfully developed/identified three possible techniques. Previously, we developed a method (procedure) for producing precisely designed and repeatable models for preexisting fractures in transparent soda-lime glass cubes using the 3D laser engraving technique. We also develop additional methods involving heating and cooling of glass and quartz-rich, polycrystalline rock (the latter was not used in this project, however). The additional methods were developed and samples produced, because we anticipated the needs for more complex and realistic fracture geometry than can be realized by the 3D laser-etching method. These three different techniques are described below.

a. 3D-laser engraved fractures (glass cubes): Figure 2.6a

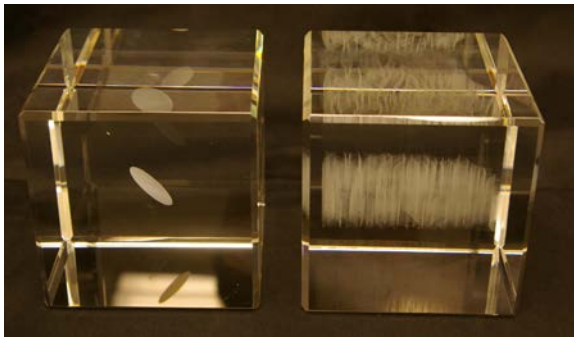
This method uses a focused laser beam to produced highly localized thermal expansions in a transparent solid. Because of large differential thermal strain, the laser induces a microscopic crack at a desired location in a 3D volume. By scanning the 3D space with the focal point of laser, following a pattern given to a computer program, fractures with desired and highly repeatable geometry can be produced. By altering the density of the microscopic cracks constituting the fracture, the tensile strength of the fracture can also be controlled in a repeatable fashion. We produced about a dozen of samples (transparent 4”x4”x4” cubes) containing a model fractured reservoir with different crack densities (fracture strength). Additionally, we produced several blocks containing a single, penny-shaped crack, for examining fracture propagation from a simple crack and for determining the strength of the fractures with different microcrack density.

b. Thermally produced fracture networks (glass cubes, rectangular blocks): Figure 2.6b

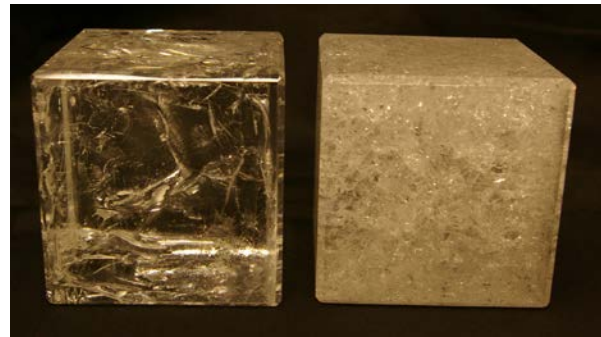
This method uses rapid thermal contraction of brittle glass samples to produce a chaotic, dense population of interconnected fractures. Through several tests, we found that the fracture density can be altered by changing the temperature of the samples before rapid cooling. Once the fractures are produced, the samples are re-heated above the annealing point so that the fractures are partially healed and the flow permeability is reduced (which also improves optical visibility of the fractures inside the sample).

c. Thermally produced microcracks (polycrystalline rocks): Figure 2.6c

This method involves heating of quartz-rich polycrystalline rock above the alpha-to-beta transition temperature of the quartz ($\sim 573^\circ\text{C}$ at 1 atm). In the past, this method was also used to examine the impact of microcracks in rock on seismic wave propagation. The process involves about $\sim 0.45\%$ of linear expansion in quartz crystals, resulting in intercrystalline microcracks in rock, which do not heal even after the temperature is lowered and a part (or most) of the quartz crystals undergo reverse transition. Additionally, this process is accompanied by the thermal cracking caused by different mineral types and orientations of anisotropic minerals. A granite cube treated by this process resulted in much lower seismic velocities than untreated cube, indicating enhanced grain-scale microcracks and heterogeneity.



(a) 3D laser engraved fractures



(b) Thermal-shrinkage-induced fractures



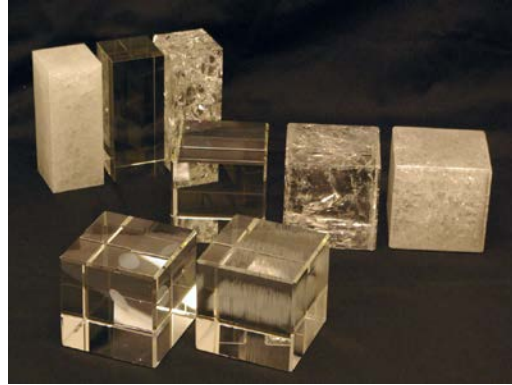
(c) Phase-transition-induced cracks in granite (block on the right was heated above the α - β quartz transition point)

Figure 2.6. Three different techniques for producing preexisting fractures in rock/analogue rock samples.

An assortment of the samples has been produced using these techniques, including slender, rectangular glass blocks containing fractures (one of these blocks was used in the leak test/X-ray transparency test of the portable true-triaxial test cell) (Figure 2.7).



(a) Long rectangular sample



(b) Assortment of glass samples

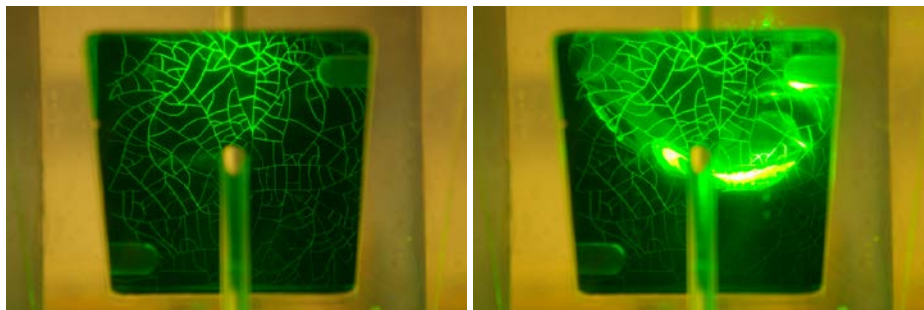
Figure 2.7. The sample preparation technique using the glass heating/cooling has been used to produce heterogeneous samples for the tests using the portable true-triaxial cell with X-ray CT imaging (a). The density and strength of the fractures in glass samples can be varied by changing the temperature difference during the initial fracturing, and the heating temperature and the duration of the subsequent reheating (b, samples in the rear rows).

2.1.3 Subtask 2.3–Preliminary hydraulic fracturing experiment (Phase I)

Optical visualization experiment

We first conducted optical visualization experiments using transparent, analogue fractured rock samples and intact glass blocks. These experiments were conducted using the true triaxial (polyaxial) loading system with a mirror and a viewing window, which was built in Subtask 2.1. During the experiments, a $\sim 4'' \times 4'' \times 4''$ (10cm \times 10 cm \times 10 cm) glass cube containing an analogue borehole (stainless steel tubing) with a diameter of 1/8'' was first subjected to principal stresses of 700 psi, 1,050 psi, and 1,400 psi (vertical). Subsequently, low-viscosity (~ 2 cP), high-stiffness liquid metal (Galinstan) was injected in the borehole, and a hydraulic fracture was created.

In the first experiment, we successfully observed the growth of hydraulic fractures within a glass cube containing a network of model fractures produced by the 3D laser engraving method (Figure 2.8). However, the propagation of the fractures was instantaneous, partly because the pump used for the injection (High Pressure Equipment Company pressure intensifier) resulted in too high compliance in the injection system, as indicated by the numerical modeling result. Additionally, uneven application of the stress resulted in non-planar geometry of the hydraulic fractures, which was probably not caused by the effect of the preexisting fractures (Figure 2.9).



(a) Before

(b) After

Figure 2.8. Visualization of hydraulic fracturing within a glass cube containing a network of model fractures

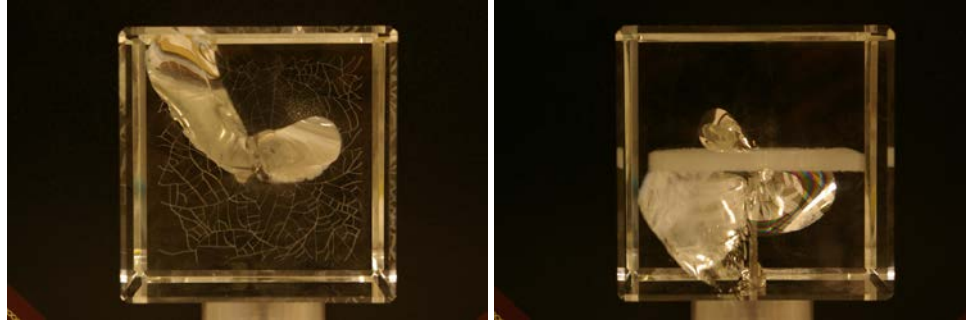


Figure 2.9. Non-planar geometry of hydraulic fractures produced in a fractured reservoir model in a glass cube. The fracture orientation, generally, is in the maximal principal stress direction, as expected.

In order to capture the growth of hydraulic fractures and visualize their interactions with preexisting fractures, the growth has to be stabilized and the rate of propagation reduced. We speculated that one of the reasons for the abrupt growth was the sudden release of strain energy in both fluid in the system and the solid around the borehole. These can be reduced by applying a pre-notch on the borehole wall to reduce the breakdown pressure. To test this idea, we fabricated a tool for inducing a small flaw at the bottom of a blind (bore) hole. This tool works by mechanically compressing a small rubber plug, which generates small, stable fractures by pressurizing the borehole wall. To some degree, the orientation of the flaw can be controlled by applying stress to the sample during the pressurization (Figure 2.10).

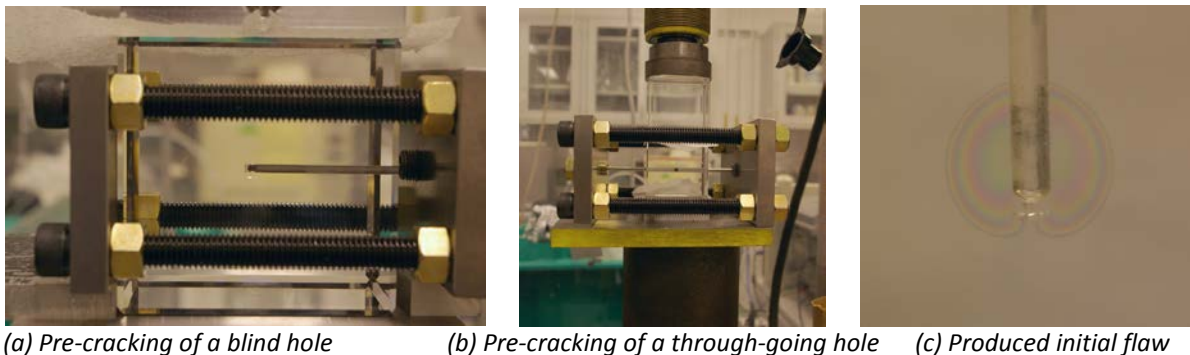


Figure 2.10. Pre-cracking of a borehole using a mechanical loading technique

In addition to the prefracturing, we also attempted to increase the stiffness of the injection system by using a miniature screw pump with a very small internal volume. To allow us to operate this device consistently and electronically, we fabricated a pump-drive system using a high-torque gear motor (Figure 2.11). Later, this stiff, small-volume fluid injection system was improved further to allow extremely slow fluid injection ($\sim 0.5 \mu\text{L}/\text{min}$), which was necessary for injecting a viscous fluid into thin, low-volume hydraulic fractures. The new device (Figure 2.12) operates a small-diameter, screw-driven piston using a 5:1 ratio gear motor. The axial displacement of the piston is measured using an LVDT, which is measured and converted to the volume of the injected high-stiffness, liquid metal used as the drive fluid.

In Figures 2.13 and 2.14, the results of four hydraulic fracturing experiments are presented, conducted with initial flaws with various sizes. Note that for these experiments, the pump system in Figure 2.11

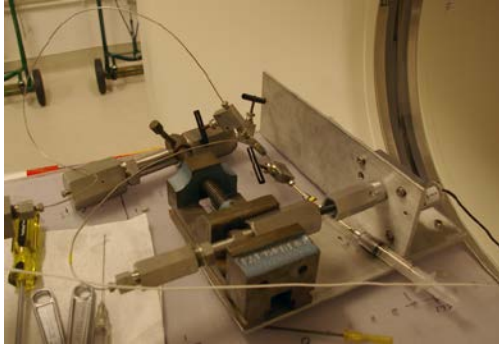


Figure 2.11. Motor-driven, miniature high-pressure fluid injection device (initial model)

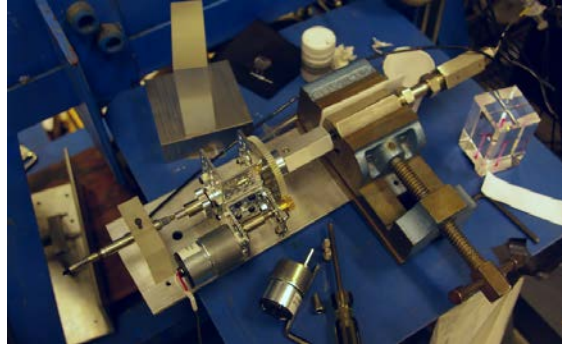


Figure 2.12. Improved, lower-speed system with a fluid-volume measurement capability.

was used. A test with no flaw resulted in very abrupt propagation of a fracture (Test#4), which did not allow us to image the fracture growth. (The optical images were taken at 1 frame/second rate.) With increasing flaw size, however, the breakdown pressure reduced, and the propagation of the fractures became slower and more stable. Note that the images of the growth of fractures shown in Figure 2.15 took almost 20 seconds.

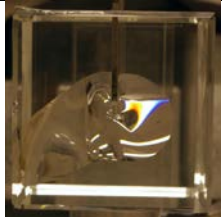
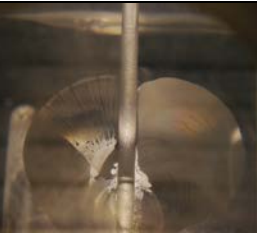
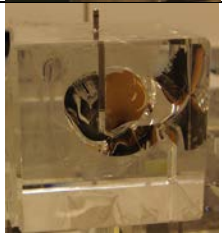

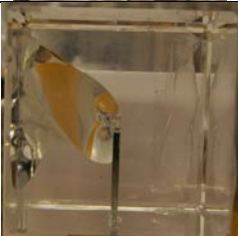
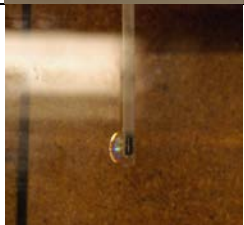
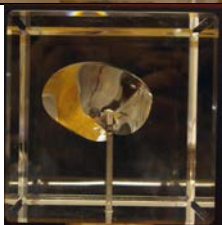
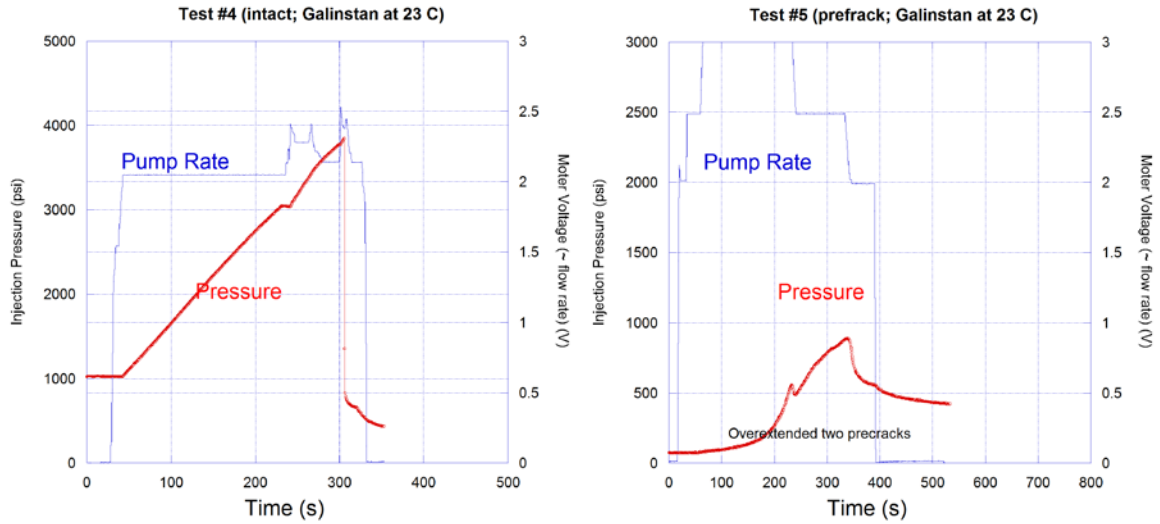
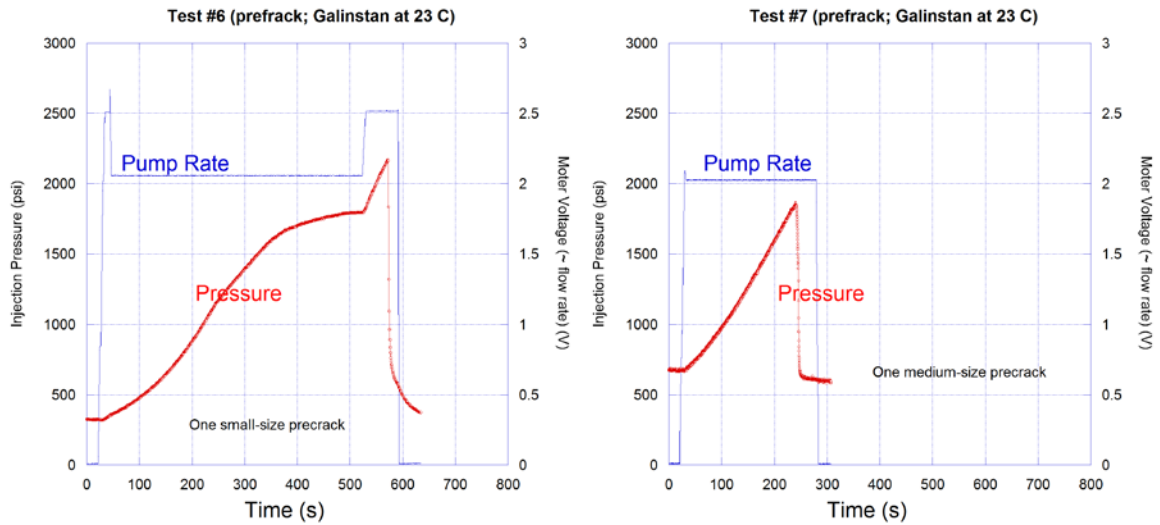
Test	Description	Initial State (Before injection)	Final State (After injection)
4	Intact sample.		
5	A pair of initial cracks *These precracks overextended due to subcritical crack growth before the experiment		
6	Small, one-sided initial crack		
7	Medium, one-sided initial crack		

Figure 2.13. Liquid metal injection experiments into intact glass cubes for visualization of controlled hydraulic fracture growth



(a) Test#4 (Intact)

(b) Test#5 (large precracks)



(c) Test#6 (small precrack)

(d) Test#7 (medium precrack)

Figure 2.14. Pressure histories during hydraulic fracturing experiments. The pump rate (given in V) is not calibrated to actual flow rates. The size of the pre-induced crack (flaw) determines the breakdown pressure as well as the pressure decline rate which is related to the speed of fracture propagation. Note that the pressure drop in an intact sample (a) is instantaneous.

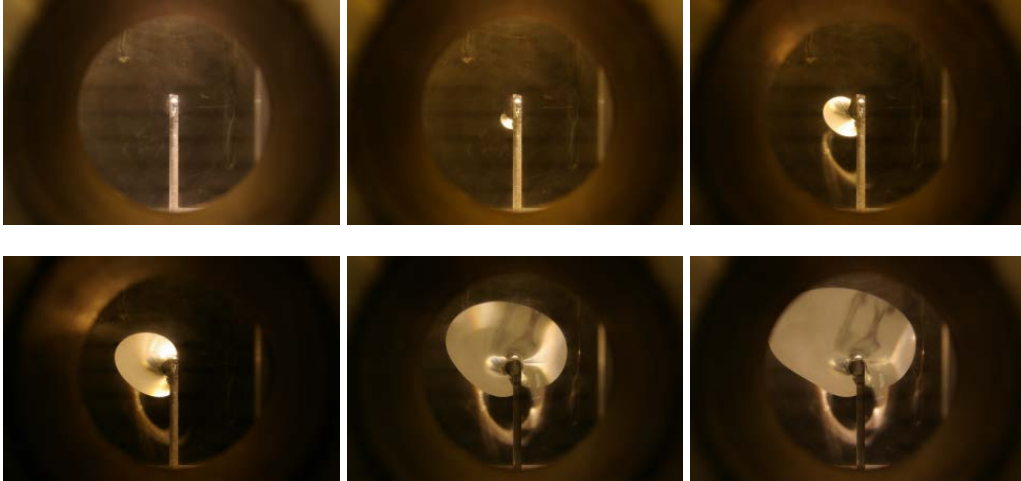


Figure 2.15. Reduced-speed fracture growths in Sample #7. The total growth time is ~20 seconds.

In order to reduce the speed of fracture growth further, which should allow us to examine the details of interactions between hydraulic fractures and preexisting fractures, we also used highly viscous fluid (glycerol anhydrous, viscosity ~1,100 cP at 23°C) as the fracturing fluid. This extended the fracture propagation time to several minutes, as well as increased the breakdown pressure in spite of the use of initial flaws (Figure 2.16). One problem of the experiment was that the induced fracture was nearly invisible when seen at high angles (Figure 2.17, 2.18). Because of this, we developed fracture image enhancement methods using fluorescent dye.

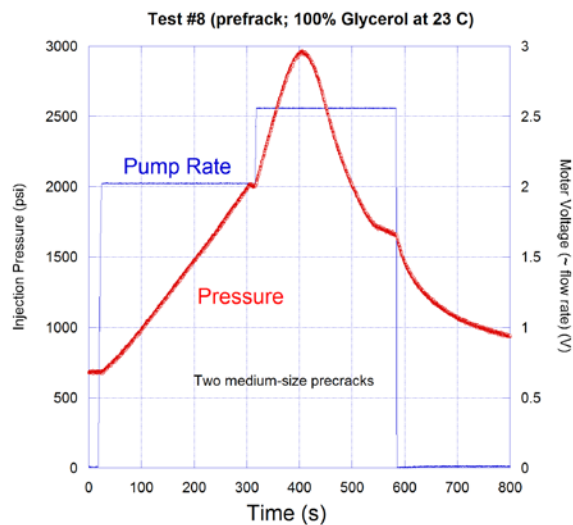


Figure 2.16. Pressure histories during a hydraulic fracturing experiment with glycerol. The pump rate (given in V) is not calibrated to actual flow rate. Compared to the low-viscosity-fracturing fluid results in Figure 2.14, fracture propagation is much slower, and the peak injection pressure (breakdown pressure) higher. The flaw size was similar to the medium-size flaws in Test#7.

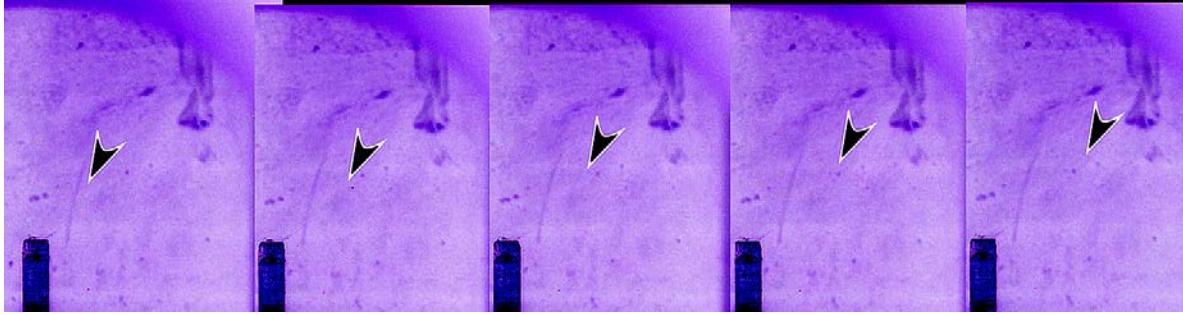
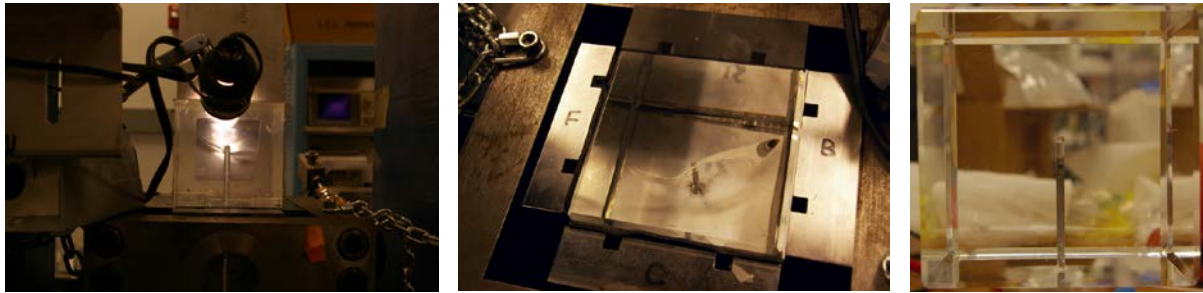


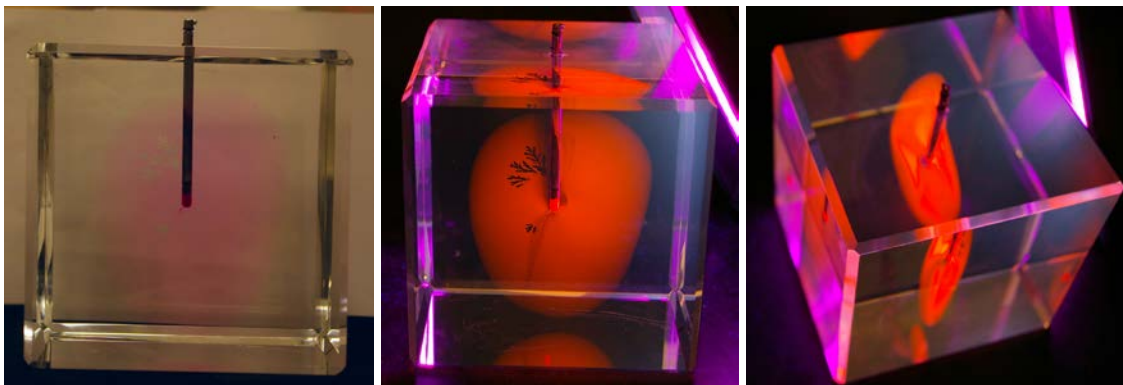
Figure 2.17. (Enhanced) Visual images of hydraulic fracture growth during the experiment. The total sequence here is ~20 seconds. The fracture front is barely visible.



(a) Fracture image in the mirror (b) Sample immediately after the experiment (c) Front view of the fracture

Figure 2.18. Images of hydraulic fractures after the experiment. At shallow angles, the hydraulic fractures can be easily seen (a,b). In contrast, from the direction near-perpendicular to the fracture plane, they are hardly visible (c).

An additional improvement was made to the visualization technique of hydraulically generated fractures. Although, we successfully produced stable, through-growing hydraulic fractures using anhydrous glycerol (viscosity 1,100 cP at 25°C) as the fracturing fluid, unfortunately, because of the relatively close refraction index values between the soda-lime glass and the glycerol, and the extremely small fracture thickness, it was very difficult to visualize the fracture growth. To make the fractures more visible, we used a fluorescent dye mixed with the glycerol. The fluid we used was 1%wt sulfo-rhodamine B in anhydrous glycerol, which fluoresces very strongly in yellow to orange (or blood red in long-wavelength UV light. Figure 2.19).



(a) Under room light

(b) Under long-wavelength ultraviolet light

Figure 2.19. Enhanced visualization of hydraulically produced fractures using a glycerol-sulforhodamine B mixture.

The optical visualization system using the true-triaxial loading frame was also updated with two high-resolution webcams (Microsoft Lifecam) with 30 fps speed capability. These cameras provide both top-down view of the fractures through a diagonal mirror embedded in a transparent acrylic cube and a side view through a port hole in the lateral load frame and a transparent acrylic spacer block. During the visualization experiment, the light used to illuminate the fractures was filtered to blue-green (upper cut-off at $\sim 550\text{nm}$ wavelength) to enhance the color contrast of the fractures against the background (Figure 2.20). Examples of the obtained images (extracted from video images) for fracturing of an intact block is shown in Figure 2.21, together with the accompanying injection fluid pressure and volume history in Figure 2.22.

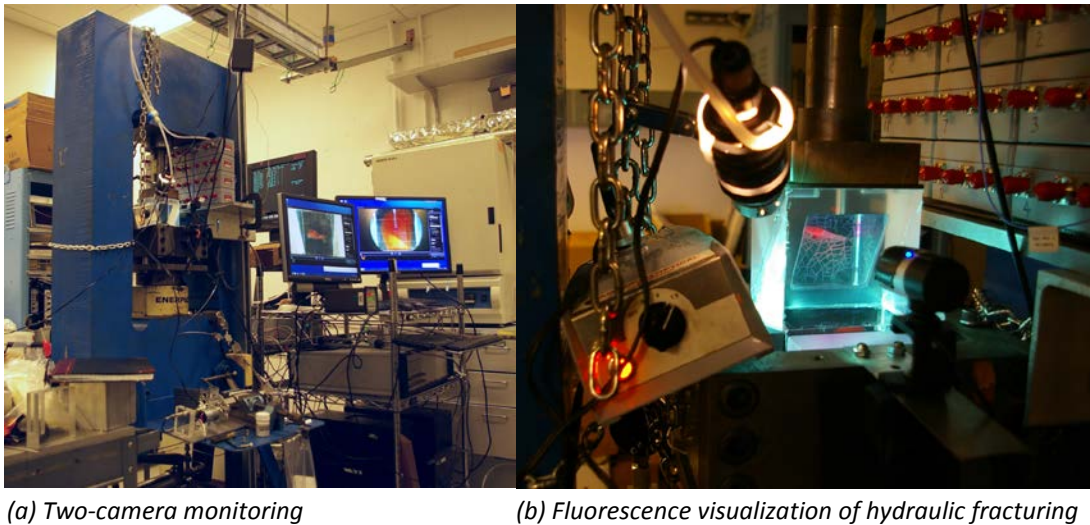


Figure 2.20. Enhanced visualization of hydraulically produced fractures using a glycerol-sulforhodamine B mixture.

Initially, the system was also equipped with two acoustic emission sensors (Physical Acoustics) to monitor the fracturing of the sample seismically. Finally, a capability to monitor anisotropic expansion of the sample due to fracturing was added by installing new syringe pump controllers (ISCO/Teledyne) with analog pump fluid volume data output (the volume of the oil expelled out of the hydraulic cylinders in the three perpendicular directions can be used to measure the sample expansion along the axes). However, unfortunately, the acoustic emission monitoring and the anisotropic sample expansion measurement did not produce meaningful data. One possibility for the undetectable acoustic emissions was because our sensors could not be attached to the sample surface directly, and the small waves generated by the fracturing may have been reflected and damped by the sample-platen boundaries (Note that the boundaries are lined with paper and/or rubber sheet to apply uniform stress on the surface). Additionally, it may also be possible that the frequency of the very slowly growing fractures in glass may be too low (aseismic growth) to be detected by the acoustic sensors (sensitivity band is tens of kHz up to 5 MHz), which raises an interesting scientific question. As for the volume expansion, we believe that the magnitude of the signal is too small because of the very small thickness of the fractures (considered to be a few micrometers). Although this is not undetectable displacement, the measurement errors from the syringe pumps' volume readout is on the order of tens of microns.

Using these experimental setups and techniques, we conducted experiments in Subtask 2.4 and 2.5

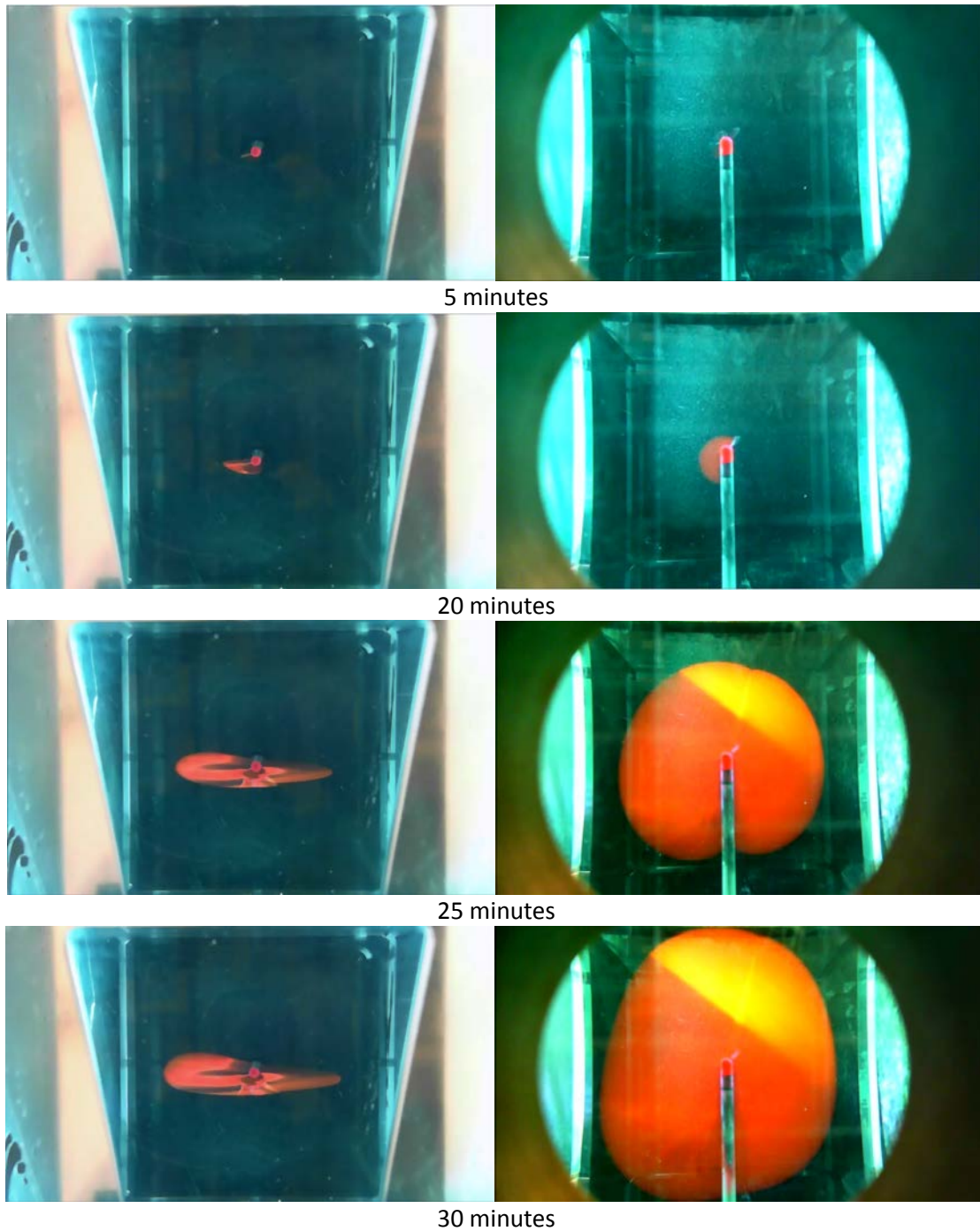


Figure 2.21. Top (left) and side (right) images of hydraulic fracturing in an intact glass cube subjected to anisotropic stress. Green-blue light was introduced in the glass cube, resulting in fluorescence of sulforhodamine B dissolved in glycerol. Thanks to the high viscosity of the fracturing fluid ($\sim 1,100$ cP) and very small fracture aperture, the experiment time is very long.

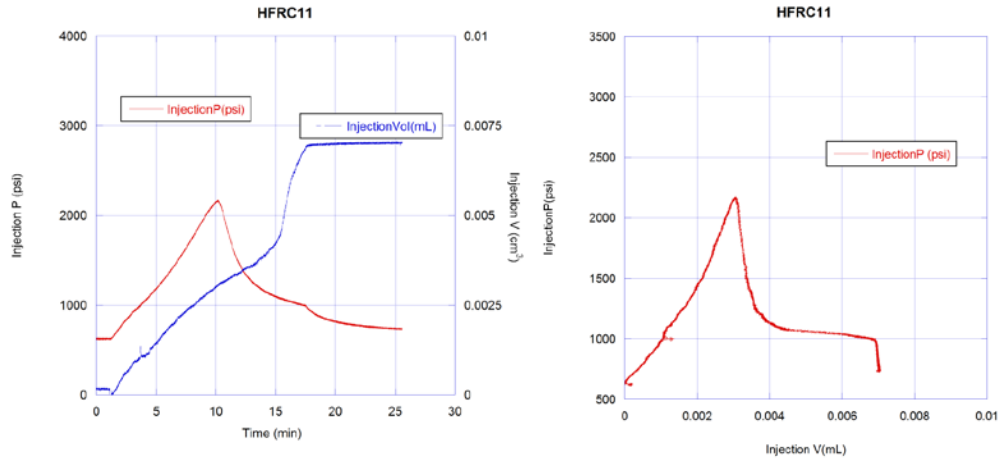


Figure 2.22. Time-injection pressure/volume history (left) and pressure-injection volume (right) results for hydraulic fracturing of an intact block.

The dye-assisted visualization experiments can be further enhanced by using a laser sheet as seen in Figure 2.8. This method is particularly powerful for imaging interactions between a hydraulic fracture and the laser-etched, 2.5D fractured reservoir models. As presented also in the subsequent sections for Subtasks 2.4 and 2.5, hydraulic fracturing experiments can be conducted while applying a laser sheet at the top of the reservoir model so that the interactions between the fractures could be seen clearly (Figure 2.23).

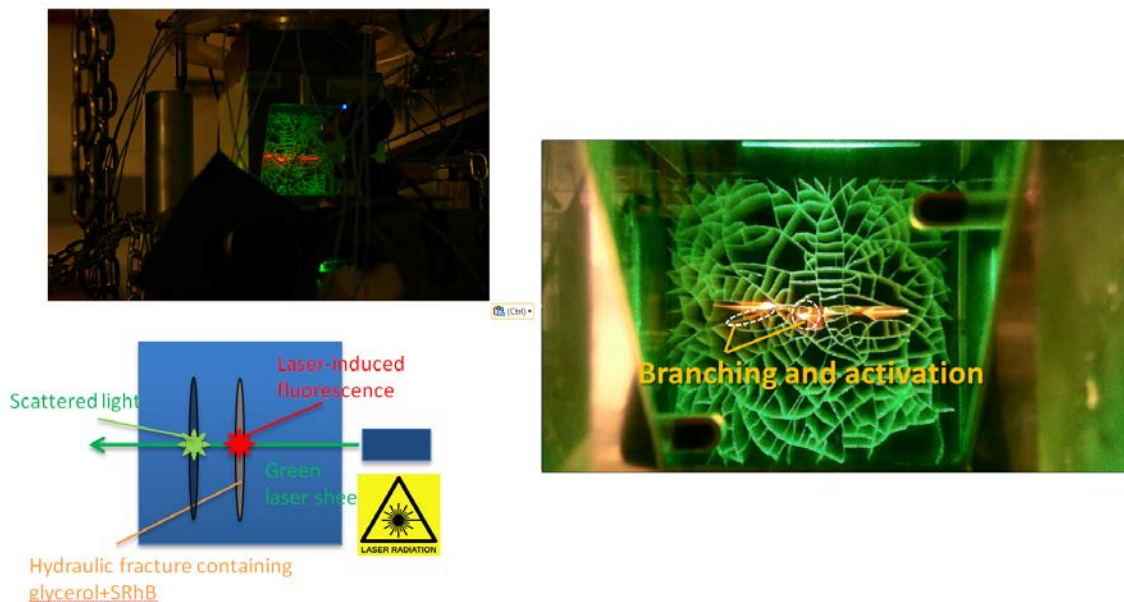


Figure 2.23. Laser-sheet-assisted visualization of hydraulic fracturing in a sample containing a 3D-laser-etched fractured reservoir model. The image above is a reflection of a sample being tested within a true-triaxial loading frame, in a diagonal mirror embedded on a transparent loading block.

X-ray CT imaging experiment

We also conducted a hydraulic fracturing visualization experiment in a true-triaxial cell. A random network of thermal contraction induced fractures was introduced in a slender block of soda lime glass, and an analogue borehole was installed for this experiment (Figure 2.24a). This sample was installed in the X-ray CT scannable true-triaxial test vessel, and subjected to principal stresses of 1,000 psi:1,000 psi: 1,172 psi. X-ray CT scanning was performed before, during, and after a hydraulic fracturing test on this sample, by injecting the high-density liquid metal. (Figures 2.24bc),



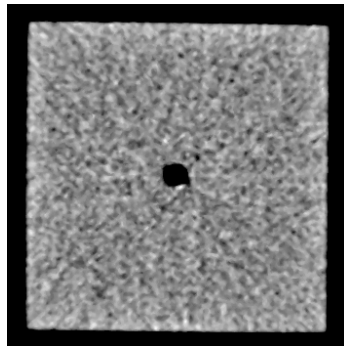
(a) Before test

(b) After test

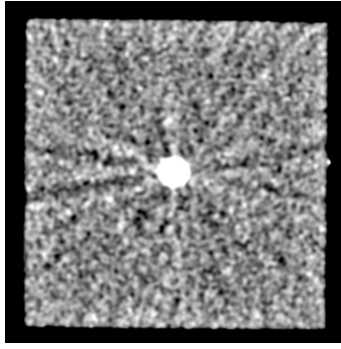
(c) Fluid leaked to the surface

Figure 2.24. Before and after images of prefractured glass block injected with liquid metal (the silver-colored fluid in the images). Although optically visible, the fractures injected with the metal did not appear clearly in the X-ray CT images.

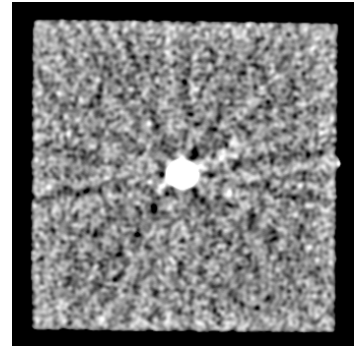
Pre-test scanning was performed to establish the baseline and allow for later differencing of images. This is often a very powerful technique to identify changes in a sample. A number of techniques were attempted before the test to attempt to identify the most advantageous scanning parameters. Figure 2.25a shows one slice of the pre-test scan. Each slice shown is 0.625 mm thick and the pixel dimensions are 0.187× 0.187 mm. Figure 2.25b shows the same location after applying enough pressure to saturate the well with the liquid metal. Note the high-density (~6.5g/cc) Galinstan is present in the well, and a small bead is present on the right side of the block. This indicates that a fracture pathway exists in the block even without the injection pressure. Figure 2.25c shows the same location following a moderate pressure liquid metal injection (~500 to 200 psi), and Figure 2.25d shows the same location following a high pressure liquid metal injection (~1,400 psi maximum, resulting from high flow resistance). There is no obvious difference in Figures 2.25c. Figure 2.25d shows an accumulation of Galinstan at the lower right. The difference images in Figures 2.25e and f also did not show obvious fluid-filled pathways.



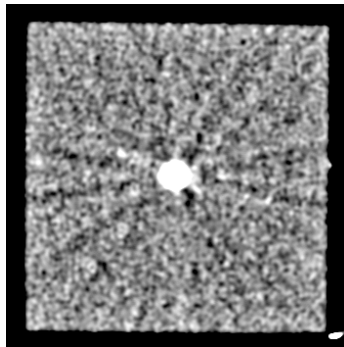
a. Pre-injection



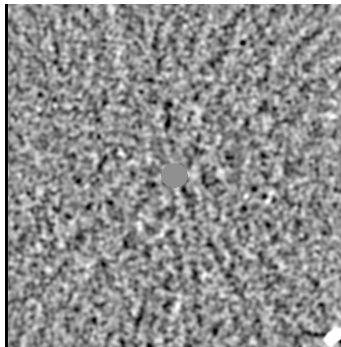
b. After low-pressure metal injection at low pressure, filling the borehole. Note bright spot at right border indicates metal had penetrated fracture.



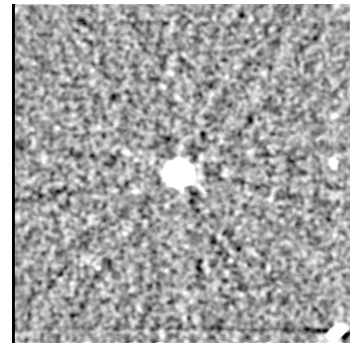
c. After moderate pressure injection. A possible fracture pathway could be identified, however the magnitude is within the measurement error.



d. After high-pressure metal injection. Note metal at lower right outside sample.



e. Difference between d and b. A large presence of metal in a fracture would be indicated by a brighter region. No fracture feature can be clearly identified.



f. Difference between d and a. Note presence of bright spot midway up the right side. No fracture feature can be clearly identified.

Figure 2.25. X-ray CT images during a hydraulic fracturing experiment inside a true-triaxial cell, with a liquid-metal injection fluid (only the slices at one location are shown, although the actual images was conducted for a 1.3-inch wide strip). Although the fluid was injected into the fractures and leaked to the outer surface of the prefractured glass block, the fluid within the fractures was not visible due to poor signal-to-noise ratio of the images.

The poor X-ray visibility of the liquid-metal-injected fractures is quite disappointing, and we do not think further improvement in image processing would dramatically improve the quality of the images, which is necessary for examining details of the interactions between hydraulic fractures and preexisting heterogeneity. We believe that the reason for the poor visibility is the extremely small thickness of tensile fractures produced in glass. Without application of stress, however, thanks to the larger aperture of the tensile fractures, imaging can be improved using a more sophisticated processing technique.

In order to improve visualization of thin fractures using X-ray CT, we investigated possible advanced image processing techniques to extract extremely thin fractures from X-ray CT images of fractured glass blocks, in collaboration with a RPSEA fracturing project. An example of a fractured glass block immediately after the thermal fracturing was induced by quenching (but before re-heating of the block) is shown in Figure 2.26. One effective technique is the Connected Component Analysis (Figure 2.27).

Using this technique in the image processing software FIJI (a version of the well-known ImageJ software), we were able to extract some fractures with more clarity than simple conventional processing.

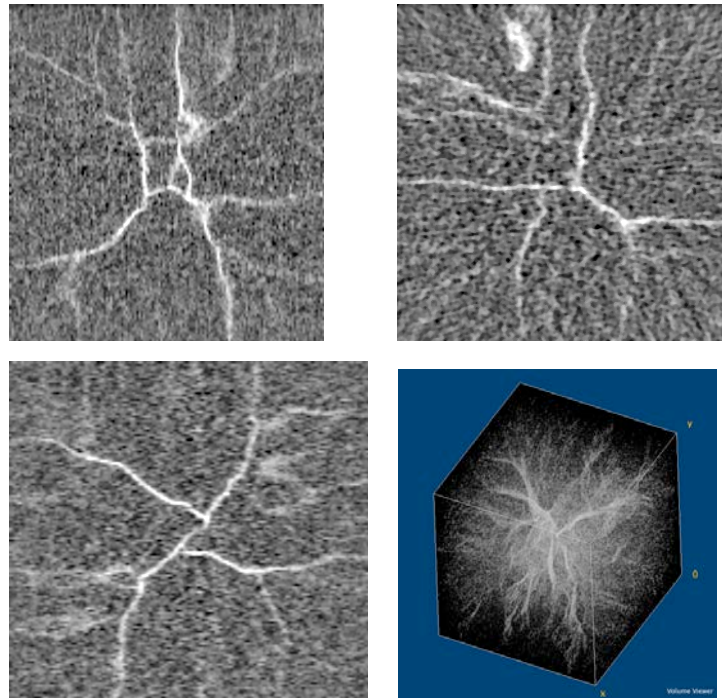


Figure 2.26. Three orthogonal X-ray CT cross sections of a thermally fractured block. The color look up table is inverted from normal, thus bright here indicates low density.

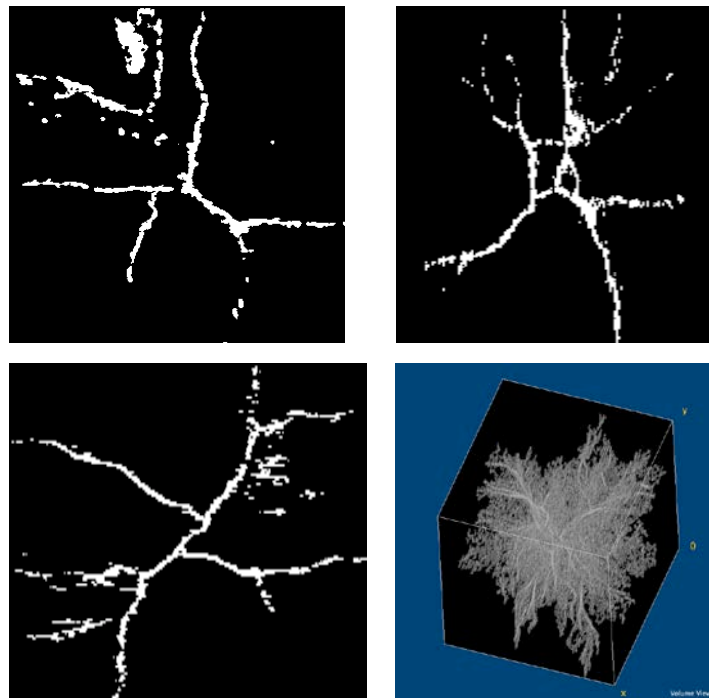


Figure 2.27. Fractures from Figure 2.26 extracted using Connected Component Analysis.

Fractures produced in natural rock can be much thicker, and the pores connected to the fractures can also be filled with the injected fluid, further enhancing the X-ray visibility. Thus, experiments with X-ray CT on natural rock (shale) samples were expected to be more successful. However, with sample we obtained for the experiment, we experienced a different set of problems, delaying the completion of a part of our milestones (*Milestone M4: X-ray CT imaging of hydraulic fracture growth in a real shale sample under true triaxial stress state*). Two major causes for the difficulties are (1) induced hydraulic fractures are still very thin and difficult to resolve using our medical CT scanner with weak beam energy and (2) shale samples are difficult to prepare, because swelling of the rock matrix resulted in drill tool failure during analogue borehole installation rock fracturing.

The shale sample we used for our experiment was Mancos Shale, obtained from Kocurek Industries, Inc. The dimension of the sample was 2.5 inches x 2.5 inches x 6 inches, with the longest dimension parallel to very prominent bedding planes. Although the cutting of the blocks by the vendor was mostly successfully done, drilling of a small, 1/8-inch diameter analogue borehole in the block turned out to be extremely difficult. Figure 2.28 shows X-ray CT images of one of the samples. In this sample we made two attempts to drill a hole from the opposite ends. Each time, the coring drill broke before a desired depth was reached, because the shale matrix swollen by the drilling fluid (water) increased the tool-rock friction too much. Additionally, both the excessive stress applied by the drill and the swelling pressure in the rock resulted in fracturing of the shale matrix.

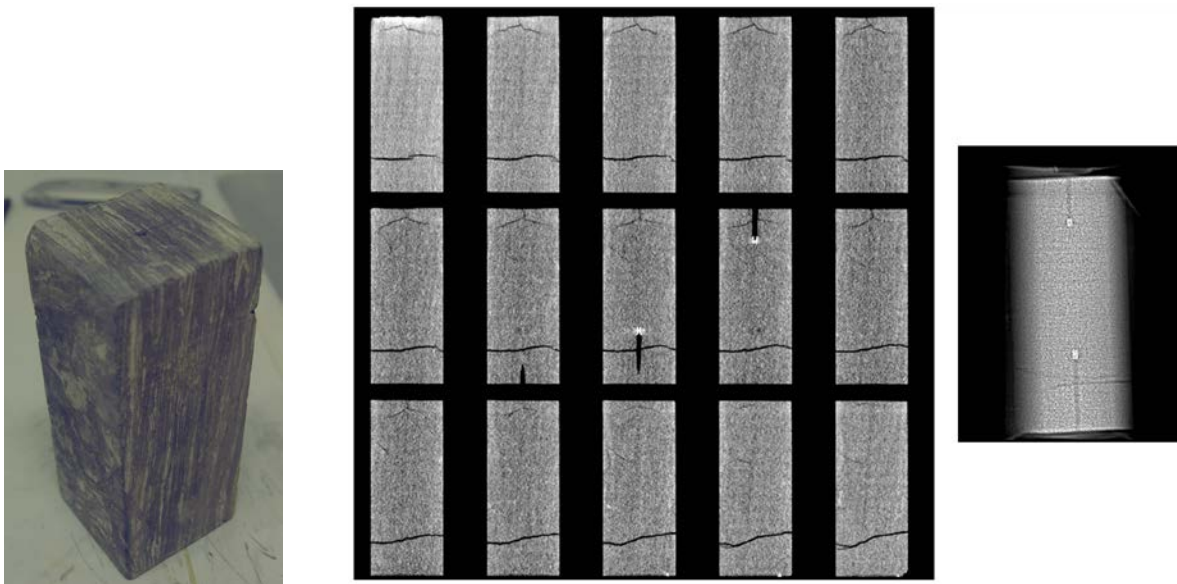


Figure 2.28. X-ray CT images of Mancos shale block (cutting through the sample in-and-out of the paper) with failed attempts to drill 1/8"-dia analogue boreholes. Broken bits can be seen as bright white spots (high density) at the ends of the incomplete, blind holes. Numerous pervasive fractures were also produced in the process.

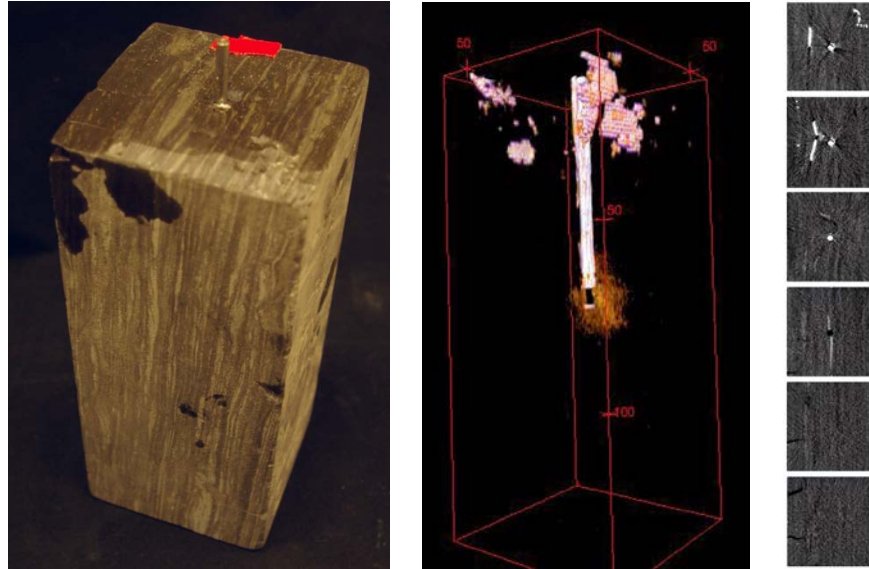


Figure 2.29. Mancos shale block prepared for hydraulic fracturing experiment using liquid metal (left). The sample leaked the fluid during the pre-experiment fluid injection stage. X-ray CT images (center and right) show the fluid penetrated into drilling-induced fractures and, possibly, preexisting shrinkage fractures.

Nonetheless, we managed to prepare one sample by drilling a ~3-inch deep, 1/8-inch diameter analogue borehole, and installing an injection tubing. However, unfortunately, this preparation resulted in unwanted fracturing of the rock matrix, primarily along the bedding planes. These fractures were filled with liquid metal (Ga-In-Sn) for a hydraulic fracturing experiment that was planned after the tube installation. Preliminary X-ray CT images of the sample (without hydraulic fracturing by high-pressure injection) show the injection fluid which is present along the induced fractures, leaking to the sample surface (Figure 2.29). Although this is an unsuccessful experiment, the images indicate that the fractures produced in shale can be much more open and visible to X-ray CT—with the help of the high-density liquid metal fracturing fluid—, compared to extremely thin fractures produced in glass.

2.1.4 Subtask 2.4– Hydraulic fracturing visualization I: Stress and texture anisotropy effect (Phase II)

Stress anisotropy effect

In order to examine the effect of the stress and texture (fracture) anisotropy, experiments were conducted by rotating the minimum principal stress direction by 90° against the texture of the fractured reservoir model, compared to the preliminary experiment. The applied confining stress state was the same as before, σ_x : σ_y : σ_z (vertical, borehole parallel)=722 psi: 1,084 psi: 1,445 psi (Note that these numbers are slightly higher than before, because we have made corrections to the cross section of the sample blocks). The newly conducted experiments all resulted in hydraulic fractures which clearly propagated perpendicular to the minimal principal stress direction, with small perturbations by the preexisting fractures. Although the previously conducted experiment produced some hydraulic fractures which were not necessarily perpendicular to the minimal principal stress, we believe this was caused by uneven loading on the sample, and the uniformity of the loading has been improved at the end of project Phase I. Although we could have repeated the previous experiment, because the stress/texture

anisotropy effect in our samples is rather trivial (and more critically, because we have only a limited number of synthetic, laser-engraved fracture models), we decided to allocate the remainder of the synthetic fracture models to other experiments (which examine the impact of other more important factors such as the effect of fracture height and weakness, and of fluid viscosity and injection rate as examined in Subtask 2.5).

Note that the throughout the experiments conducted in the Phase II, the anisotropy and orientations of the principal stresses, with respect to the texture of the laser-engraved fracture models, were kept consistent with the on-going numerical modeling. This was done so that the fracturing behavior was easily compared between the simulations and the experiments. In the following, we will describe the results of these experiments. Additionally, we realized that it was necessary to examine the effect of the fractured reservoir height and the strength so that the numerical simulations conducted using 2D models can be compared to the laboratory experiment. These experiments are reported shortly after experiments on strongly textured shale sample.

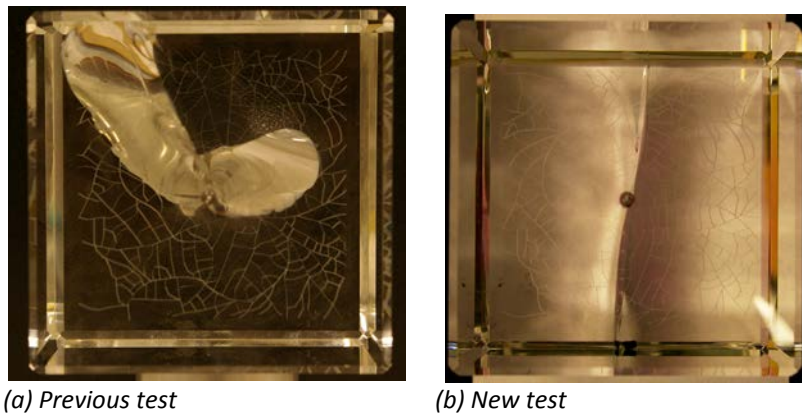


Figure 2.30. Stress and texture anisotropy and hydraulic fracturing orientations. In the “Previous test,” the maximum horizontal stress was applied in the horizontal direction (a) while in the “New test,” it was applied in the vertical direction in the images (b). (Note that these would be top-down views of the samples during the experiment.) Although the fracture orientations were not well defined in the previous test (possibly because of uneven application of confining stress), in both cases, the fracture orientations align with the direction of the maximum horizontal stress.

Texture anisotropy effect

A hydraulic fracturing experiment was conducted on the only successfully prepared sample in Subtask 2.3. Note that, as mentioned earlier, drilling and clay-swelling-induced damage (prefrac) was induced around the borehole. We applied principal stresses of 700psi: 1050psi: 1400psi to this sample within the true-triaxial confining cell. The intermediate stress was applied in the axial direction (parallel to the borehole), and the maximum principal stress perpendicular to the bedding plane (Figure 2.31). For an isotropic rock and glass blocks, a hydraulic fracture would grow in the direction of the maximum principal stress, perpendicular to the shale texture orientation (and the short prefrac). The fracturing fluid was Galinstan (Galium-Indium-Tin) which has a density of 6.44g/cc (at 20°C) and viscosity 2.4 cP. The fluid was injected at an approximate rate of 0.7 $\mu\text{L}/\text{min}$, using a home-made, gear-motor-driven micro linear syringe pump. The snapshots of the experiment are shown in Figure 2.32.

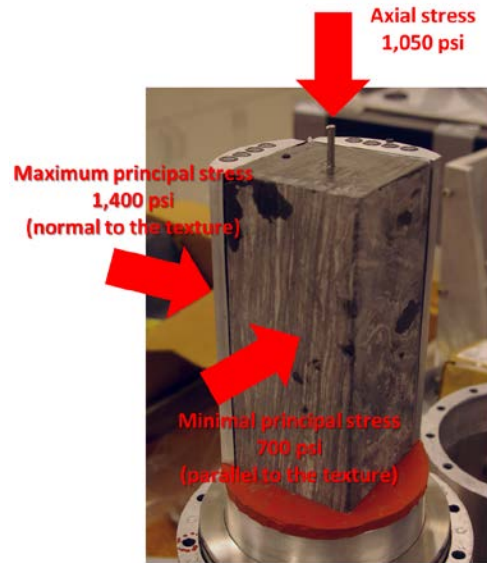


Figure 2.31. Principal stresses with respect to the bedding plane texture of a Mancos Shale block used for the hydraulic fracturing/X-ray CT imaging experiment

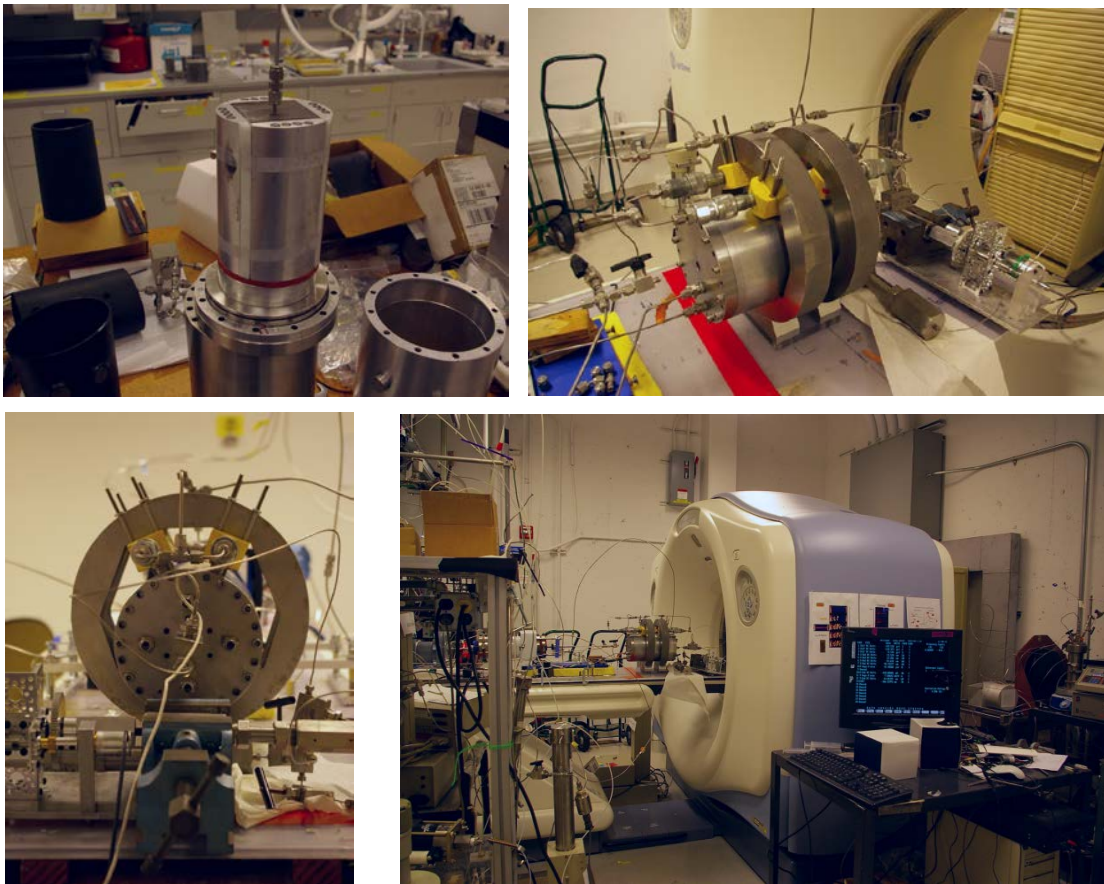
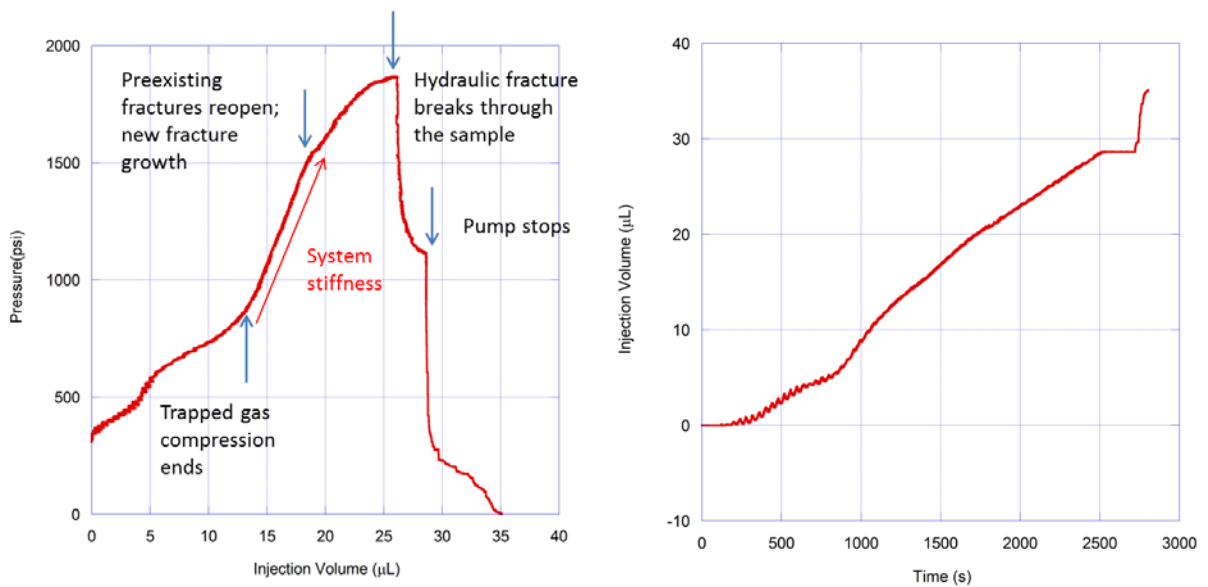


Figure 2.32. Experiment in progress. A rectangular block is surrounded by aluminum platens to form a cylindrical sample (upper left) which is jacketed and installed in the true-triaxial vessel (upper right and lower left). During the experiment, three principal stresses, injection pressure, and injected fluid volume are monitored (lower right).

Although we anticipated that the sample might not be able to hold high injection pressure due to the damage around the borehole (i.e., the injected fluid may simply leak along the borehole), because of the limited extent of the damage, the borehole was well sealed. The injection pressure vs injection fluid volume and the corresponding injection volume history are shown in Figures 2.33a and b, respectively. After the initial compression of the injection system and the borehole (injection volume $< \sim 13 \mu\text{L}$), the system behavior becomes linear until the injected fluid starts to penetrate the damage around the borehole (fracture re-opening). The slow further increases in the injection pressure and the decreases in the pressure increase rate indicate increases in the size of the fracture. At $\sim 26 \mu\text{L}$ (or $\sim 1860 \text{ psi}$ injection pressure), the pressure reduces suddenly, and the injection volume vs time relation becomes linear, because the fracture reached the outer sample boundary where the pore pressure is ambient (atmospheric pressure).



(a) Injection pressure vs volume

(b) Injection volume vs time

Figure 2.33. Injection pressure and volume during a hydraulic fracturing experiment in a true-triaxial cell

A series of X-ray CT images were taken during the hydraulic fracturing experiments. The block ($62 \times 62 \times \sim 149 \text{ mm}$) was contained in the True-triaxial apparatus, and aligned horizontally on the CT table. The True-triaxial cell provides a $\sim 31 \text{ mm}$ X-ray transparent window for CT scanning. In total, 17 sets of scans were performed over the course of the test. The first five sets were performed to optimize the visualization, and the remaining 12 were performed to monitor the test. CT operational parameters are shown in Table 2.1. Early scans in the sequence were performed approximately every 5 minutes, with later scans performed more frequently (Table 2.2). Liquid galinstan (density $\sim 6.44 \text{ g/cm}^3$) was the fracturing fluid for high CT contrast. As we speculated, compared to previously conducted X-ray CT/hydraulic fracturing tests on glass blocks, hydraulic fractures in natural rock sample are thicker and much more visible when the liquid metal was used as a contrasting fluid. Note that however the fractures would be still not visible using a medical X-ray CT scanner if low density fluids such as brine and gas were used.

Table 2.1. CT operational parameters.

Scanning Parameters	140kV, 300 mA
Voxel size	0.2x0.2x0.625 mm
Reconstruction Algorithms	Standard, Detail
Scan Duration	11 sec
Scan Axial Travel Distance	4 cm

Table 2.2. Scan times and experiment conditions.

	Scan	Scanner Clock Time	Pressure (psi)
Baseline	6	11:44:51	334
	7	11:49:29	399
	8	11:54:45	533
Images Shown Below	9	11:59:30	710
	10	12:04:29	967
	11	12:09:43	1540
	12	12:11:13	1600
	13	12:14:30	1743
	14	12:17:01	1820
	15	12:19:30	1860
	16	12:20:54	1357
	17	12:23:45	1118

CT scans were evaluated using ImageJ (Rasband 2016). Data from scans 6-8 were averaged, resliced from the top to provide horizontal slices (nearly parallel to the fracture), and a 2-pixel radius Gaussian blur was applied to reduce noise in the fracture plane. Each subsequent data set was treated identically, however no averaging was performed for those data sets. The averaged Scan 6-8 data were subtracted from later data sets to highlight changes in the system. The 3-dimensional data are displayed using the Volume Viewer plugin (Kai Uwe Barthel), from three orthogonal perspectives – top, side, and axial (Figure 2.6) In the Volume Viewer plugin, the 3-D Fill transfer function was used, with regions that were hand selected based on intensity. This results in some inconsistencies in the displayed data as the algorithm selects connected regions, however the hand selections were done in a single session to minimize inconsistencies. The largest by-hand inconsistencies occur on the selection of regions in the final scans (16 and 17), where regions of liquid metal have become isolated. Additionally, out-of-fracture-plane blobs are identified in Scan 17; these are likely to artifacts of the selection process.

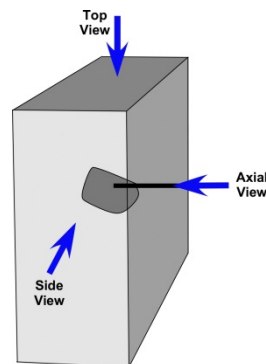
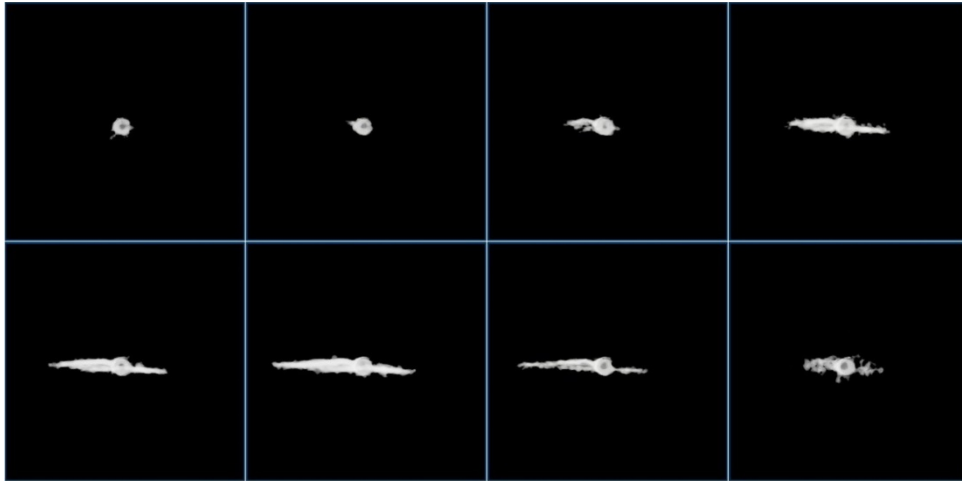
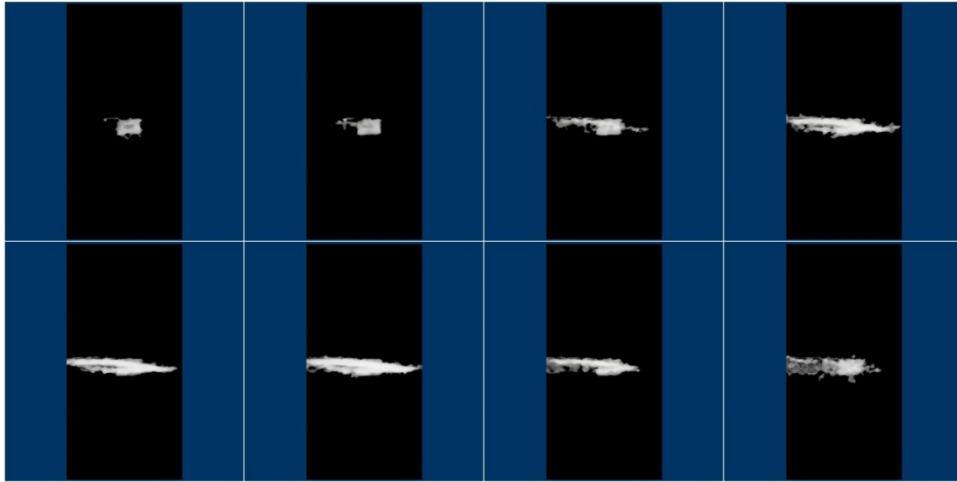


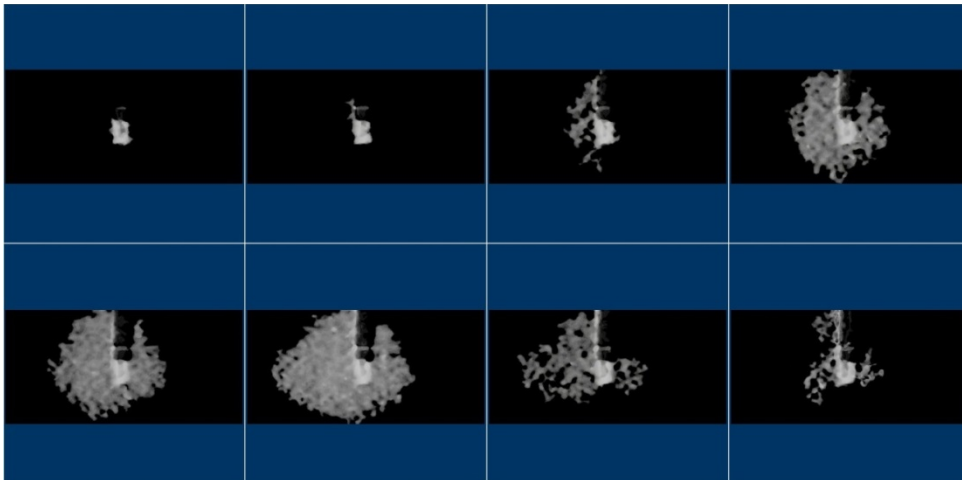
Figure 2.34. View perspectives.



(a) Axial views (~62mm x ~62mm)



(b) Side views (~62 mm x ~31.25 mm)



(c) Top views (~31.25 mm x ~62 mm)

Figure 2.35. Three-direction views of scans 10-17 showing fracture pressures increasing from 334 to 1860 through Scan 15 (first 6 images) and decreasing to 1118 psi over the last two scans.

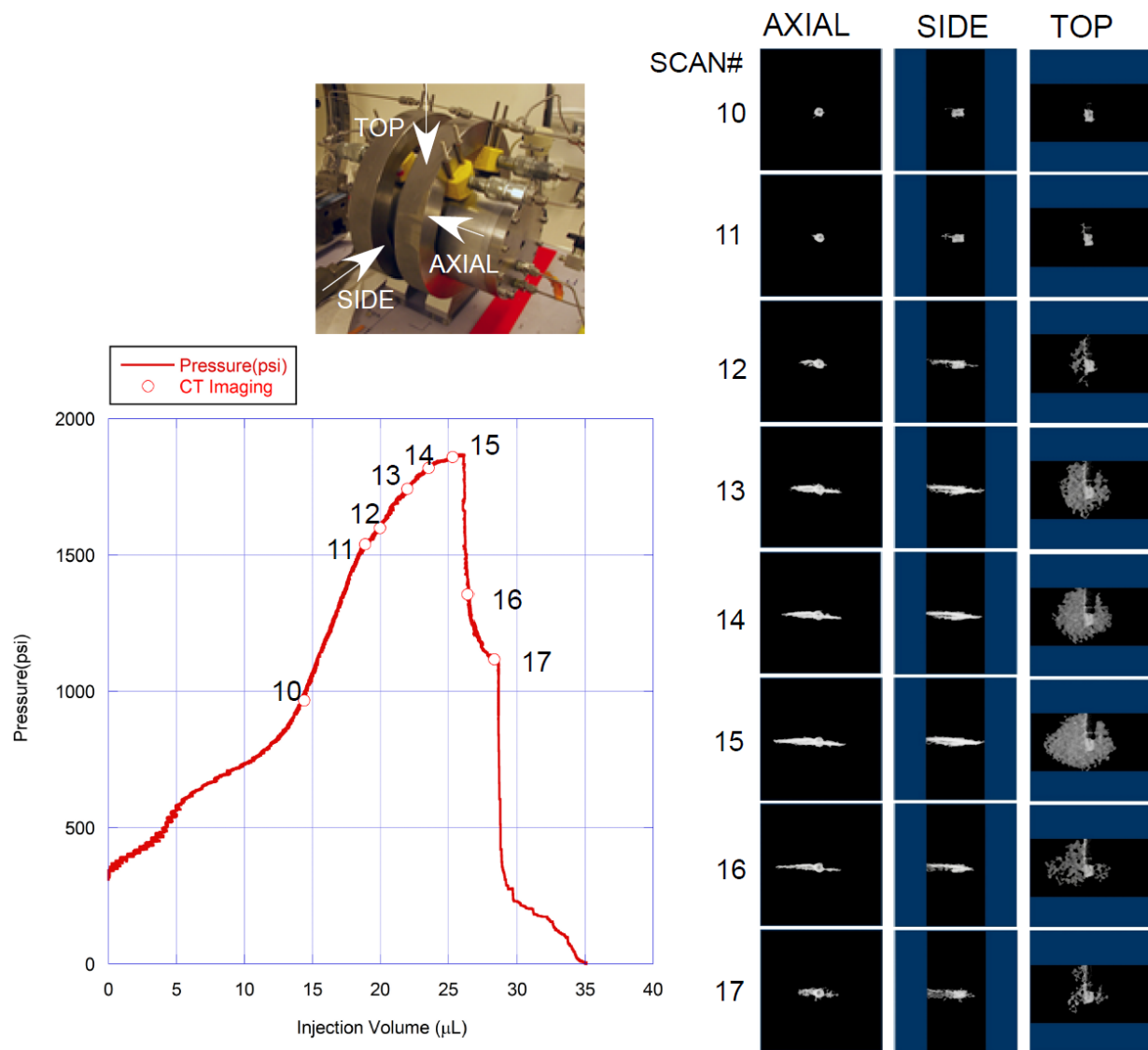


Figure 2.36. Correlated results for the hydraulic fracturing test (pressure vs. injection volume) and the X-ray CT images.

From Figure 2.33 the preexisting fractures open at ~1500psi, corresponding to the second CT images in Figures 2.36a,b and c. The results correlated with the pressure-injection volume data are summarized in Figure 2.36. The injection pressure still increases after this “reopening pressure,” before the critical fracture size is reached. The observed orientation of the fracture growth however is parallel to the minimum principle stress and along the bedding planes, indicating that the fracture orientation was dictated by the shale texture, rather than the principal stress directions.

In the post-experiment visual images of the shale block, a breakthrough of the fracturing fluid can be confirmed (Figure 2.37).

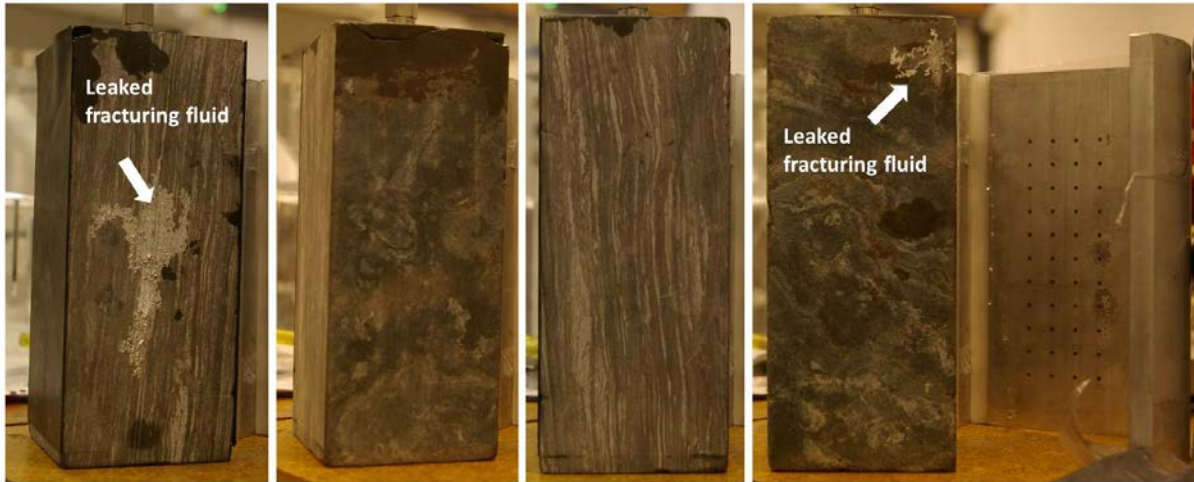


Figure 2.37. Mancos Shale block after a hydraulic fracture visualization experiment. The four sides of the block are shown. The fracture propagated along the bedding planes, but also along some of the preexisting fractures.

Fracture height effect

The “standard” fractures in glass cubes have a height of 0.25 inches (6.35 mm). We also prepared “tall-fracture” samples with a height of 0.5 inches (12.7 mm), and later, “very-tall” fracture samples with 1.0 inches (25.4mm). Fracturing in the standard sample showed some interactions of hydraulic fractures with the preexisting fractures. However, its behavior was dominated by the fracturing of the intact part of the glass matrix, in contrast to numerical simulations. We suspected this may have been caused by the three-dimensional nature (of texture anisotropy and heterogeneity) of the laboratory model. In contrast, numerical simulations essentially are done in 2D. To examine the impact of the fracture height, we tested a “tall-fracture” sample under the same test conditions as the “standard” sample.

In both cases, initial real-time optical visualization (Figures 2.38, 2.39) indicated that the growth of a planar, disk-shaped hydraulic fracture was affected by a fractured reservoir model (seen as a notch/shadow in the top views, and changes in the color and fracture’s external contour in the side views). However, detailed interaction between the hydraulic fractures and the segments of the preexisting, laser-etched fractures, however, was difficult to identify from these images.

To gain better understanding of the hydraulic fractures within the reservoir section, we used a green laser sheet to illuminate a part of the reservoir (Figure 2.40, 2.41). Because hydraulic fractures and activated preexisting fractures connected to them are filled with glycerol containing fluorescent dye, they glow in bright red which stands out against the green-colored background fracture model. In the “standard” model, some interactions between hydraulic fractures and the preexisting fractures occurred, particularly when they intersect at shallow angles. In contrast, the “tall fracture” model showed extensive activation of preexisting fractures. This indicates that the predominant fracturing of intact matrix within a fractured reservoir section in the laboratory may be caused by the three-dimensional nature of the model. (Note that so far, our 2D numerical modeling has shown that hydraulic fracturing occurs mostly along the preexisting fractures.) The injection pressure and volume records are shown in Figure 2.42. Note that for the “tall fracture” experiment, the volume data is irregular because the sensor slips occurred during the test.

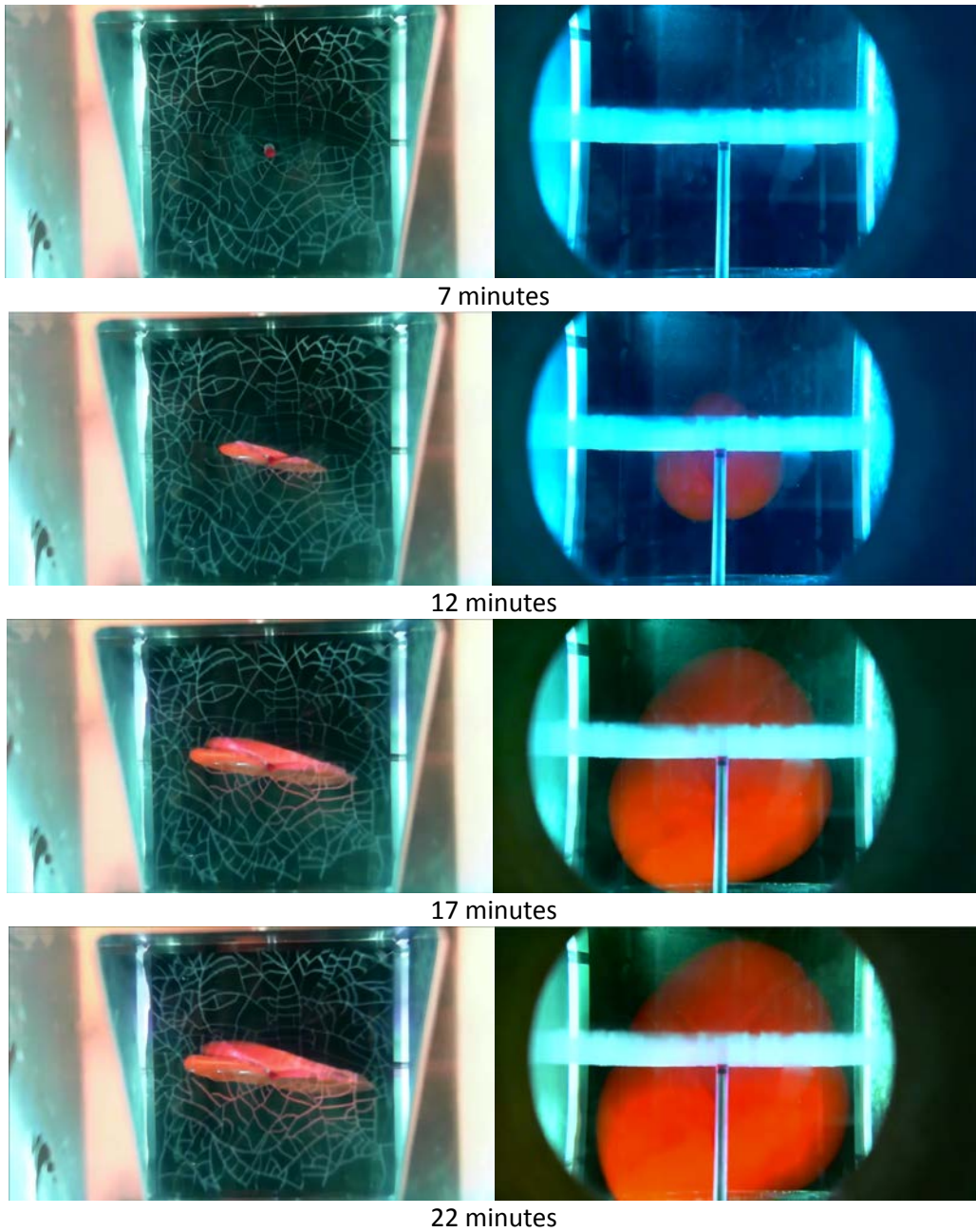


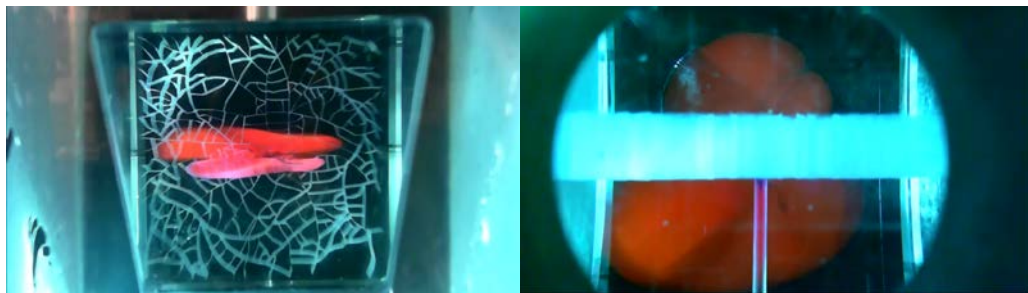
Figure 2.38. Top (left) and side (right) images of hydraulic fracturing in a glass cube containing “standard” fracture model injected with high-viscosity fluid.



10 minutes



15 minutes



20 minutes

Figure 2.39. Top (left) and side (right) images of hydraulic fracturing in a glass cube containing “tall” fracture model injected with high-viscosity fluid.

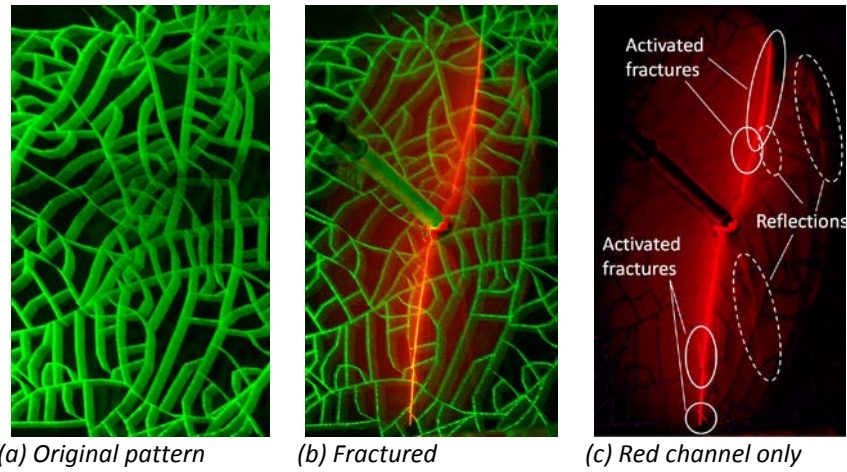


Figure 2.40. Fracturing of a “standard” height fractured reservoir model ($H=0.25$ ”). Hydraulic fractures are mostly propagating within intact matrix. The preexisting fractures are activated when the hydraulic fracture encounter a preexisting fracture at a shallow angle (see upper branch). Some high-angle fractures, however, were also activated but are not extensive.

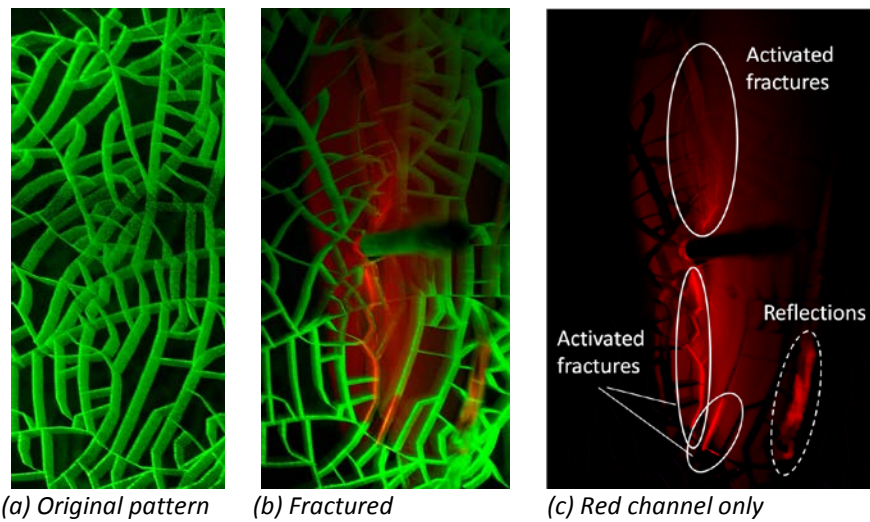
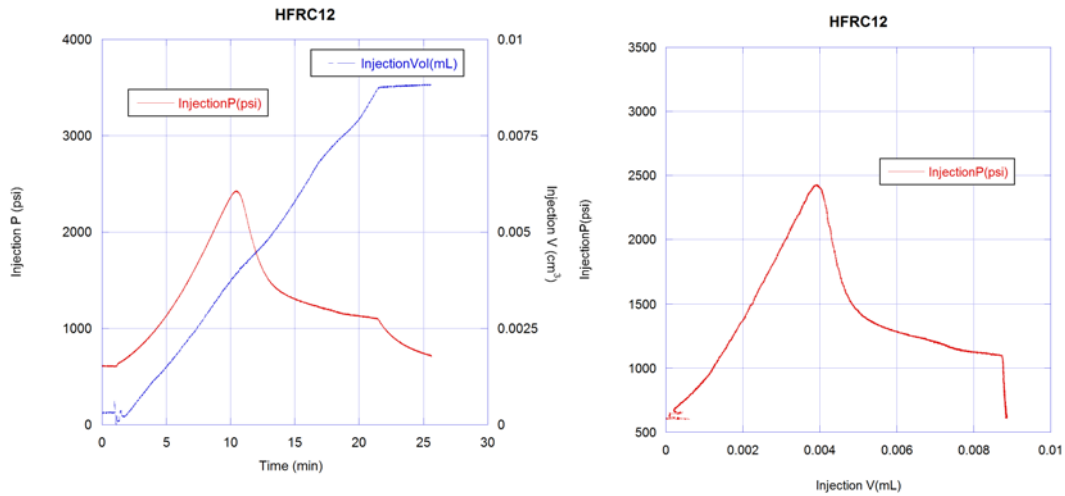
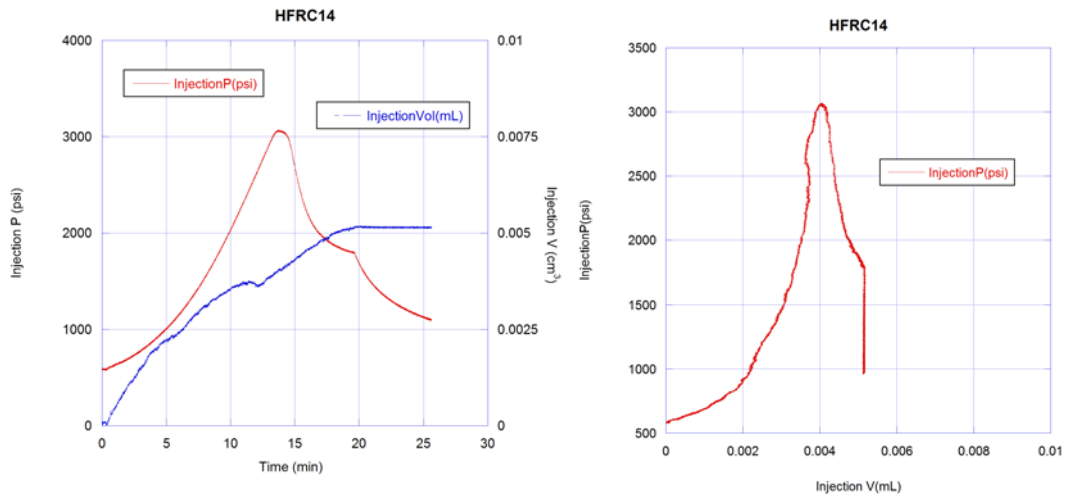


Figure 2.41. Fracturing of a “tall” fractured reservoir model ($H=0.5$ ”). Hydraulic fractures primarily followed the preexisting fractures. Note that the isolated fracture in near the bottom was in fact connected to the near-borehole part of the hydraulic fracture via fractures in the intact part of the sample surrounding the fractured layer.



(a) Standard height fractures ($H=0.25''$)



(b) Tall fractures ($H=0.5''$)

Figure 2.42. Time-injection pressure/volume history (left column) and pressure-injection volume (right column) results for hydraulic fracturing of an intact block. The top row is for the “standard height” fractures (a), and the bottom row is for the “tall” fractures (b). The injection volume record is irregular because of a slipped displacement sensor.

Later, we also conducted a similar experiment using a 1.0-inch fracture model. The strength of the fractures was also reduced by increasing the density of the microcracks constituting the etched fractures. As expected, strong interactions happened in this “very tall” fractured reservoir model. The level of interactions, however, was not dramatically different compared to the shorter, 0.5-inch tall fracture model, as shown in Figure 2.43 (the results of the current experiment is compared to the previous experiments on shorter fractures). Also, somewhat surprisingly, in spite of the weaker strength of the fractures, the hydraulic fractures still largely propagated within the intact part of the sample, instead of along the preexisting fractures.

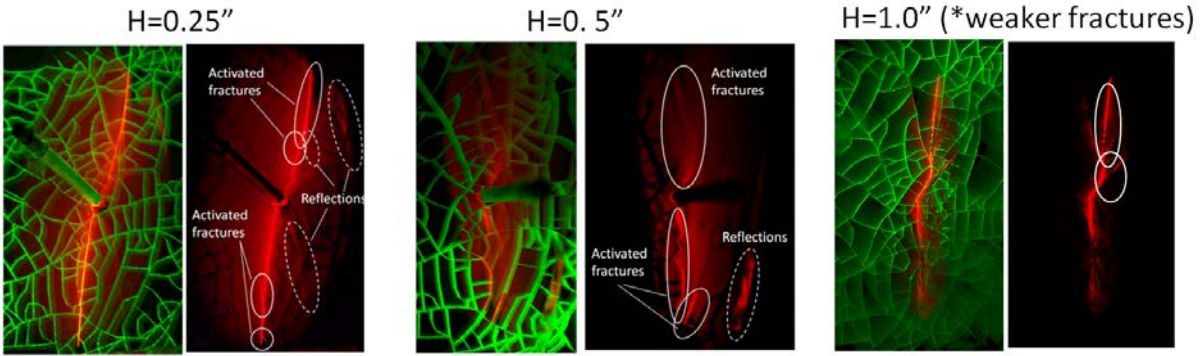


Figure 2.43. Interactions between hydraulic fractures (in red fluorescent light from the injected glycerol). All the experiments were conducted under anisotropic stress (4.8 MPa/7.2 MPa/9.6 MPa) and with an injection rate of 0.425 $\mu\text{L}/\text{min}$.

Fracture strength effect

The “standard” fractures are etched in glass with intervals of $\Delta x = \Delta y = 0.1\text{mm}$, $\Delta z = 0.15\text{mm}$. We also prepared “weaker” samples with intervals $\Delta x = \Delta y = 0.07\text{mm}$, $\Delta z = 0.15\text{mm}$ (we also have “low-density” samples with intervals $\Delta x = \Delta y = 0.2\text{mm}$, $\Delta z = 0.2\text{mm}$ which were not used) which has approximately 40% higher defect density. The results are shown in Figures 2.44, 2.45, and 2.46. The hydraulic fracture activated a preexisting fracture intersecting at a shallow angle at an early stage of propagation. Branching of the fracture near the bottom can be seen. The overall behavior is similar to the standard case, and it is rather difficult to distinguish the impact of the weaker fractures because of the different paths taken by the hydraulic fractures.

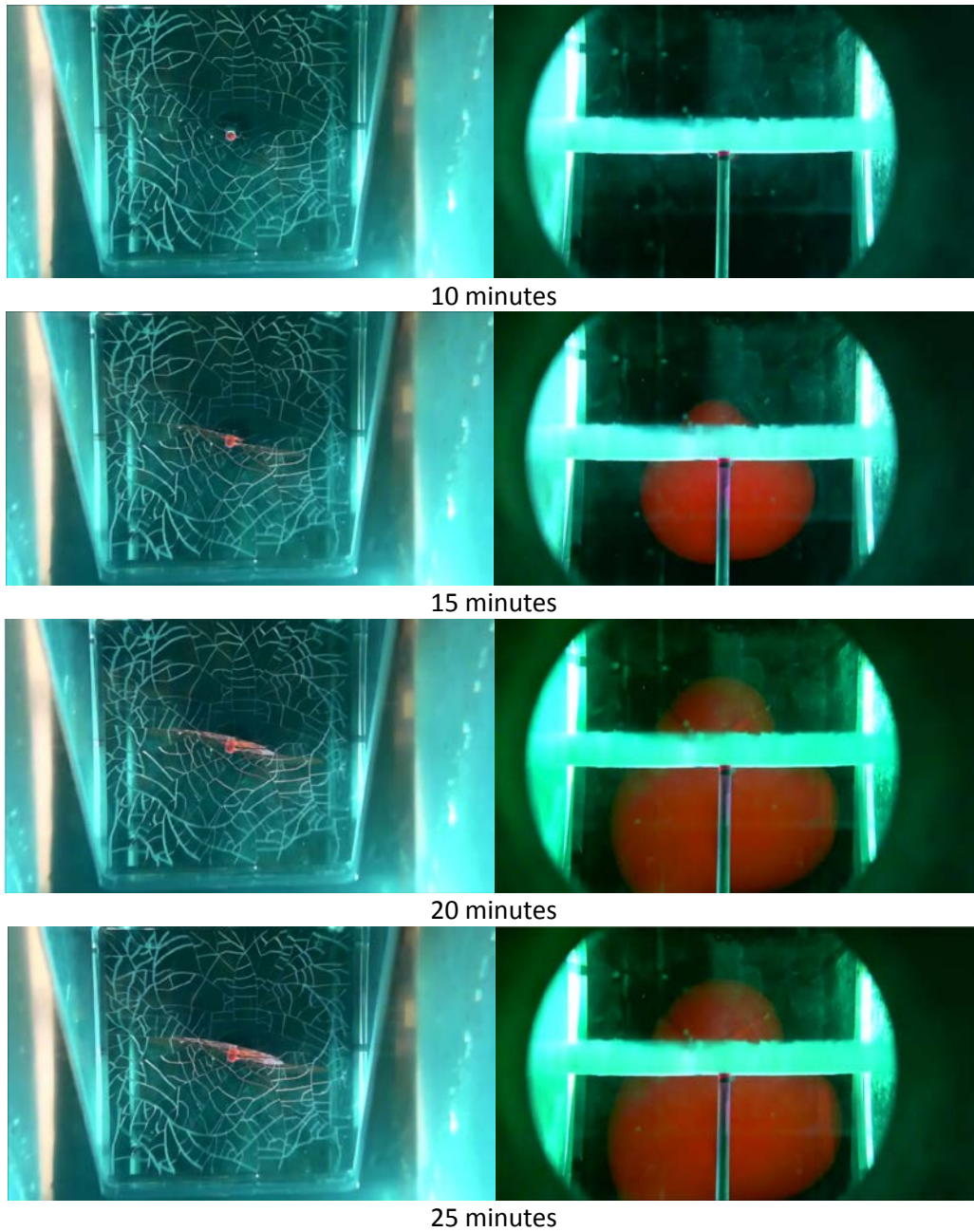


Figure 2.44. Top (left) and side (right) images of hydraulic fracturing in a glass cube containing “weaker” fracture model injected with high-viscosity fluid.

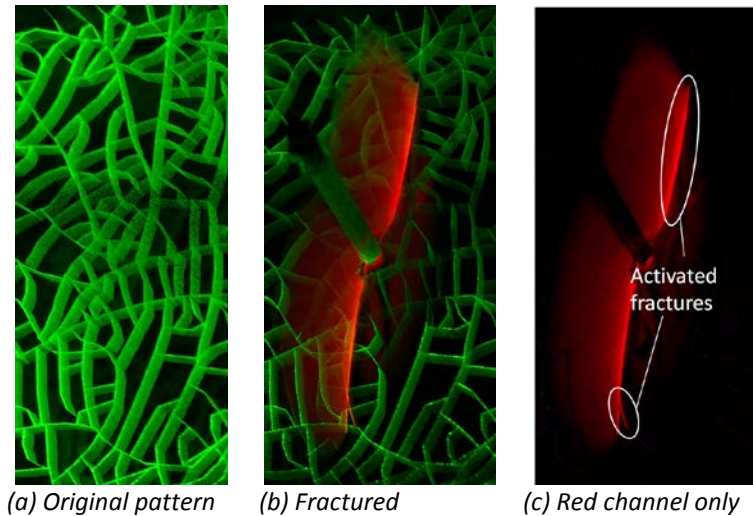


Figure 2.45. Fracturing of a “weaker” fractured reservoir model. (Compare to the “standard” model in Figure 2.40.)

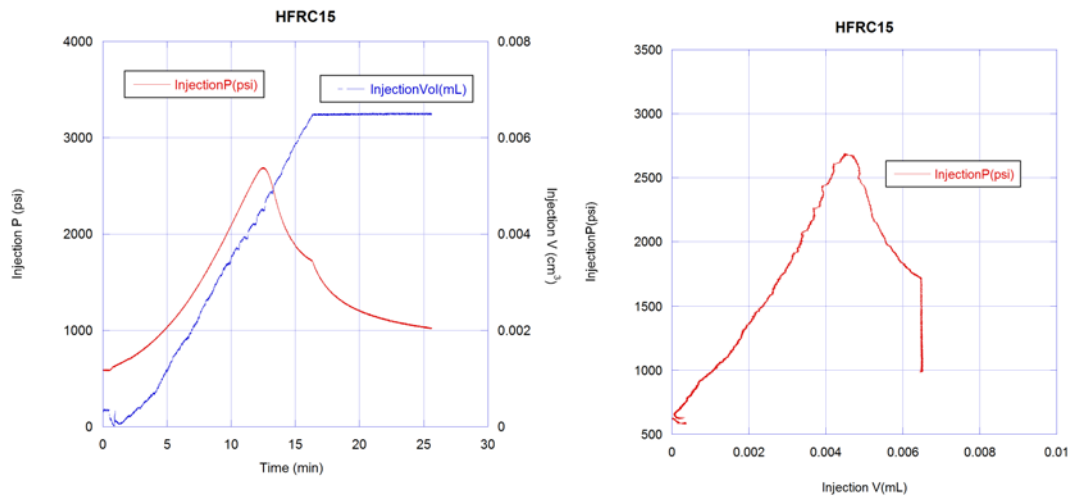


Figure 2.46. Time-injection pressure/volume history (left) and pressure-injection volume (right) results for hydraulic fracturing of a block containing “weaker” fractures.

2.1.5 Subtask 2.4– Hydraulic fracturing visualization II: Fluid viscosity/injection rate effect

Fluid viscosity effect

As seen in Figure 2.16, use of high-viscosity glycerol (1,100 cP) stabilized the fracture growth, considerably decreasing the fracture propagation velocity. In the new experiment in this Subtask, we used distilled water with 1%wt sulforhodamine B, which has a viscosity similar to water (~1cP). The resulting liquid appears dark red under room light, but unfortunately, the solution did not show an appreciable amount of fluorescence. Because the diluted solution is nearly transparent, and the fluorescence is weak, we decided to use the 1% solution to simply color the water. However, unfortunately, hydraulic fractures produced by the water injection were still very difficult to visualize even using the dyed water (Figure 2.47) (Note that previously, low-viscosity experiment on an intact glass block was conducted with liquid metal, in which the fracture was clearly visible.)

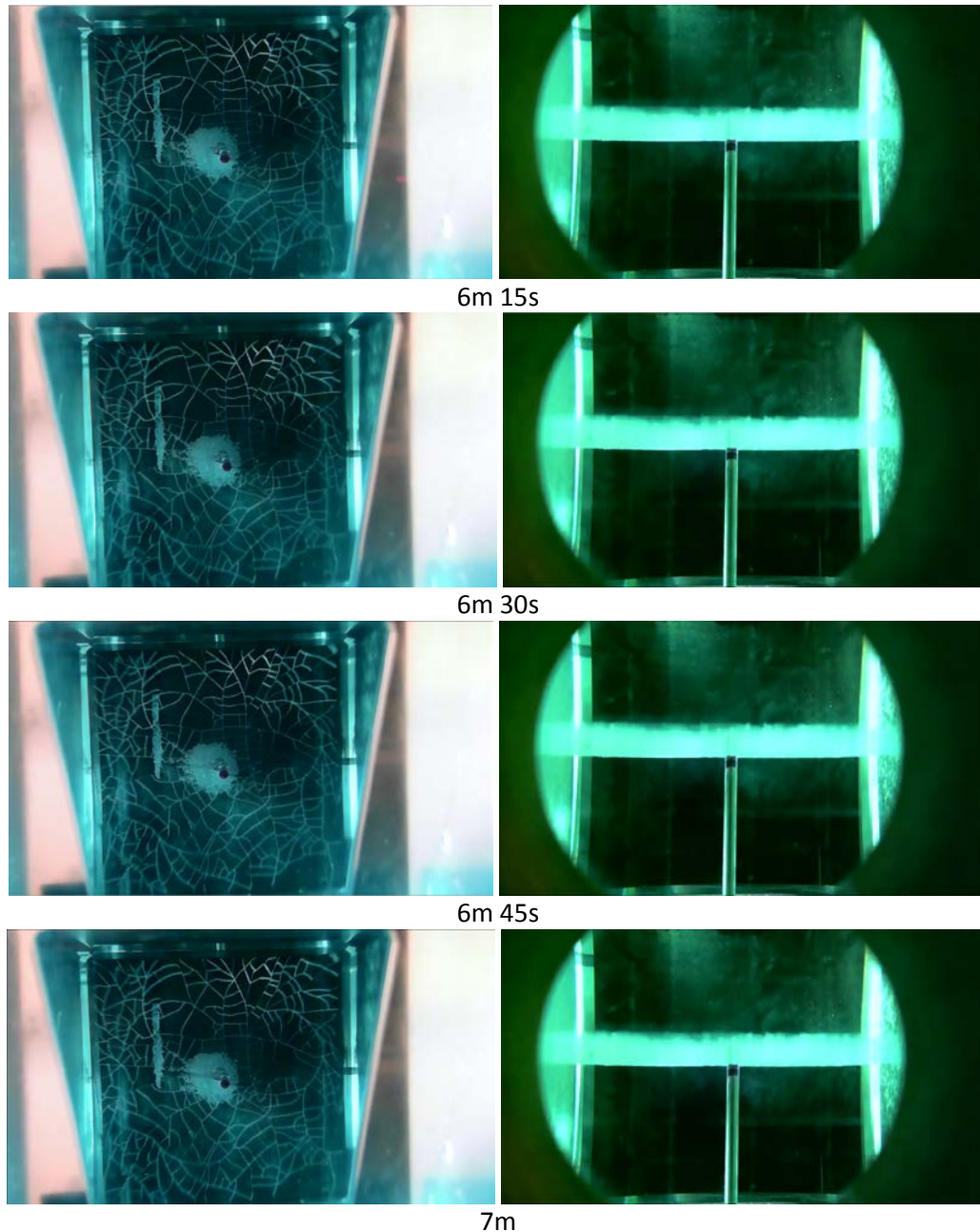


Figure 2.47. Top (left) and side (right) images of hydraulic fracturing in a glass cube containing “standard” fracture model injected with low-viscosity fluid (water). Because of the small refraction index contrast, the induced fractures are difficult to see, particularly for the side views.

Although the rapid growth of the fractures produced by injection of low-viscosity water was expected, we were somewhat surprised by a large decrease in the breakdown pressure (Figure 2.48, compared to Figures 2.42, 46). This may be attributed to the initial infiltration of the fracturing fluid into extremely thin cracks and defects around a borehole, which requires much more time with the glycerol. Another interesting finding is that the fracture produced by the fast fracturing with water resulted in hydraulic fractures that were hardly affected by the preexisting fractures. The post-experiment picture in Figure

2.48 shows an image of hydraulic fractures propagating across the laser-etched fractures, even when they intersect at a very shallow angle.

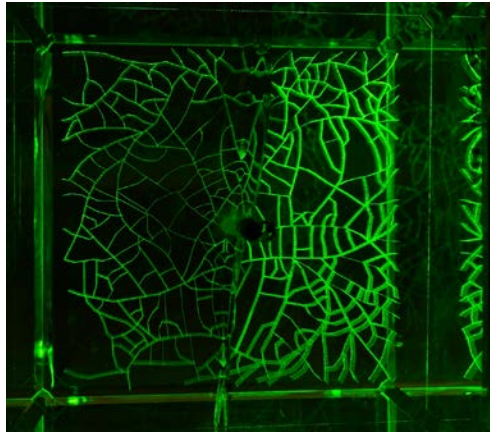


Figure 2.48. Because of the lack of (or very weak) fluorescence, the hydraulic fracture cannot be color tagged. However, from the differences in the brightness of the laser-illuminated, pre-existing fracture patterns, it can be seen that the hydraulic fracture was not affected by the preexisting fractures.

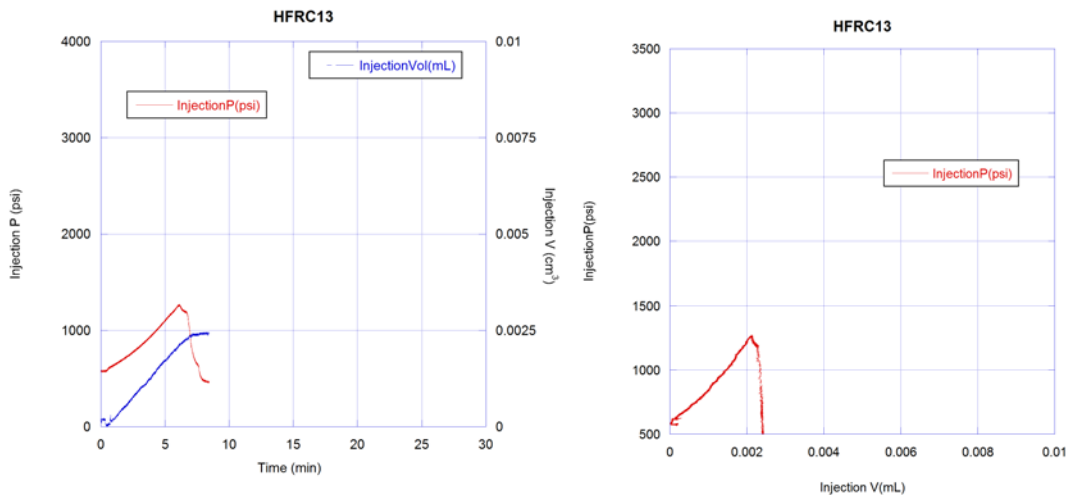


Figure 2.49. Time-injection pressure/volume history (left) and pressure-injection volume (right) results for hydraulic fracturing of a block containing “standard” fractures injected with water.

Fluid injection rate effect

Subsequently, instead of changing (reducing) the fluid viscosity, we increased the injection rate while using the high-viscosity glycerol (Figure 2.50). The injection rate was changed by increasing the driving voltage of the gear motor and also by replacing the original motor with 0.5 RPM/12V rate by a 10 RPM/12V motor. The estimated injection rate is about 30 times faster than the other experiment (because of malfunction of an injection volume measurement sensor, the actual injection rate measurement could not be made).



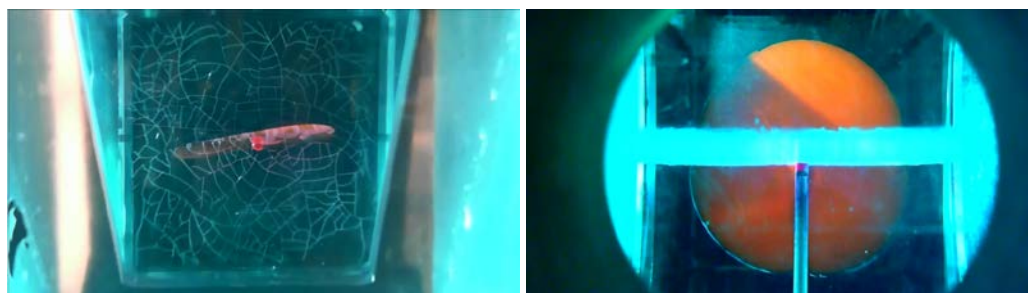
1m 30s



1m 45s



2m



2m 15s

Figure 2.50. Top (left) and side (right) images of hydraulic fracturing in a glass cube containing “standard” fracture model injected with low-viscosity fluid (water). The speed of injection was approximately 30 times faster than the case shown in Figure 2.38.

Similar to the fast fracture propagation by injection of low-viscosity fluid, fast propagation by rapid, viscous-fluid injection resulted in fracture propagation that was seemingly unaffected by the preexisting fractures (Figure 2.51). The fracturing processes involved in the two tests are quite different, however, and these can be distinguished by the presence of vacuum (which may be filled with low-pressure gas) behind the leading edge of hydraulic fractures, before the flow of the viscous fluid catches up (Figure 2.52). The breakdown pressure for this fracture was the highest among all the experiment we conducted, reaching over 4,000 psi (Figure 2.53). Again, the initial, rate-dependent infiltration of highly viscous liquid into extremely thin fractures is believed to be responsible.

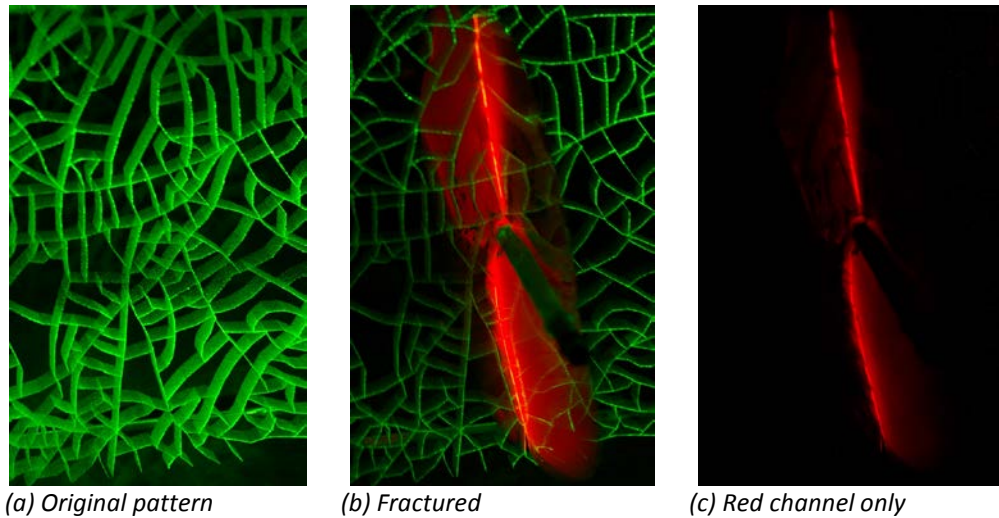


Figure 2.51. Fracturing of a “standard” fractured reservoir model at a fast injection rate. (Compare to the “standard” model in Figure 2.40.) The induced hydraulic fracture was not affected by the preexisting fractures at all.

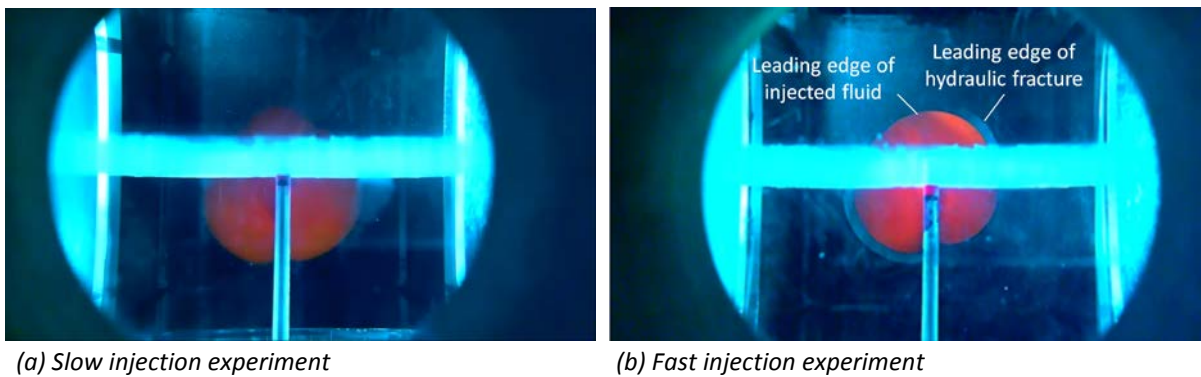


Figure 2.52. At early times during fast injection of highly viscous fluid (right), a (near-)vacuum-filled zone behind the fracture front can be seen, preceding the fluid front. This zone was not observed for slower injection of the same fluid (left).

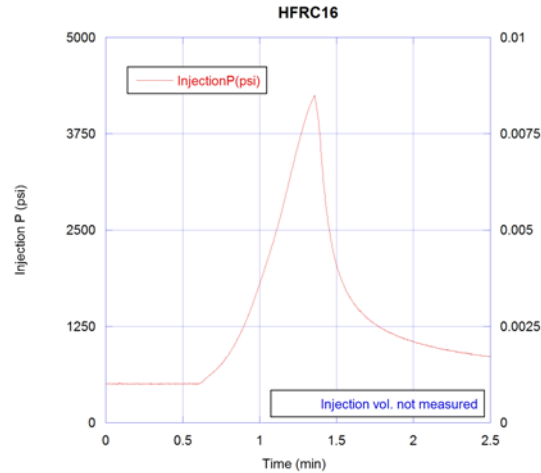


Figure 2.53. Time-injection pressure/volume history (left) and pressure-injection volume (right) results for hydraulic fracturing of a block containing “standard” fractures, with fast (30×) injection of glycerol

Complex fracture network and the fluid injection rate effect

Although observation and interpretation of hydraulic fracture growth and its interactions with the background heterogeneities can be done more easily than randomly fractured samples, the laser-etched fracture models lack the level of complexity of the random fracture network. The fracture network geometry and the strength/permeability of the randomly fractured samples can be altered by changing the initial quenching temperature and the subsequent reheating temperature and duration, respectively. Our original plan was to characterize the resulting fractures quantitatively via ultrasonic velocity (P-wave) measurements. However, actual measurements revealed that there was little difference in the velocities of the fractured samples compared to an intact sample, except for the case for which the fractures were nearly completely open and the interior of the sample was difficult to observe (Figures 2.54, 2.55a). For this reason, currently, we are using optical transparency of the sample for categorizing the samples, and using only the samples that have sufficient transparency for the experiment.

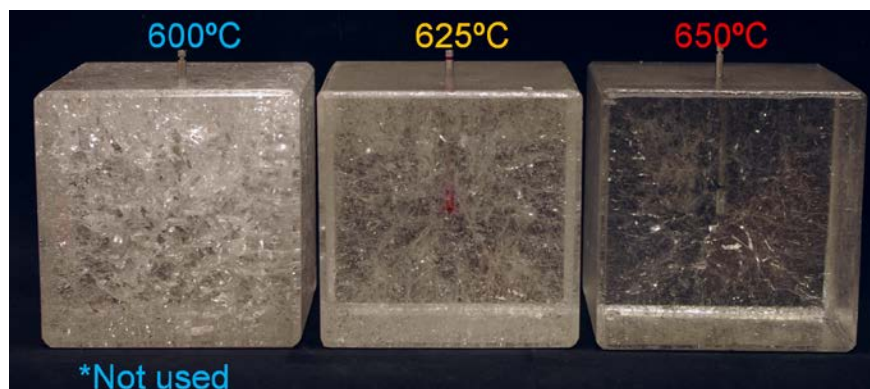


Figure 2.54. Randomly fractured soda-lime glass cube samples. The temperature values indicate the re-heating temperature of original blocks which had a similar population of contraction-induced fractures.

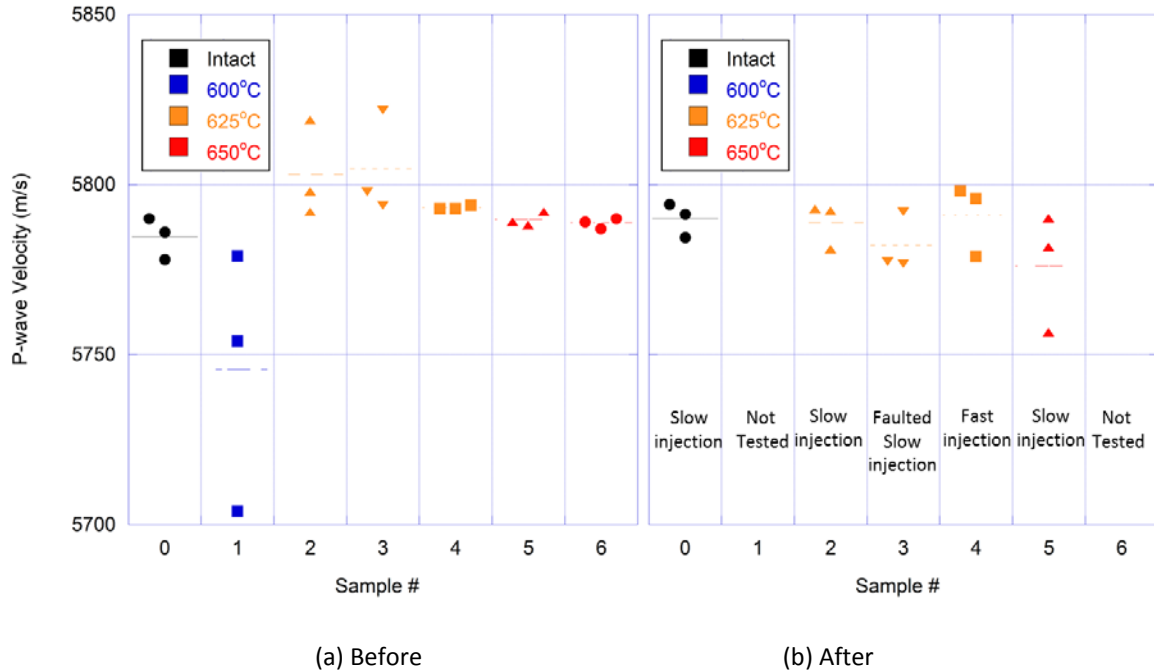


Figure 2.55. Seismic P-wave (1MHz) velocity changes before and after hydraulic fracturing experiments in the glass cubes in Figure 2.54. The measurements were made along the three axes of the each cube.

Using these samples, we conducted several hydraulic fracturing/visualization experiments, using 100% glycerol containing 1%wt sulfur-rhodamine B as the fracturing fluid. The injection rate of the fluid was either “slow” (0.425 $\mu\text{L}/\text{min}$) or “fast” (8.50 $\mu\text{L}/\text{min}$) which is 20 times the rate of the slow injection. The post-experiment images (enhanced by the fluorescence of the injected fluid illuminated by long-wavelength UV light) in Figure 2.57 show that, via slow injection, the “strong block” prepared at 650°C resulted in hydraulic fractures similar to an intact block, which link preexisting fractures in the background. In contrast, the “weak block” (prepared at 625°C) produced a dendritic network fractures which were mostly preexisting with the slow injection. However, when a similarly fractured sample is injected at the “fast” injection rate, well-defined, planar hydraulic fractures similar to the intact and strong blocks were produced, which cross-cut and interconnected the background preexisting fractures. The differences in the fracturing behavior resulting from the slow and fast injection rate can be seen more clearly from the images (video images) obtained during the experiment (Figure 2.58). For the “fast” injection experiment, when the planar hydraulic fracture was propagating, the leading edge of the fractures did not seem to contain any fluid (which can be distinguished from a fluid filled fracture, because a vacuum/air filled fracture exhibit well-defined edge thanks to the strong contrast in the index of refraction).

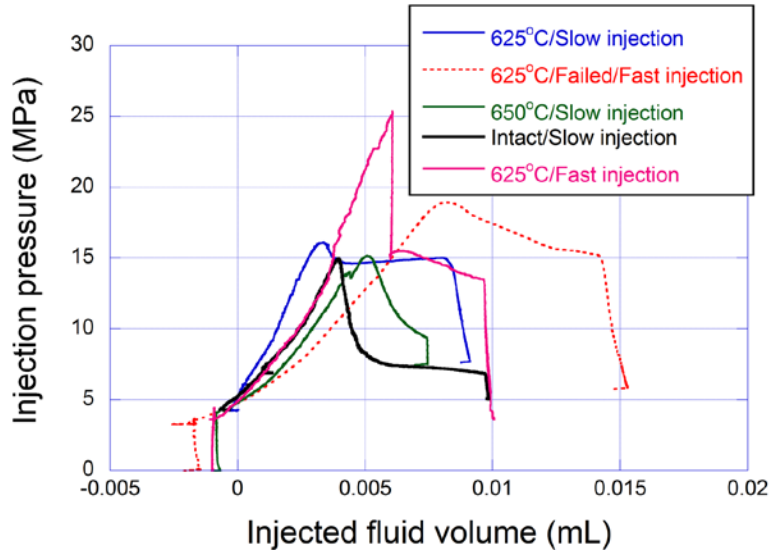


Figure 2.56. Injection pressure-volume relationships measured in various tests. The “slow” injection test was conducted at a rate of $0.425 \mu\text{L}/\text{min}$, while the “fast” injection test was conducted at 20 times that rate.

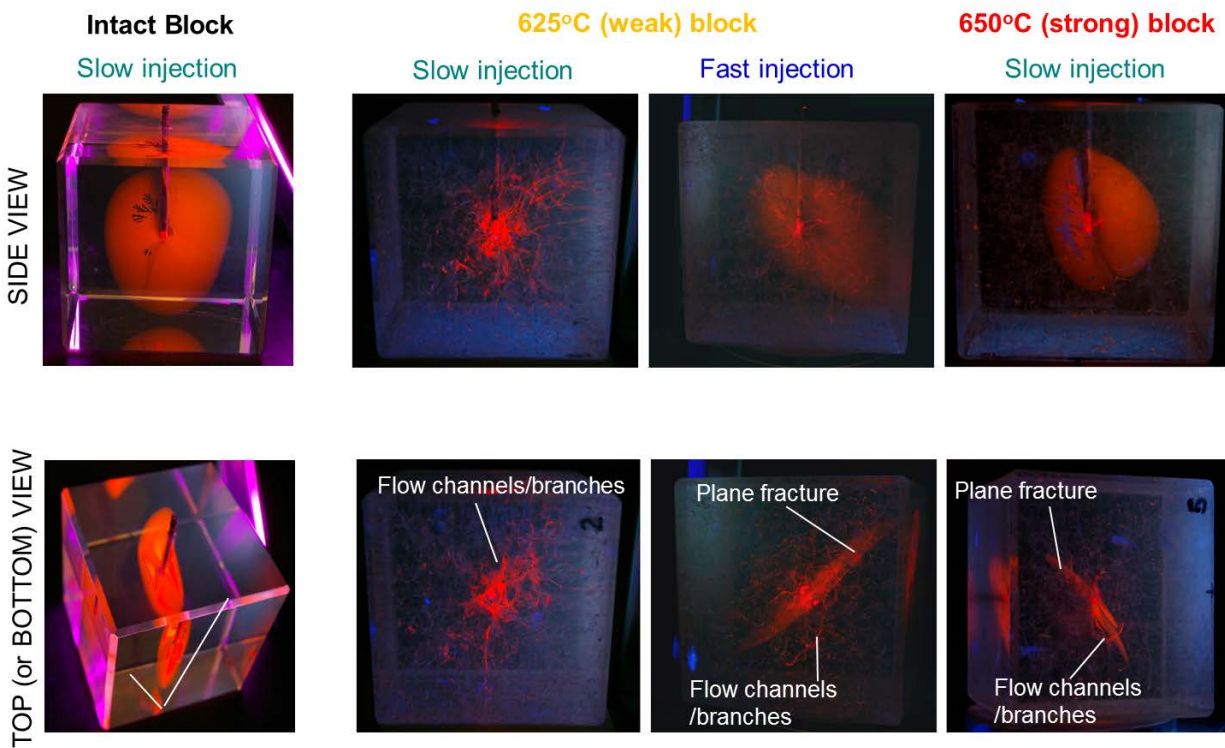
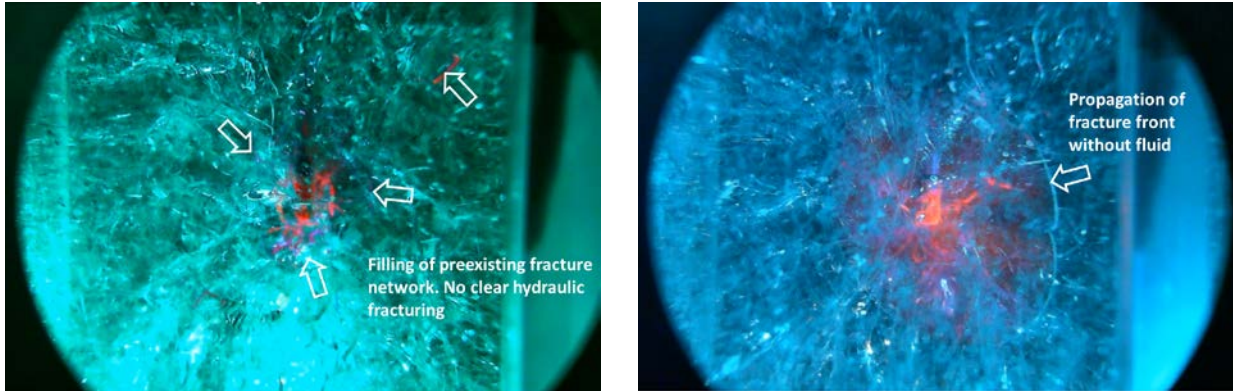


Figure 2.57. Observed hydraulically induced fracture images enhanced by fluorescence induced by long-wavelength UV light.

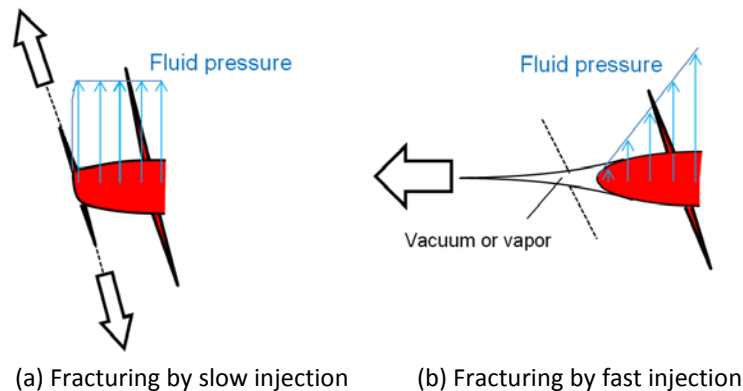


(a) Fracturing by slow injection

(b) Fracturing by fast injection

Figure 2.58. Hydraulic fracturing within “weak” fractured block. Different fracturing behavior in glass samples containing fracture networks with similar fracture properties, subjected to either “slow” or “fast” injection of fracturing fluid. Sample with fast injection, which exhibited well-defined, flat hydraulic fractures, showed planar fracture fronts which were not filled with the fracturing fluid.

The dramatically different behavior and the resulting geometry of the hydraulic fracture network between the “fast” and “slow”-injection induced hydraulic fractures can be explained by possible different fracturing regimes near the leading edge of a propagating fracture (Figure 2.59). A strong pressure gradient along a fracture caused by fast injection results in a “wedge effect” which produces vacuum or vapor filled zone behind a leading edge of the fracture. In this zone, the fluid pressure is very low, and the preexisting fractures and weak interfaces tend not to be activated by the hydraulic fracture, when frictionally stabilized under the confining stress. As a consequence, the hydraulic fracture can jump across the discontinuity, maintaining the original plane of propagation. In contrast, if the pressure gradient caused by the slow injection is small, high fluid pressure can reach the tip of a propagating hydraulic fracture, preferentially activating preexisting weaknesses.



(a) Fracturing by slow injection

(b) Fracturing by fast injection

Figure 2.59. Possible mechanisms for the different fracturing behavior cause by slow and fast injection. The low fluid pressure near the leading edge of propagating hydraulic fractures may fail to activate the weak, preexisting interfaces (fractures), resulting in “crossing” of the hydraulic fractures across the interfaces and continued fracturing of the intact matrix.

Correlation with acoustic emission locations

In November 2015, we finally completed the implementation of an acoustic emission monitoring system (AMSY-6, Vallen Systems Co.) integrated with the true-triaxial loading frame with the optical visualization setup (Figure 2.60). This was made possible by leveraged funding from another project funded by DOE (OBES office) which focuses on the fundamental processes in rock fracturing and their geophysical monitoring. This system allows us to monitor acoustic emissions resulting from hydraulic fracturing using 12 miniature piezoelectric sensors (each cube face has two stations). Originally our plan was to simply count acoustic emissions using then available 2-channel system (Physical Acoustics). However, leveraged funding from the Office of Basic Energy Sciences program allowed us to procure the monitoring system capable of real-time location of AE events during experiments.

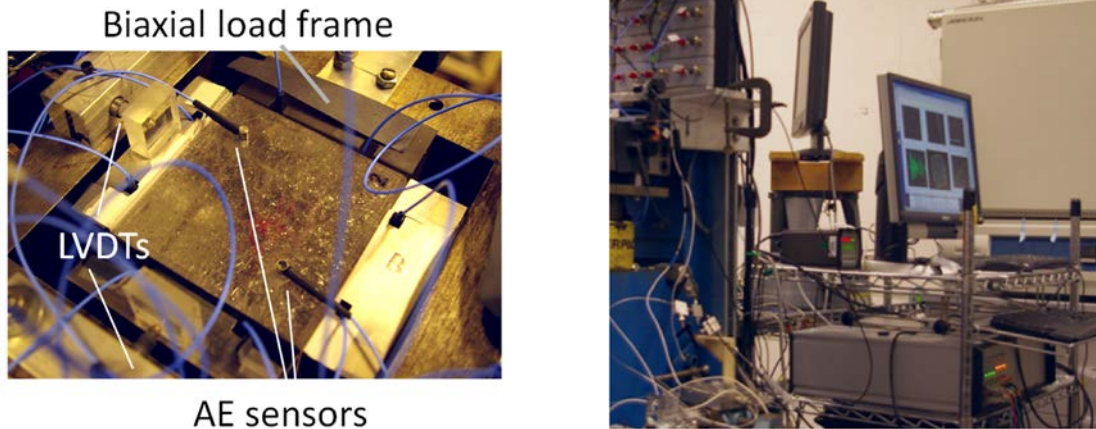


Figure 2.60. A 12-channel acoustic emission monitoring system (AMSY-6, Vallen Systems) integrated with the true-triaxial hydraulic fracturing visualization system.

In Figure 2.61, the AE history obtained during the “fast injection experiment”. (A related injection pressure-volume plot is included in Figure 2.5.) After about 150 s after the start of injection (started at $t \sim 750$ seconds), breakdown in the injection pressure occurred, and a large number of AEs were observed. These events were grouped by 150 s time intervals, and the related locations of the events in the sample block were determined. In Figure 2.62, the spatial distribution of the located events, and the images of the hydraulic fractures corresponding to the time intervals are shown. What is interesting, although somewhat expected, is that: (1) many AEs occurring at the early stage of the fracturing are located far away from the hydraulic fractures, indicating “dry” events; and (2) as the hydraulic fractures grow, the AE cloud collapses onto a plane along which the hydraulic fracture is propagating.

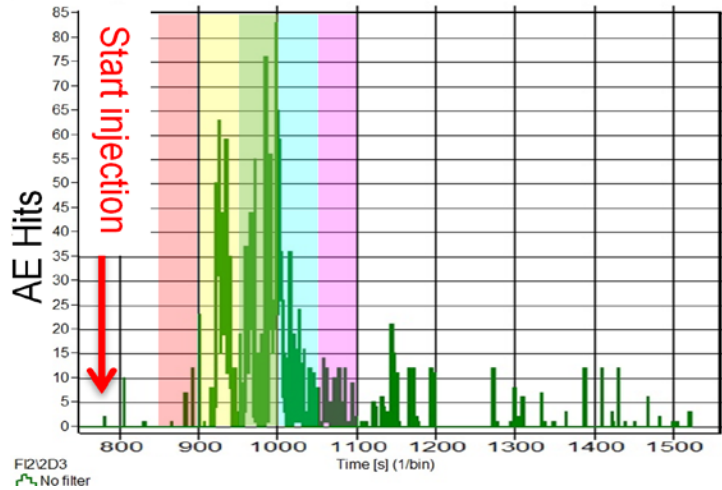


Figure 2.61. Acoustic emission count history for the “fast” injection experiment. The AE events are grouped by time with 150 s intervals.

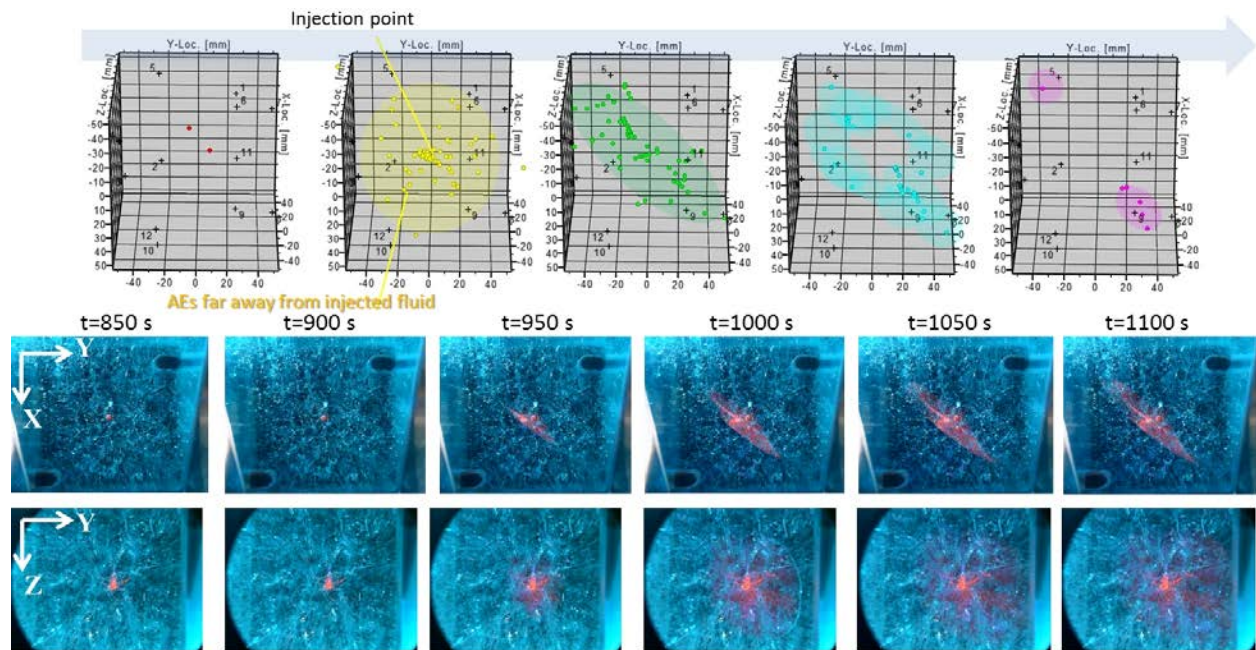


Figure 2.62 Correlated views of AE locations (top) and the visualized images of hydraulic fracturing in both top view (middle row) (similar angle of view as the AE plots) and side view (bottom row).

2.1.6 Final remarks on the laboratory experiments

The glass samples used for optical visualization caused some unanticipated problems, mainly because the thickness of the induced fractures was extremely thin, which resulted in (1) poor X-ray CT visibility, (2) poor static deformation measurements of the samples (the obtained measurements were extremely noisy and unusable), (3) no measurable changes in the acoustic properties (for static mechanical property changes before and after the experiments) and permeability (under elevated confining stress was applied).

In Figure 2.63, an example of loading platen displacements during the hydraulic fracturing experiment in Figure 2.62 are shown, correlated to the fluid injection pressure. With our currently available displacement sensors (LVDTs were used) and data acquisition system, the resulting data was very noisy, including strong drifts in the signal (which was corrected in this plot). However, the result does show some anisotropic expansions (and a small contraction) of the cube-shaped sample when hydraulic fractures were produced. In contrast, anisotropic sample mechanical property changes, reflected in the seismic velocity changes, were hardly measurable. As seen in Figure 2.55, the effect of preexisting fractures on the seismic P-wave velocity (1 MHz) was very small, and the velocity changed little by the induced fractures. (Note that the velocity measurement error is approximately 1 to 2% (50–100 m/s). We believe the high (dynamic) stiffness of the fluid-filled thin fractures is responsible for the small velocity changes.

For the experiments conducted in this project, the samples had no measurable permeability when subjected to effective confining stress, even after the hydraulic fractures are introduced. This is because the fractures in the samples were well mated, and only small external stress is needed to seal the fractures against flow of viscous fluid. In order to evaluate the degree of “permeability enhancement” in different experiments, we examined the flow rate of the injected fluid (100% glycerol) at an approximate post-breakdown residual state (when pressure changes become small), normalized by the injection pressure:

$$K = \frac{1}{P(t_{residual})} \frac{dV(t_{residual})}{dt}$$

where P , V are the injection fluid pressure and volume, respectively, and $t_{residual}$ is the time when the injection pressure becomes (approximately) unchanged, typically at the end of each experiment. Although this is by no means an accurate measure of the reservoir rock permeability, using available data in our laboratory experiment, the parameter provides some ideas about the changes in the permeability (i.e., a permeability proxy) for the same fracturing fluid, assuming that the fluid pressure at the leading edge of the hydraulically connect fracture network is small. The breakdown and residual pressures, and the above “residual injectivity” parameters, are shown in Table 2.3. The samples shown in the table correspond to the randomly fractured samples in Figure 2.56. The results indicate that slow injection resulted in smaller permeability (changes) for both “weak” (625 °C) and “strong” (650 °C) samples (Note that weaker sample contains a large number of connected preexisting fractures). In contrast, the sample with fast injection resulted in significantly larger permeability. The very high permeability in the prematurely failed sample is possibly due to the presence of a high-permeability “fault” in the sample to which the induced hydraulic fractures connected.

Although the above issues (especially 1) appear to be less problematic for hydraulic fractures in natural rock (shale), the water-sensitive, swelling behavior caused different kinds of difficulties during sample preparation. To combat some of the problems, for similar experiments conducted in the future, use of micro-scale proppant may be effective during the injection experiment to increase and maintain the fracture aperture. For sample preparation of water-sensitive shales, a dedicated core preparation setup which can use high-salinity brine compatible with the rock may be needed, particularly when small-diameter borehole is to be drilled in the rock.

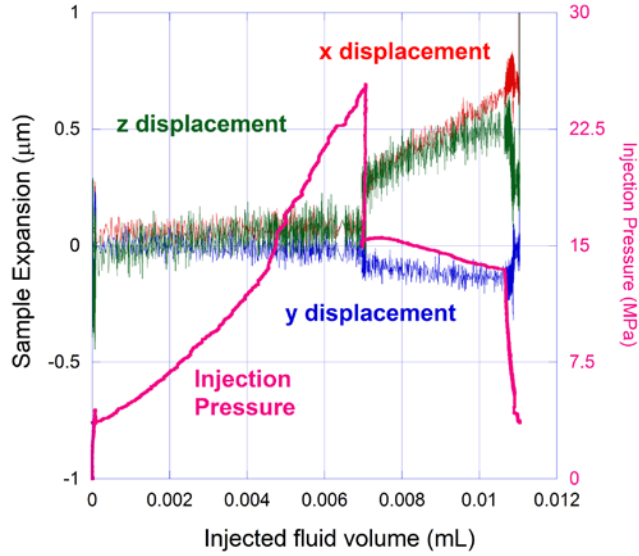


Figure 2.63 Platen displacements correlated with the hydraulic fracturing of “strong” block by “fast injection” (same as the sample used in Figure 2.62). Note that the platen displacements are very small (less than 0.5 microns for the 10cm cube sample) and the data is very noisy. The original data also contained strong drifts in time, which were corrected in this figure.

Table 2.3. Assessment of permeability changes

Sample	P _{breakdown} (MPa)	P _{residual} (MPa)	Residual injectivity (m ³ /Pa.s)	Comment
Intact	15.0	6.9	2.7 x 10 ⁻¹⁸	
625°C Slow	16.6	15.0	1.7 x 10 ⁻¹⁸	
625°C Slow	19.0	15.2	13.1 x 10 ⁻¹⁸	Prematurely failed/faulted sample
650°C Slow	15.2	9.4	1.2 x 10 ⁻¹⁸	
625°C Fast	25.3	13.3	8.8 x 10 ⁻¹⁸	

*Here, this quantity is used as a surrogate for the permeability of the fractured block after hydraulic fractures are induced in the sample (i.e. static permeability)

2.2 Task 3.0 Numerical Modeling

In the numerical modeling task we

- Make improvements and modifications to the TOUGH-RBSN code, which are necessary for simulating hydraulic fracturing, and verify the performance of the new algorithms.
- Model and interpret the laboratory hydraulic fracturing experiments.
- Upscale the effects observed at the core scale to the intermediate field scale, with the quantitative links provided by the numerical model verified at the small scale.

In the following subsections 3.1.to 3.5, the work and results are reported for each modeling subtask.

2.2.1 Subtask 3.1–Code modification and verification of TOUGH-RBSN hydraulic fracturing algorithms (Phase I)

TOUGH-RBSN has been modified and verified for modeling hydraulic fracturing, including fracturing within complex fractured rock.

According to the original plan, the following key code modifications and verifications have been accomplished:

- Code modification and testing of modeling anisotropic elastic and strength behavior (e.g. shales such as Opalinus Clay)
- Code modification and testing of modeling existing fractures in contact under compressive stress
- Code verification of fluid-driven fracture propagation

The modification and testing of modeling anisotropic elastic and strength behavior was completed and tested. The elastic and strength anisotropy algorithms were tested and verified for modeling of laboratory scale samples under compression. The code modification and testing for modeling existing fractures subjected to compressive stress (and therefore, with contacting fracture surfaces) was completed. (Note that the original RBSN code could not consider compressive contact forces.) Figure 3.1 shows RBSN simulation of uniaxial compression tests on 2-D rectangular samples. The anisotropy (bedding planes) of the sample varies against the (axial) loading direction, at angles of $\beta = 0^\circ, 15^\circ, 30^\circ, 45^\circ, 60^\circ, 75^\circ, 90^\circ$. The resulting stress-strain responses show that the apparent elastic moduli and peak stresses varies as a function of the bedding angle, typical characteristics of the mechanical properties of shales such as Opalinus Clay. In Figure 3.2, fracture patterns are depicted in the deformed state for $\beta = 0^\circ, 30^\circ, 45^\circ, 60^\circ, 90^\circ$. For the samples with the bedding planes parallel and perpendicular to the loading direction, the fracture patterns do not have apparent directionality (Figure 3-2a and e). In contrast, for the cases with bedding planes oblique to the loading direction, the direction of fracturing tends to be biased towards the bedding directions (Figure 3.2b to d).

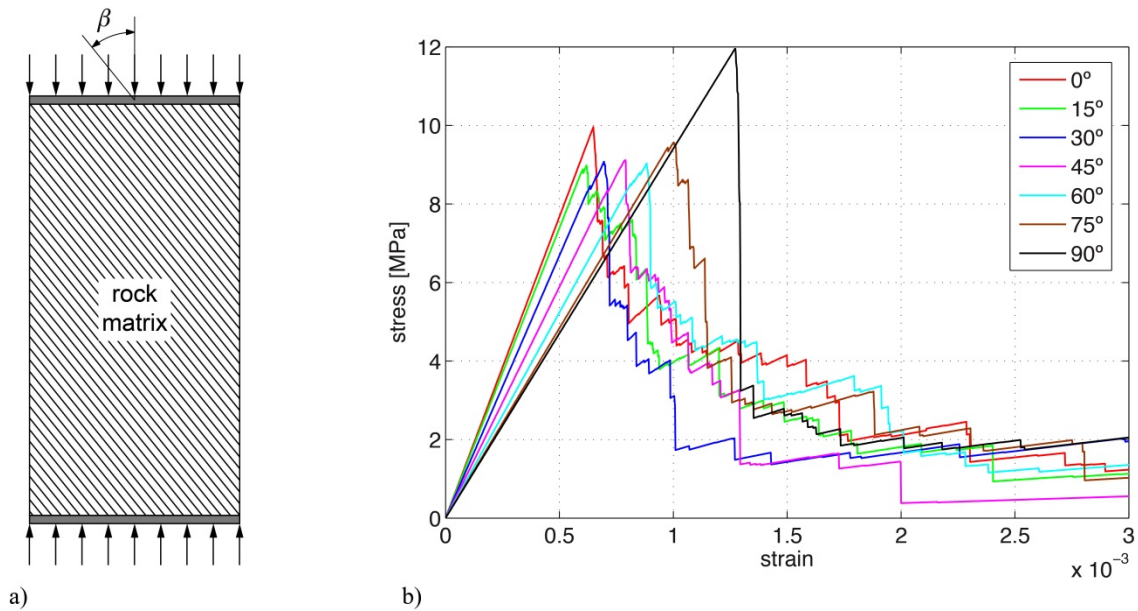


Figure 3.1. Uniaxial compression tests: a) schematic drawing for the test program; and b) stress-strain curves with various orientations of bedding plane with regard to the loading axis.

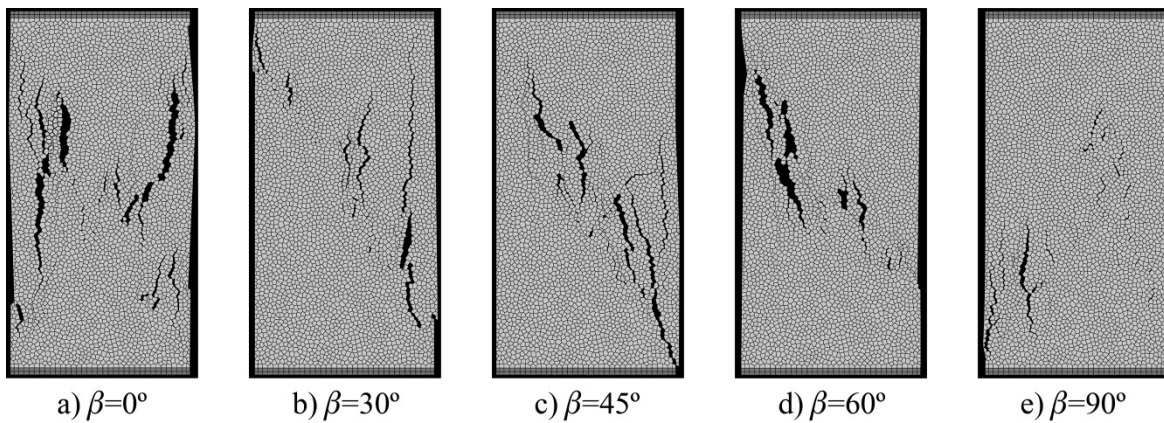


Figure 3.2. Fracture patterns in deformed shapes of the model. Note that the mesh geometry is identical, but the bedding orientation is internally changed in the simulations.

Subsequently, the numerical code was tested for fluid-driven fracture propagation of a single fracture [this particular problem is called the Khristianovic-Geertsma-de Klerk (KGD) model]. Figure 3.3a shows one example in which a two dimensional rectangular domain with dimensions of 120×100 m was prepared and discretized with graded mesh density for computational efficiency. At the left boundary where the injection point is located, a symmetric boundary condition was applied. The KGD model is for the cross section of an elliptical fracture, based on the linear elastic fracture mechanics theory, while uniform fluid pressure is applied along the length of the fracture.

The resulting fracture profiles from the simulations are plotted in Figure 3.3b. A single hydraulically driven fracture advances through the domain with increasing injection time. From the model deformation, the aperture width is calculated and compared with the KGD analytical solution. The fracture profile retains elliptic shape, with the fracture length and the aperture as the major and minor radii of the ellipse.

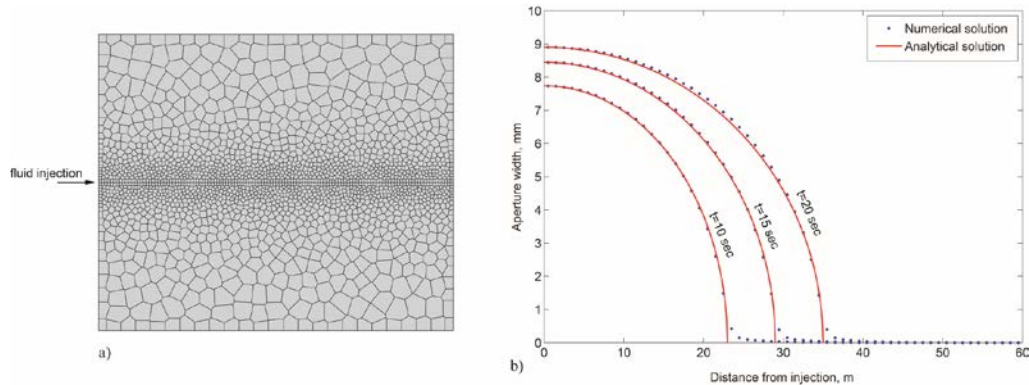


Figure 3.3. KGD model test: a) model set up; and b) aperture width profiles along the fracture.

2.2.2 Subtask 3.2–Numerical model setup and preliminary simulation of complex hydraulic fracturing (Phase I)

The main objective of this task was to determine the best option of modeling the laboratory experiments performed under Task 2 considering the capabilities and limitations of the numerical model. More specifically Subtask 3.2 was accomplished by

- Testing and verification of the applicability of the TOUGH-RBSN for the modeling complex hydraulic fracturing in core samples
- Model setup and preliminary simulation of the initial laboratory experiments
- Recommending ideal test parameters for further laboratory experiments

Initially, we conducted initial simulations of fracture propagation within rock containing a preexisting network of discrete fractures using a generic model of a complex fracture network involving 40 fractures (Figure 3.3). This was the first test and demonstration of capability of TOUGH-RBSN to model fracture propagation through a network of pre-existing fractures.

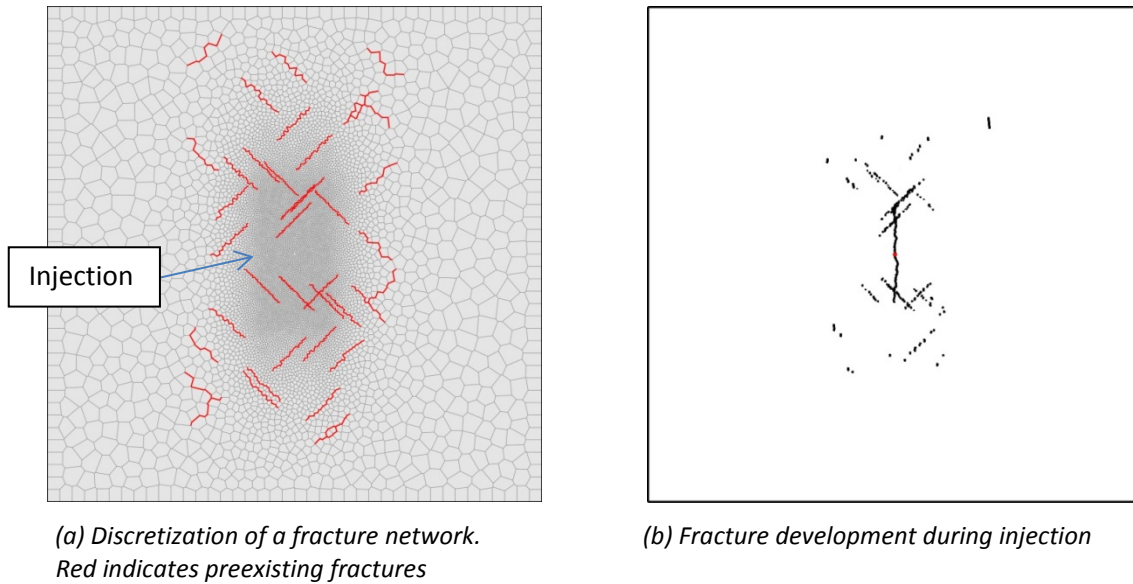


Figure 3.4. Initial demonstration model simulations of fracture propagation through a discrete fracture network

Next we modeled samples with actual geometry of pre-existing fractures designed in the laboratory experiments under Task 2. We successfully mapped the actual geometry of fractures within a glass sample developed under Task 2.2, onto our unstructured Voronoi grid (Figure 3.4). In principle, there is no limitation on the number of fractures that can be discretized using the TOUGH-RBSN. However, finer element discretization for more accurate representation of the fracture geometry quickly increases the computational costs. We have developed several models with different mesh density and modeling fracturing using both finer and coarser mesh discretization (Figure 3.5).

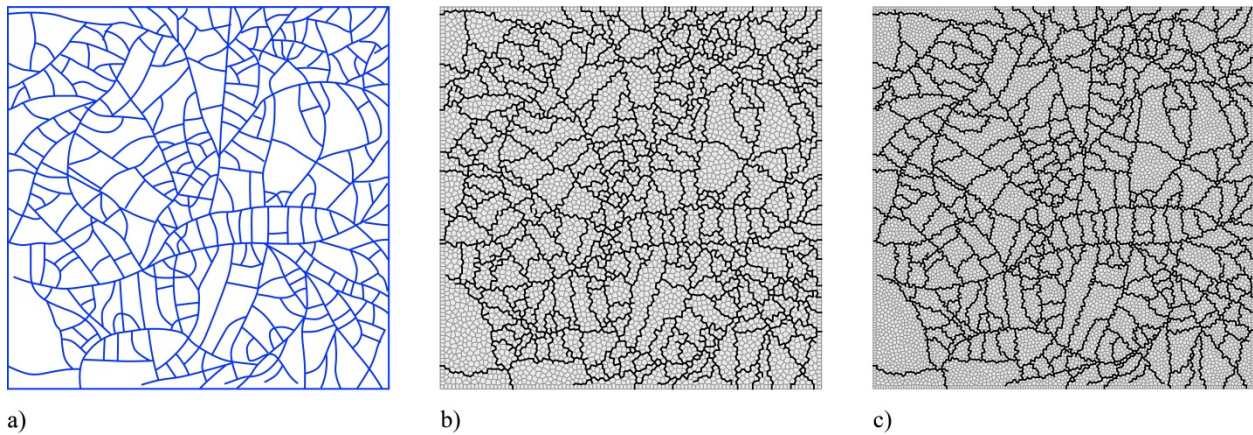


Figure 3.5. a) Discrete fracture network of a glass sample; and mapping of the fracture geometry onto unstructured Voronoi grid with different mesh density: b) 5000 cells and c) 10000 cells, approximately.

We have conducted sensitivity studies of fracture and injection parameters. Note that it is crucial to represent the storage of the fluid within the injection system correctly (including the storage attributed to the compliance of the wellbore) as well as the fluid storage created by the opening of the fracture inside the sample. Because these parameters are not determined in the laboratory experiments at this point, in these preliminary simulations, we focus on the qualitative aspects of the results.

The model properties are for soda-lime glass which is simply assumed to have zero permeability and porosity. Note that the compressibility for the matrix is also zero (rigid body). Other mechanical properties of the glass are as follows: Young's modulus $E = 73.8$ GPa, tensile strength $f_t = 30$ MPa. A Mohr-Coulomb fracture criterion is used to represent brittle failure of the RBSN elements, for which cohesive strength $c = 22.5$ MPa and internal friction angle $\varphi = 45^\circ$. Since the glass material may undergo a very brittle fracturing, the rate of injection should be very small to capture the fracture propagation. In the simulations performed under this subtask, the rate of water injection was assumed to be 2×10^{-7} kg/s per unit millimeter. The model was subjected to anisotropic confining stresses, for which 7.24 MPa and 4.83 MPa were applied at the boundary edges.

For pre-existing fractures, it was assumed that their mechanical properties are reduced by a half of the intact glass. However, the permeability of these fractures are assumed to be zero and do not affect the hydrological behavior unless they are mechanically activated. Once a new fracture occurs or a pre-existing fracture is activated, the mechanical resistance is completely removed and the permeability and the porosity were drastically increased (e.g., 1 Darcy of permeability; 0.8 of porosity).

The simulation results with such input data showed that hydraulic fracturing occurred in preferred directions due to the anisotropic stress conditions and the degraded mechanical properties of the pre-existing fracture network (Figure 3.6a). Also, the simulated pressure distribution shows that the propagation of fluid fronts through the fracture paths coincides with that of the hydraulic fractures (Figure 3.6b).

One of the controllable parameters determining the fracture propagation speed is the storage of elastic energy in the injection system. In numerical simulations, this can be controlled by the compressibility of the borehole domain. In this study we qualitatively compared the fracture propagation speeds by elapsed time from the fracture initiation to complete fracture propagation to the outer boundary. Figure 3.7 presents the pressure evolutions at the borehole with two different compressibility coefficients: the blue curve is for zero compressibility, while the red curve is for 4.6×10^{-9} Pa⁻¹. With the same injection rate, the higher compressibility takes longer in the ascending branch up to the peak pressure to initiate hydraulic fracturing. However, in the post-peak region, the higher compressibility results in rapid fracture propagation with a sharp drop of the pressure; whereas the zero compressibility makes the fractures to stop and go with intermittent pressure accumulation and propagation.

The analyses conducted under this subtask indicated that a stiff (low storage) injection system is desirable for controlling the fracture propagation in a gradual process rather than an instantaneous manner.

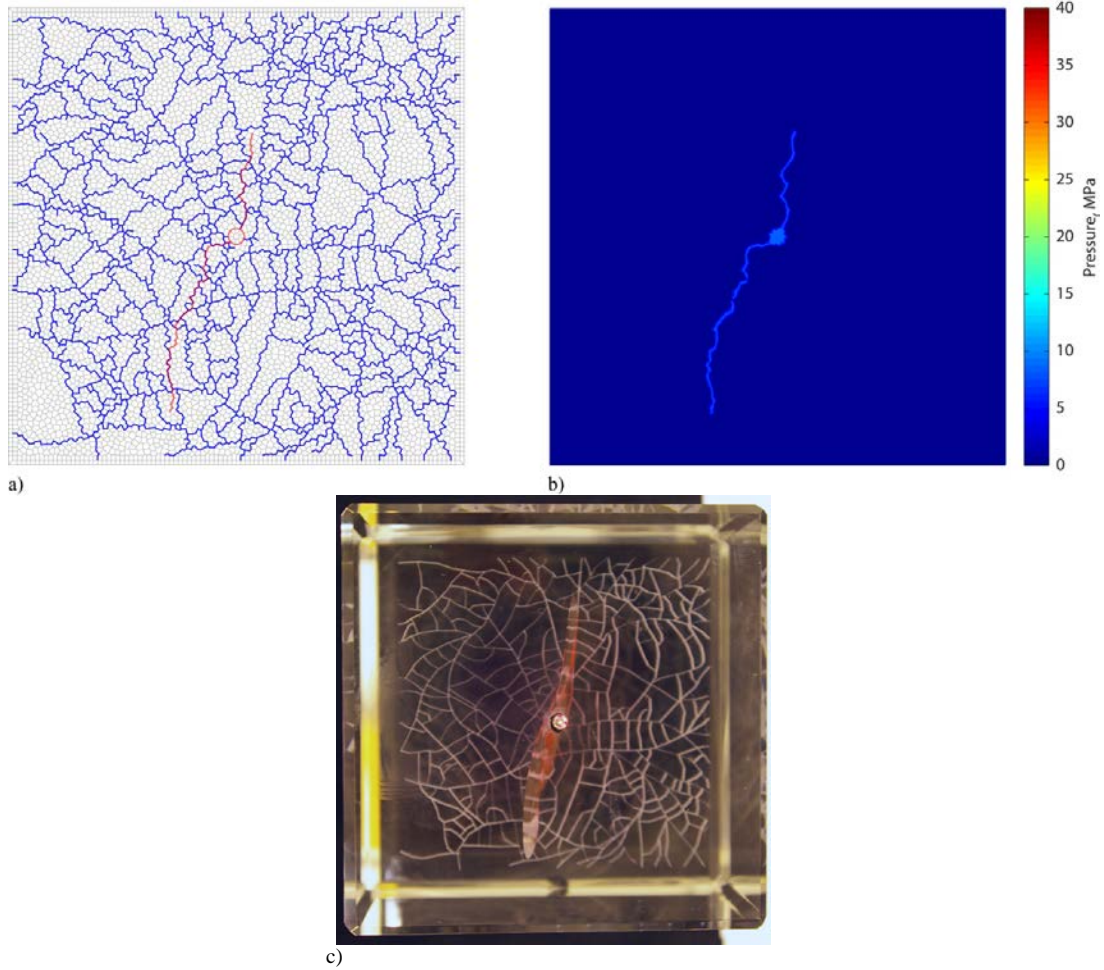


Figure 3.6. a) hydraulic fracturing which mostly follows the pre-existing fractures; and b) contour plot of pressure distribution at the same time step. The results agree well with laboratory-observed fracturing pattern c)

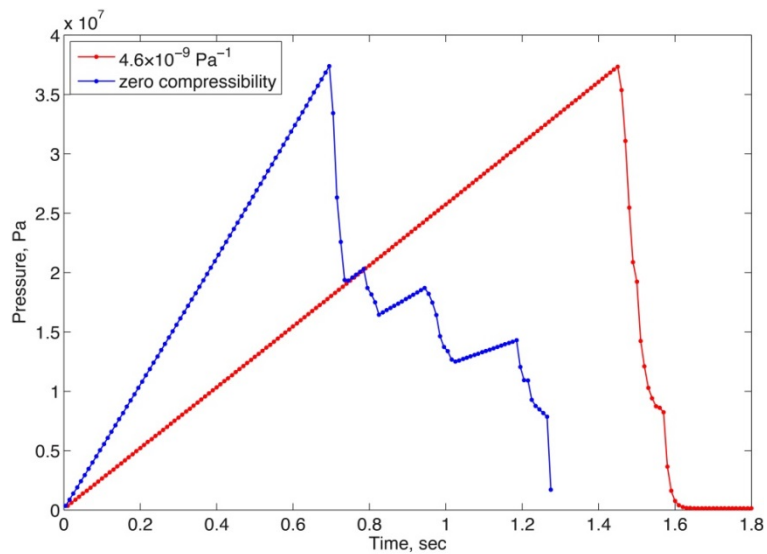


Figure 3.7. Pressure evolution at the borehole with different compressibility coefficients for the borehole domain. Note that the other parameters and conditions are identical in these two cases.

2.2.3 Subtask 3.3–Model prediction of laboratory hydraulic fracturing experiments (Phase I)

In the previous Subtask 3.2, a number of models (numerical grids) were already construct of the actual experimental geometry and mapped the exact heterogeneous features of the 3D-laser engraved fracture pattern in a glass sample. The simulation under the previous Subtask 3.2 indicated the fracturing process would be rapid in a brittle manner, which would be undesirable for capturing fracture propagation in the experiments. To avoid such rapid fracture propagation it was decided to initiate notches around the borehole that were expected to lengthen the period of fracturing process and control the fracture length. Therefore, the model prediction of the actual experiments the influence of such notches on the fracturing process was investigated.

In the RBSN models, notches or other types of discontinuous material defects can be easily represented by breaking/damaging the lattice elements. From the resulting hydraulic fracture patterns performed in Subtask 3.2, the elements were manually chosen to introduce the notches around the borehole (See Figure 3.8). For the elements representing the notches, the mechanical resistance in tension was completely removed and the permeability and the porosity were initially increased like when they are mechanically activated for hydraulic fracturing.

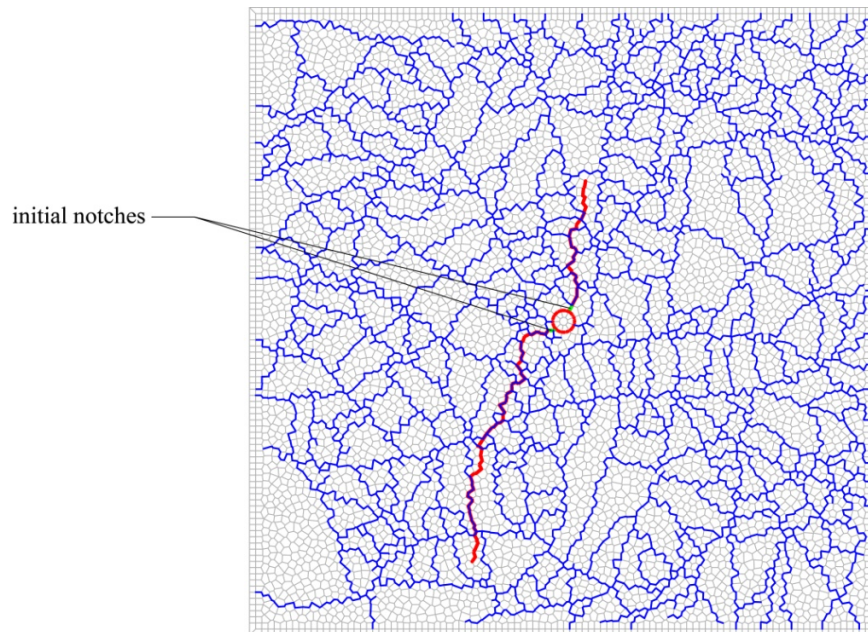


Figure 3.8. Introduction of initial notches around the borehole. The location of the notches was determined by the resulting hydraulic fractures (illustrated by red lines) without notch.

The simulation was conducted with the non-zero compressibility ($4.6 \times 10^{-9} \text{ Pa}^{-1}$) for the borehole domain, and its result was compared with the case (red curve) in Figure 3.6. The hydraulic fracturing process without notches was completed very abruptly in about 0.15 sec from the high level of triggering pressure. However, as depicted by the blue curve in Figure 3.9, the presence of the initial notches lowers the triggering pressure. The peak pressure is lowered in the presence of a notch because it is easier to propagate a fracture from an initial defect, then to initiate a new fracture from an intact material. Moreover, geometrical effects of the notches tend to concentrate the stress induced by the

fluid pressure to the crack tip. Early triggering means less storage of fluid in the injection system, thus the hydraulic fractures propagate more gradually with intermittent pressure accumulation and release at the borehole.

This result from this model prediction indicated the possibility that the fracture propagation can be halted by intermittently halting the fluid injection, e.g. when the fracture has propagated only half way to the specimen boundary. This makes it possible to study in more detail the fracture propagation processes for example when using different fluid viscosity or injection rate. As it turned out, a more gradual fracture propagation was achieved in the experiments under Task 2 when notches were introduced in the injection hole, and thus this effect was correctly predicted in the model simulations with TOUGH-RBSN.

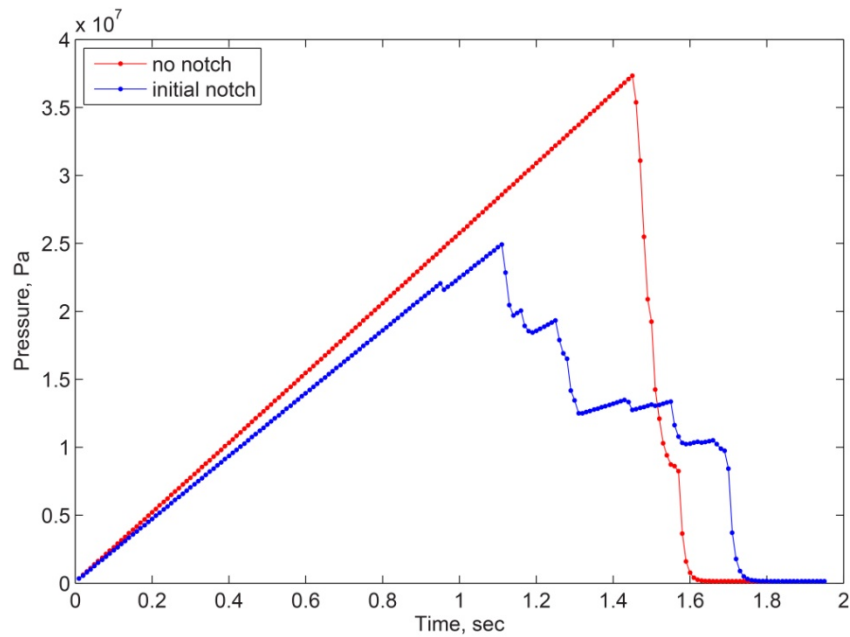


Figure 3.9. Comparison of pressure evolutions according to the presence of the initial notches.

2.2.4 Subtask 3.4–Interpretative numerical modeling of laboratory experiments (Phase II)

Interpretative modeling of the laboratory experiments performed in Task 2, were conducted once laboratory data were available. In the laboratory experiments, a comparative study was conducted for two cases of fluid injection with different viscosities, using distilled glycerol and water. Under Subtask 3.4, we modeled these experiments in order to provide interpretation of hydraulic fracturing processes from the simulation results.

To reproduce the experiments, firstly the numerical simulator (TOUGH-RBSN) had to be modified since the original flow simulator, TOUGH2, considers fluid viscosity through pre-defined functions of temperature and pressure, and does not allow to explicitly assign a certain viscosity value. We made some modifications to the TOUGH2 allowing us set the viscosity variables so that various fluids used in the experiments can be modeled. Next, the injection rate was estimated for the actual test based on the

injection volume history. By assuming that the model thickness is equivalent to those of the fracture reservoir in the test specimen (=0.25"), the injection rate is approximately 1.0×10^{-5} cm³/s per unit centimeter thickness. Two types of fluids are injected for a comparative study: glycerol and water; of which the viscosities are 1,100 cP and 1 cP, respectively.

In these simulations it was assumed that the glass matrix is impermeable, which was modeled as zero permeability, porosity, and compressibility. The mechanical properties used for the simulations are as follows: Young's modulus $E = 73.8$ GPa, tensile strength $f_t = 30$ MPa. A Mohr-Coulomb fracture criterion was used to determine the failure of discrete elements, for which the cohesive strength $c = 22.5$ MPa and the internal friction angle $\varphi = 45^\circ$. The specimen was subjected to anisotropic confining stresses, $\sigma_x:\sigma_y = 7.24:4.83$ MPa, as applied in the preliminary simulations and in the experiments.

Softer and weaker mechanical properties were assigned for the pre-existing fractures, in which Young's modulus and tensile strength were initially degraded by a half. According to the defect density for the etched pre-existing fractures in the experiments, the mechanical properties in the model maybe estimated based on the expected weakening. The hydrological properties of the pre-existing fractures were set to be same as those of intact glass, i.e. practically impermeable before fracturing. Once a new fracture occurs or a pre-existing fracture was activated, the mechanical resistance was completely removed and the permeability and the porosity were drastically increased. The permeability of the fracture element was roughly estimated to be 1×10^{-14} m² from the range of the fracture aperture up to ~ 10 μ m and a thickness of the (TOUGH2) flow elements along the fractures being about 10 times the actual fracture aperture.

The compressibility of the borehole domain including the notches, which represents the effective storage of the injection system, was calibrated to reproduce the injection pressure development in the actual experiment with a constant injection rate. The hydrological properties of model domains are listed in Table 3.1.

Table 3.1. Hydrological properties of matrix, fracture, and borehole domains.

		Permeability (m ²)	Porosity	Compressibility (Pa ⁻¹)
Matrix		0	0	0
Fracture	Pre-existing	0	0	0
	Activated	1×10^{-14}	0.8	1×10^{-8}
Borehole (notches)		1×10^{-9}	0.8	5×10^{-9}

Figure 3.10 presents the injection pressure evolutions within the borehole. The initial (linear) pressure increases are identical for both cases, because this represents fluid storage within the injection systems and borehole, which should be identical in the two cases. However, in the post-peak region, the case of injecting glycerol (red curve) displays a delay before pressure release and then exhibits a gradual pressure decrease. The simulations were terminated when the hydraulic fracture reached the specimen boundary, and the termination time was 1085 and 892.5 sec for glycerol and water injections, respectively. Fracture propagation speed was much slower when injecting glycerol, which can be also observed in the experiments. In both cases, the peak region has a kinked (oscillating pressure) plateau,

which was not observed in the experiment and was probably caused by abrupt change of hydrological properties from intact material when fractures sections were activated.

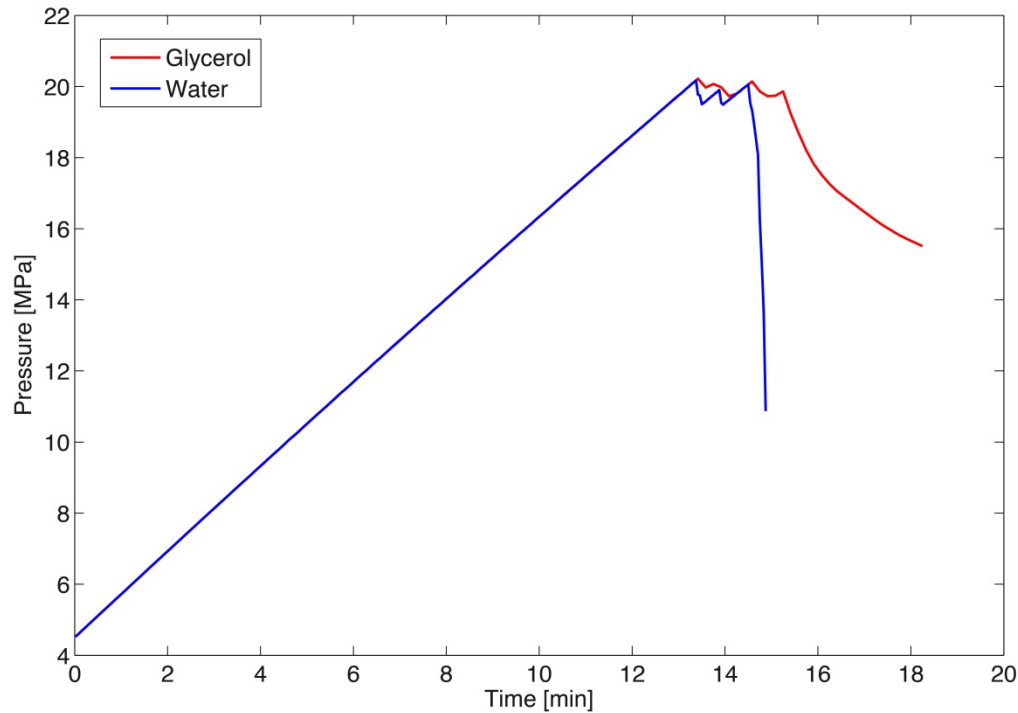


Figure 3.10 Pressure evolutions at the borehole for different fluid injections.

Figure 3.11 compares the pressure distributions, which were plotted at the final stage of fracturing processes. In the case of injecting glycerol (Figure 3.11a), the high injection pressure recedes with increasing distance from the borehole, which can be interpreted as existence of a gap between the crack tip and the fluid front. In contrast, for water injection (Figure 3.11b), the pressure is distributed uniformly along the fracture branches.

Figure 3.12 presents the final fracture patterns. The fracture propagation is overall perpendicular to the direction of the minimal principal stress with slight perturbation due to the local heterogeneity of pre-existing fractures. For both cases, the hydraulic fracturing paths partly follow the activated pre-existing fractures and are connected by newly generated fractures in the glass matrix. Distinctively, in the case of rapid fracture propagation with injecting water (Figure 3.12b), the hydraulic fracturing tends to activate the pre-existing fractures rather than break the intact matrix. See the portion of dark purple segments comparing to red segments along the fracturing paths. These characteristics are in the opposite way to the observation in the experiments.

These simulations were conducted with a fracturing model where its permeability was set to a high value once fracturing of a section occurred. An improvement to the model was later implemented in continuous changes in fracture hydraulic properties were modeling along with mechanical fracture opening and aperture changes, and using the cubic law for fracture permeability.

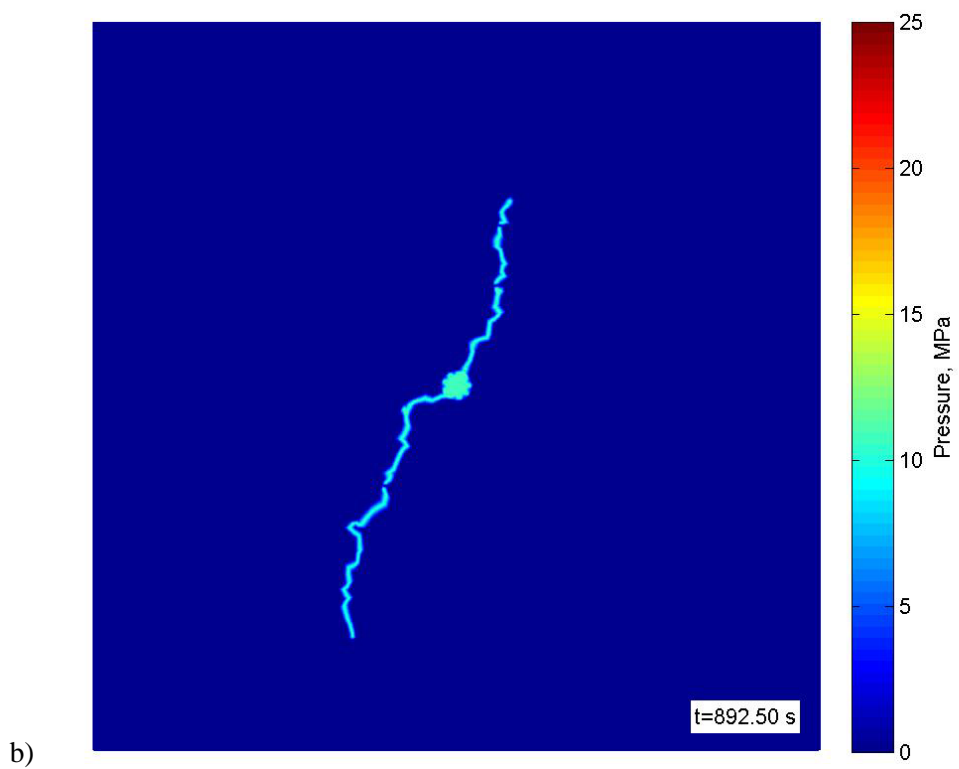
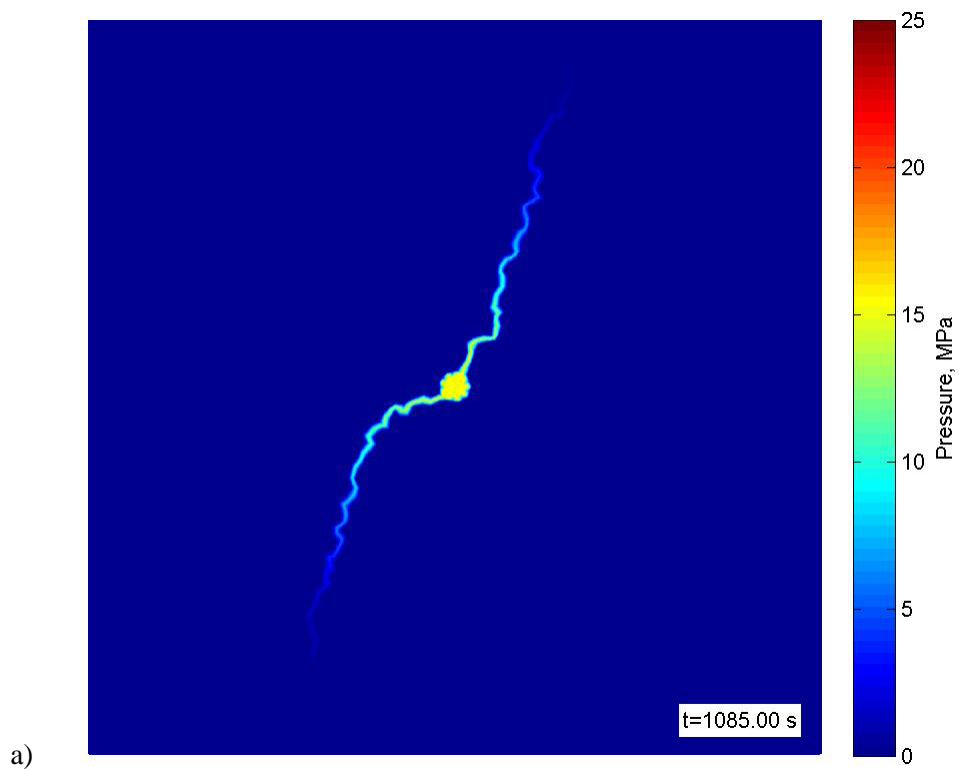


Figure 3.11 Contour plots of pressure distributions: a) glycerol injection; b) water injection.

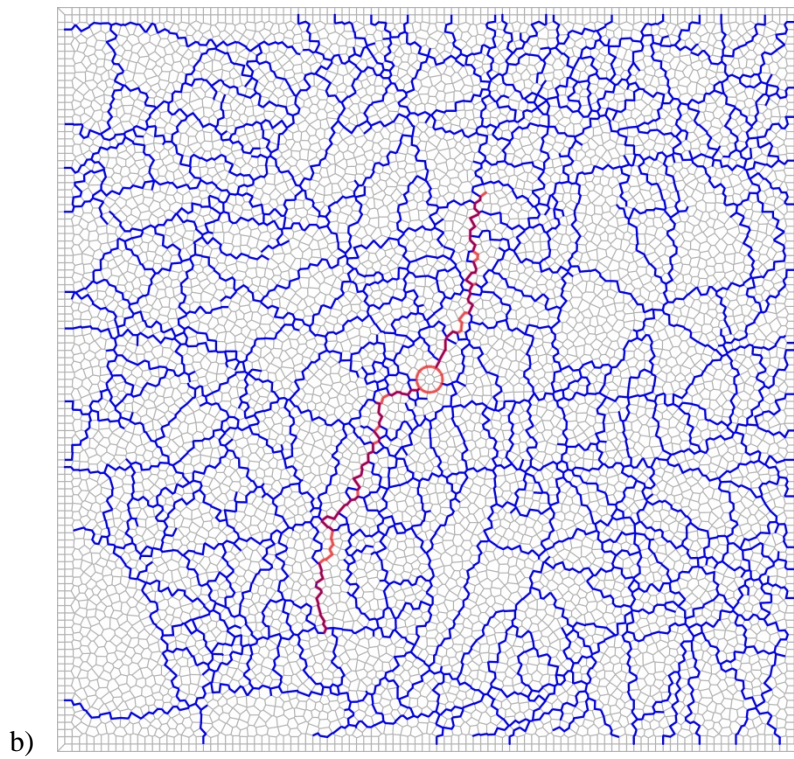
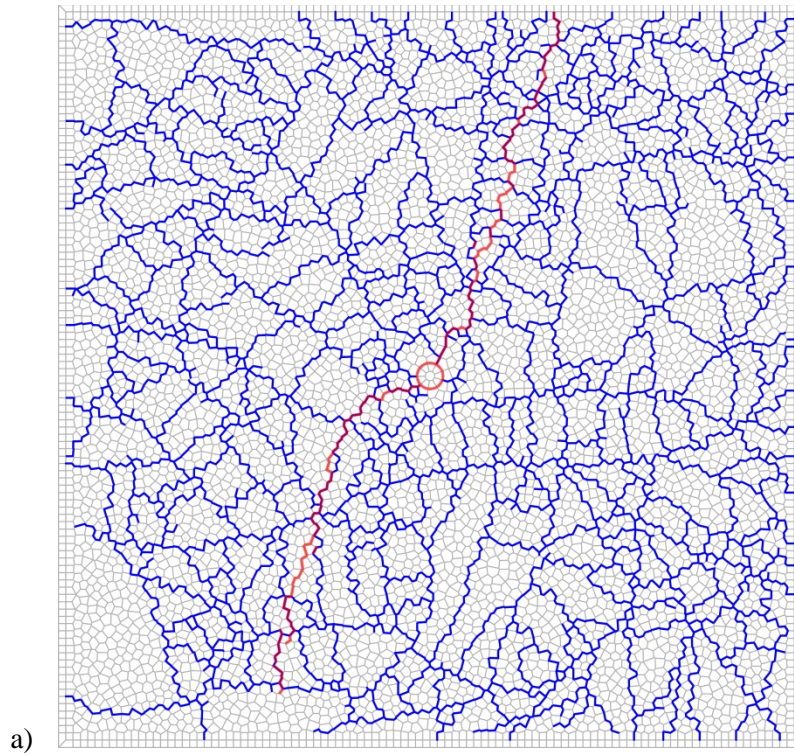


Figure 3.12 Hydraulic fracture patterns: a) glycerol injection; b) water injection.

2.2.5 Subtask 3.5 – Simulation of Mont Terri Hydraulic Fracturing Experiment (Phase II)

A hydraulic fracturing experiment conducted at the Mont Terri Rock Laboratory in Switzerland was included in this study as a possibility of applying the numerical simulator at an intermediate field scale. Thus we would use the numerical model developed and tested for small scale samples at an intermediate field scale.

Interpretation and analysis of field data

First we made new interpretations and analyses of the Mont Terri field data, including interpretation of measured mechanical and hydraulic responses and found indication of very complex behavior that is not consistent with propagation of a classical radial symmetric fracture. It was found that the volume of the injected fluid was much larger, around a factor 5 larger, than the apparent volume associated with the main fracture creation and opening. One possible explanation could be a substantial branching and damage around the main fracture that would provide a substantial amount of fluid storage. Because of the complexities revealed associated with the field experiment, and the difficulties to model these at the larger scale, we are still working on finding a good agreement between simulated and observed fracture behavior. One important feature added to the modeling was the modeling of the transient changes in permeability and fluid storage in the fracture plane with mechanical aperture changes. This was also one of the new lessons learned from the interpretative modeling of the laboratory experiments. A better representation of the hydromechanical behavior of the fracture and the fracture tip region would be needed and this may be required for an improved modeling of potential fracture branching.

The experiment that in this study is denoted “Mont Terri Hydraulic Fracturing Experiment” is part of the GP-A/GS experiments conducted at the Mont Terri URL some 15 years ago (Enachescu et al. (2002)). These experiments were conducted to study gas and water flow through fractures in Opalinus Clay and to observe longer term sealing of those fractures. However, the experiments included an initial creation and propagation of a fracture while monitoring the mechanical (displacement) and hydraulic (pressure) responses in nearby boreholes. The GP-A/GS hydraulic experiments are documented in a synthesis report by Enachescu et al. (2002), and additional interpretations are made in a paper by Daneshy et al. (2004). The main contribution of Daneshy et al. (2004) was the notion of non-ideal fracture geometry and behavior, including fracture propagation across bedding and fracture branching, and potential impact on the fracture flow and pressure responses.

We first conducted interpretations and analysis related to the injection behavior and fracture behavior by a close examination of transient pressure and displacement responses during water injection. A number of analytical models exist for analysis of fracture propagation. In this study, models of propagation of penny-shaped fractures are considered, including classical models by Perkins and Kern (1961) and Geertsma and de Kerk (1969). The model developed by Geertsma and de Klerk (1969) considers fracture propagation under fluid viscous dominated hydraulic fracturing conditions. Figure 3.13 shows a schematic of the penny-shaped radially propagating fracture according to Geertsma and de Klerk (1969). It is characterized by a logarithmic pressure decline from the injection borehole (not uniform), and a parabolic shaped fracture (not elliptic). Here, the model is rather used to match field observations in deformations and pressure and thereby used for estimating the extent and volume of

the created fracture. A model similar to that of Perkins and Kern (1961) is also used coupled with fracture mechanics of a penny-shaped fracture.

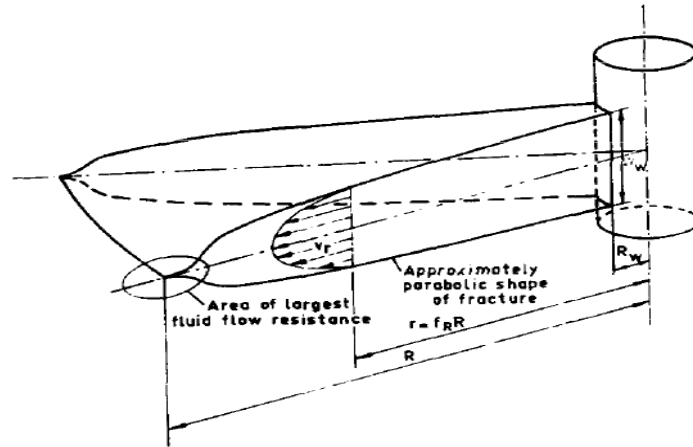


Figure 3.13. Schematic of a penny-shaped propagating fracture according to Geertsma and de Klerk (1969).

Figure 3.14 presents the borehole geometry and pressure responses in the injection borehole (BGS2) and the pressure monitoring borehole (BGS1) during the hydro-fracturing sequence. Figure 3.15 presents the evolution of injection pressure in BGS2 and deformation responses measured in boreholes BGS3 and BGS4, located respectively 0.7 and 1.4 m from the injection borehole. Breakdown occurs at an injection pressure of about 9 MPa, and this is followed by a sharp pressure drop to 7 MPa under continuous injection of about 1 l/min. A total of 3.7 liters was then injected at 1 l/min to extend the fracture. This was followed by 2 reopening cycles, using much smaller injection rates and injection volumes to avoid further fracture propagation.

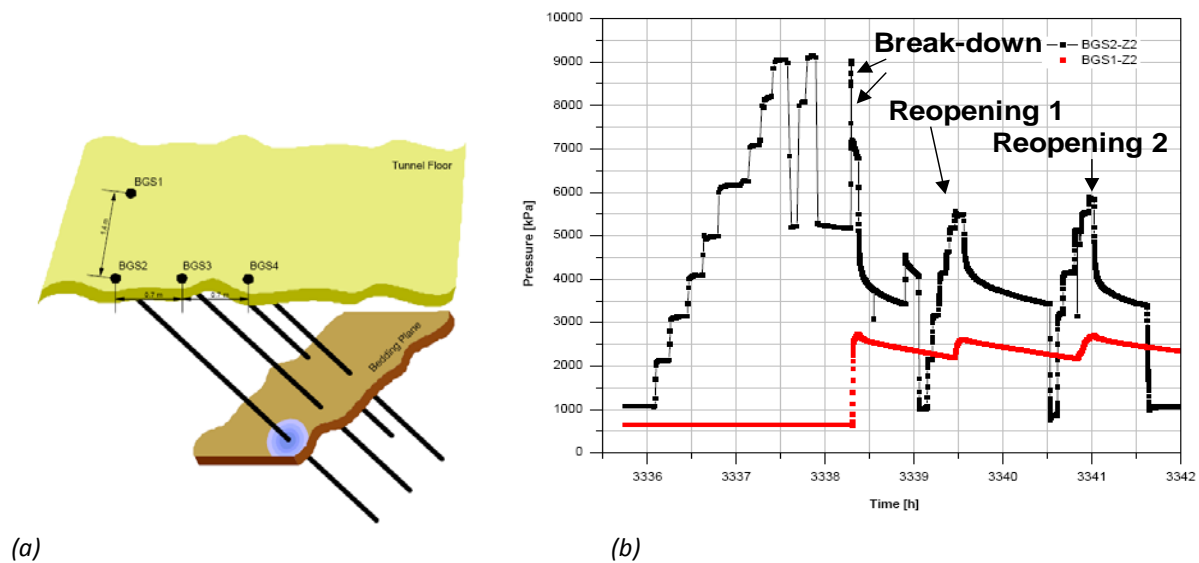


Figure 3.14. (a) Borehole layout at the GP-A/GS experiment and (b) pressure responses in the injection borehole section (BGS2-Z2) and the monitoring borehole section (BGS1-Z1) during breakdown and two reopening cycles (Enachescu et al. 2002).

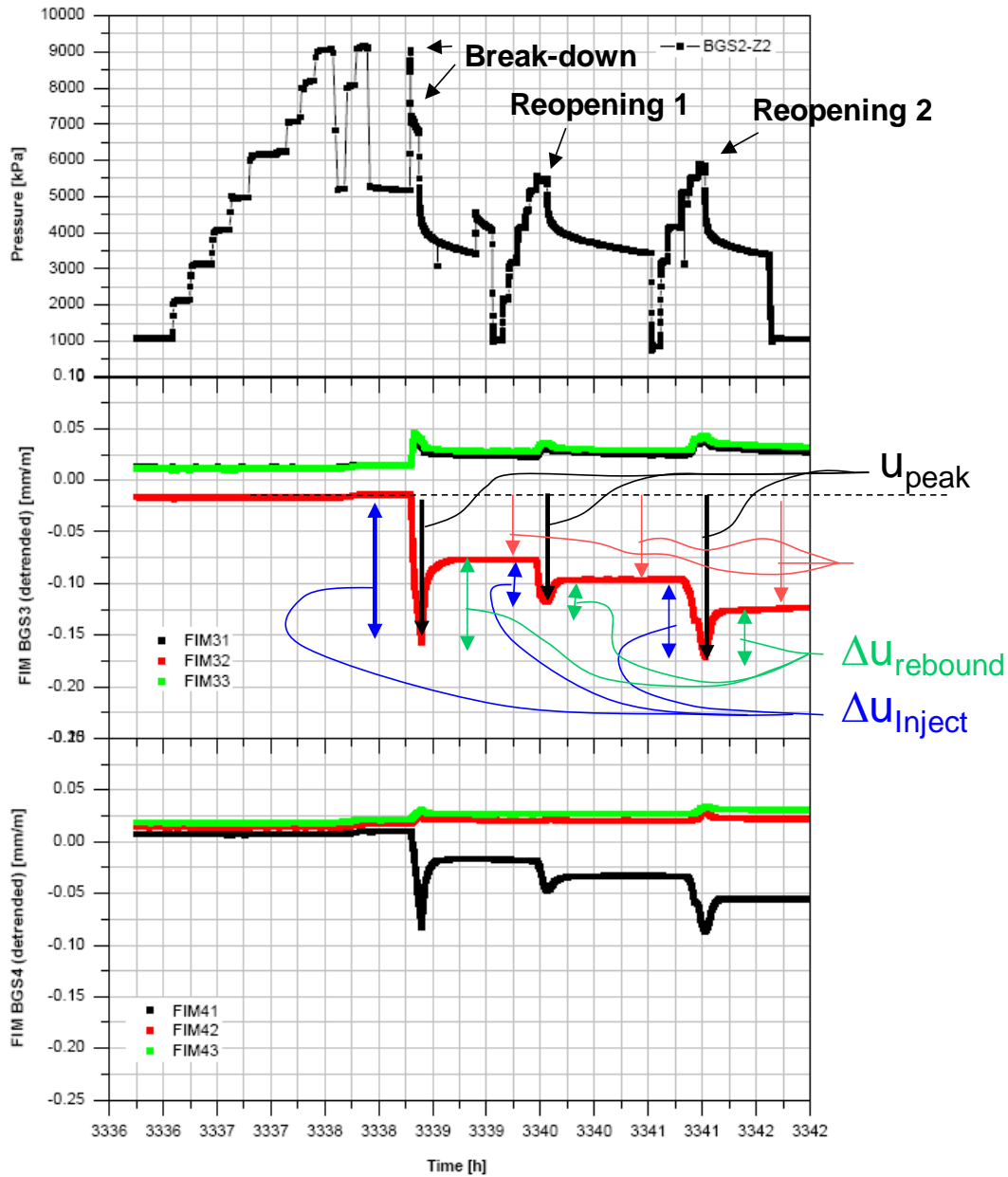


Figure 3.15. Evolution of pressure in BGS2-Z2 (injection interval) and deformations in BGS3 and BGS4 during breakdown and two reopening cycles (Enachescu et al. 2002).

The hydraulic responses in monitoring borehole BGS1 (red line in Figure 3.15) is apparent at breakdown and during the reopening cycles. Figure 3.16 also shows that there is a significant pressure drop from the injection well (BGS2) to the monitoring well (BGS1) indicating a low fracture hydraulic conductivity. Apparent from Figure 3.15 are the mechanical responses at breakdown and fracture reopening, and the residual aperture remaining even after releasing and completely venting the pressure in the injection borehole.

One of the key parameters we analyzed was the injection volume that could control the radius of the created fracture. In this section a rough estimate of fracture radius from injection volume is developed considering fracture mechanics and observations from the GP-A/GS hydro-fracturing. This is based on a detailed study of the mechanical response during the breakdown and fracture creation cycle (Figure 3.16). By noting the pressure and displacement responses in the monitoring boreholes (BGS1 for pressure, BGS3 and BGS4 for deformation) a picture of the general fracture response may be built. In Figure 3.15 some of the responses have been commented and estimated. For example, a sharp response in pressure was observed in BGS1 about 1 minute after breakdown. This shows that it took about 1 minute for the fracture to propagate to a radius of 1.4 m. The fracture deformations at that time may also be estimated from Figure 3.16. Using this information, fracture profiles were built, modeling the fracture propagation.

Another significant observation in Figure 3.16 is the pressure evolution in borehole Z1-2 located 1.4 m from the injection hole Z2-2. There were significant pressure changes induced in the injection borehole at around 190 to 200 seconds, even with a complete release of the well pressure after 200 seconds. Still the pressure in borehole Z1-2 remains elevated and constant showing the fluid pressure is trapped within the fracture. It indicates that the fracture is completely clogged near the injection well Z2-2. A possible explanation might be significant swelling of soft clays that could clog the fractures.

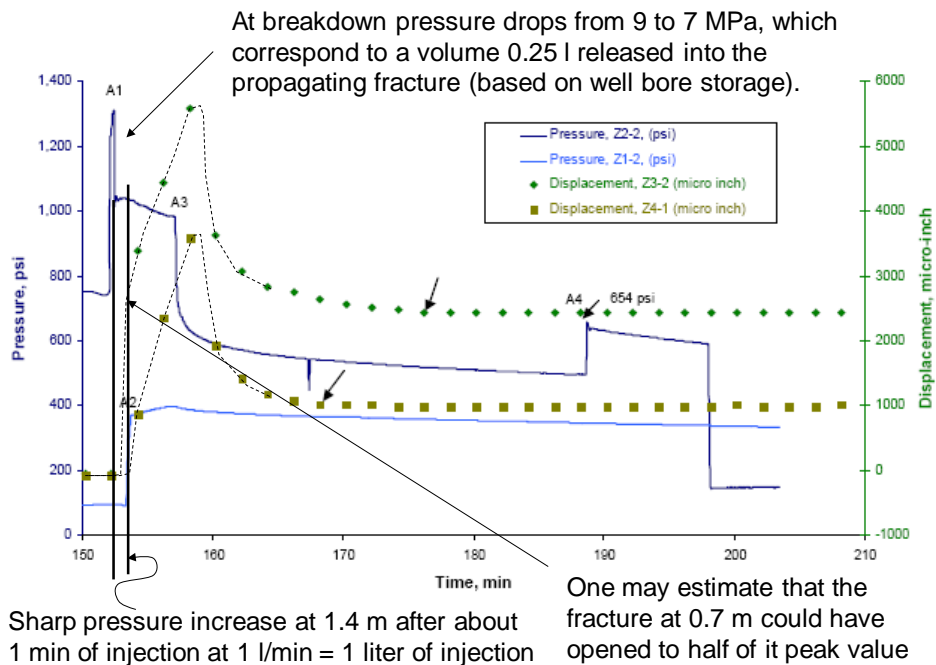


Figure 3.16. Details of pressure and deformation responses in the injection borehole BGS2 and the monitoring boreholes BGS1, BGS3 and BGS4 from Daneshy et al. (2004) here with some comments added.

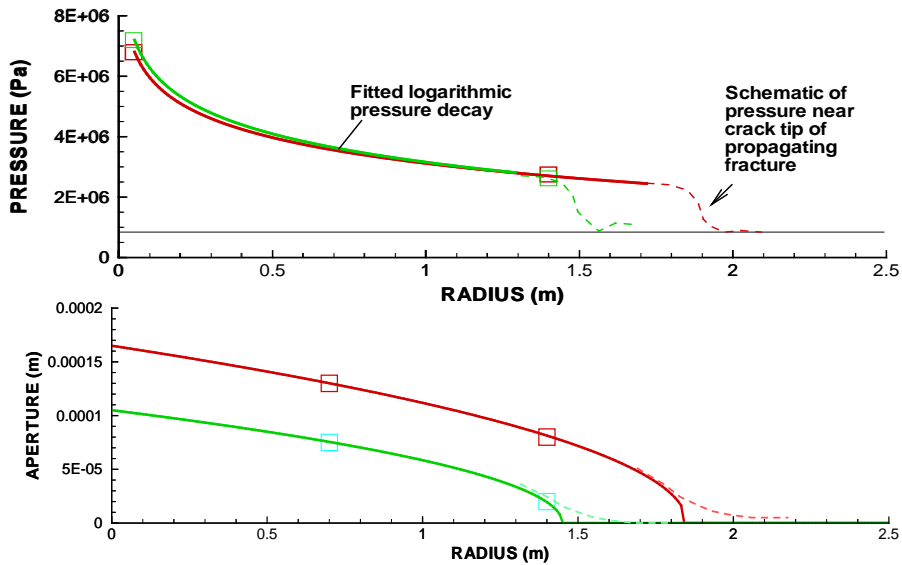


Figure 3.17. Pressure and aperture profiles constructed from the information in Figure 3.16.

For a penny-shaped fracture, two equations, one elastic equation relating radius to fracture volume and one equation relating radius to fracture mechanics parameters can be combined to yield the following expression for fracture volume:

$$V_{frac} = \frac{8\pi K_{IC}(1-\nu^2)r^{5/2}}{3E} \quad (3.1)$$

where K_{IC} is fracture toughness, $\nu = 0.3$ (Poisson's ratio), E is Young's modulus, and r is fracture radius. This equation relates fracture volume to fracture radius for a propagating fracture that is subject to a uniform internal fluid pressure. In this case, the pressure is not uniform so Equation (3.1) would be related to the pressure inside the fracture and not the pressure observed at the injection borehole.

Based on the observed injection and fracture volumes at the GP-A/GS experiments an empirical linear relationship between injected and created fracture volume was derived to be $V_{frac} = 0.24 + 0.1325 \cdot V_{inject}$. Using this empirical relation and Equation (3.1), with $K_{IC}/E = 2.0 \times 10^{-5}$ and Poisson's ratio = 0.3, the fracture radius can be estimated as: $r = 1.57 + 0.87 \cdot V_{inject}$. This relation between injection volume and radius is presented in Figure 3.18 together with created fracture volume. Figure 3.18 enables an estimate of what injection volumes it might take to create a fracture of sizable dimensions. We know from the GP-A/GS experiment that it took 5 liters of injection to create a fracture that is about 2 m in radius. To create a fracture of 3 m radius, an injection volume of about 15 liters would be required.

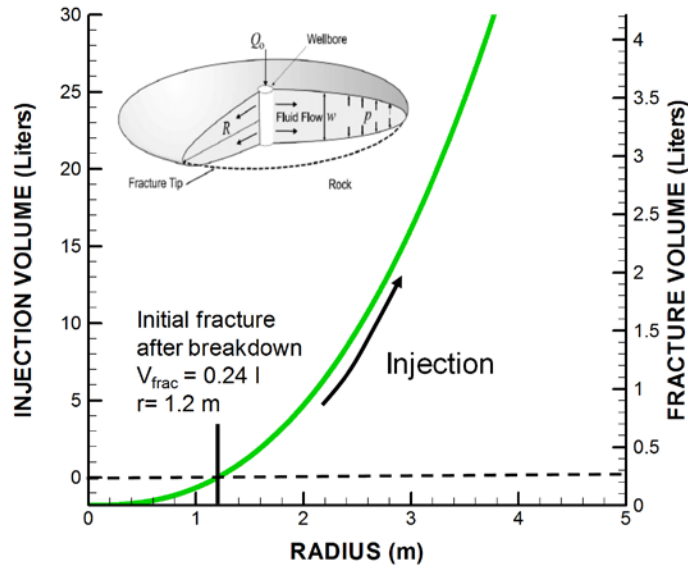


Figure 3.18. Empirical relation between injection volume and fracture length based on penny-shaped fracture mechanics model and observations at the GP-A/GS experiments.

Observation from the Mont Terri experiment also indicates fracture propagation offset from the main fracture path. Indeed, deformation measurements at the BGS4 borehole located 1.4 meters from the injection showed that the fracture had propagated offset the expected path along bedding. Daneshy et al. (2004) attributed the offset fracture growth pattern to branches consisting of tensile and shear fractures according to the conceptual model shown in Figure 3.19. The potential for shear slip along the created and opened fractures during active injection could certainly promote fracture growth offset the expected fracture propagation path. Shear may open up intersecting natural fractures which then will be pressurized with the injection fluid and propagated further.

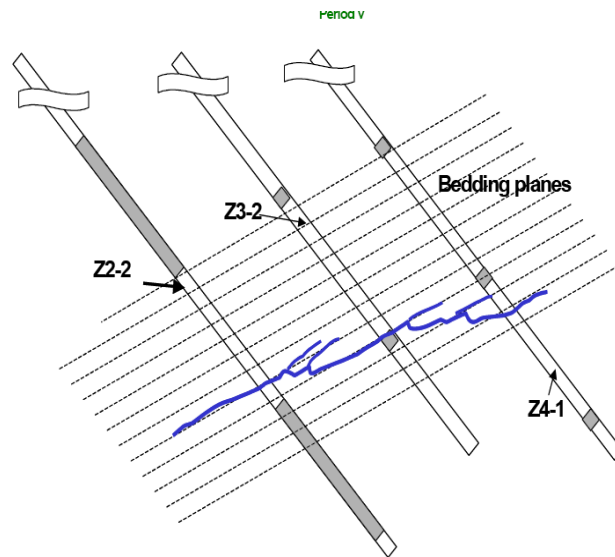


Figure 3.19. Conceptual model of possible cross-bedding fracture propagation at the GP-A/GS experiment (Daneshy et al. 2004).

TOUGH-RBSN modeling of fracture pattern

We have conducted TOUGH-RBSN modeling of fluid-driven fracture propagation through anisotropic medium (strength and elastic anisotropy) with properties of Opalinus Clay taken from the investigations at the Mont Terri URL. Using these parameters it turned out to be difficult to reproduce the fracturing pattern shown in the conceptual model in Figure 3.19. Estimates of the stress field that have been done at the Mont Terri rock laboratory have suggested that the maximum principal compressive stress is vertical. With such an assumption, the modeling indicates that fracture indeed can get cross-bedding fracture propagation; however, the fracturing will then to turn upwards towards the direction of the maximum stress rather than downwards.

With strength anisotropy and a dip of the bedding of about 35° , the fracturing can deviate downward from the bedding direction only if the maximum compressive stress is horizontal. Fig 3.20 shows one example in which the horizontal stress is assumed to be the maximum compressive stress. The dashed lines show the orientation of bedding planes which are oriented about 35° relative to the maximum (horizontal) stress. The results show some deviation of the fracture propagation from the bedding plane orientation; the fractures tend to be oriented more towards the maximum stress. The results in Figure 3-19 are shown for two different injection rate, with the injection rate in Figure 3.20a being 10 times that of the injection rate in Figure 3.20b. Both simulations show some damage developing around the main fracture.

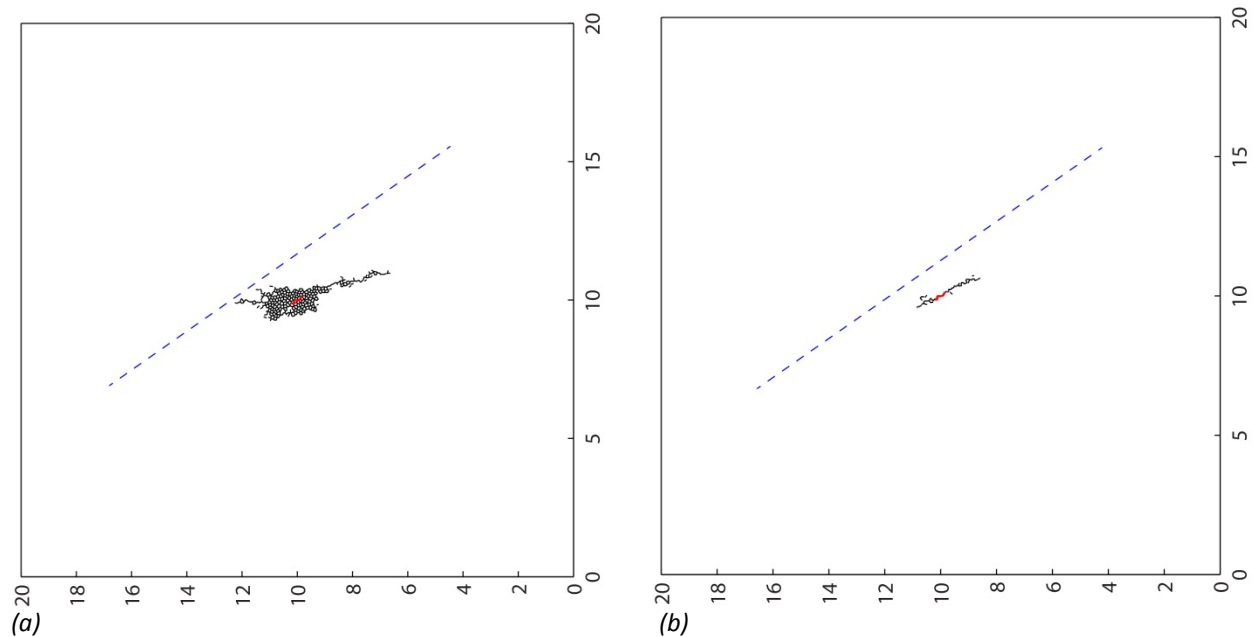


Figure 3.20. TOUGH-RBSN modeling of intermediate scale fracture propagation through an anisotropic medium. Dashed line shows direction of bedding planes. The injection rate is 10 time higher for the results shown in (a).

In addition to strength anisotropy as a result of bedding direction, there are also discrete shear discontinuities existing at Mont Terri. Most of these are oriented parallel to the bedding, but there are also smaller discontinuities oriented across the beddings. These have lower strength and therefore hydraulic fracturing might be channeled along these discontinuities. Figure 3.21 shows an example

where discrete shear discontinuities or bedding planes are inserted into the model. A small notch is placed along the bedding orientation at 35° from the horizontal axis, where the fluid injection is made. Three small defects are introduced on the possible fracturing path so that the hydraulic fracturing can turn and cross over to other bedding planes (Figure 3.21a). The defects have degraded strength parameters compared to the intact rock material. The confining stresses applied in this case are 4.5 MPa (vertical) and 5.5 MPa (horizontal), respectively.

Figure 3.21b shows the resulting fracture pattern. The fracture initiation is mainly affected by the inherent bedding orientation, where the early fracture propagates along the bedding direction. When the fracture hit the first crossing defect, the fracture is activated by the defect. Later, the fracture turns its front again parallel to the bedding direction. Due to the low injection rate, the simulation could not capture a further propagation of hydraulic fracture. There also exist fractures on the middle defect, which seem to be activated not by pressurized fluid, but by the surrounding stress conditions. Nevertheless, Figure 3.21 shows one possible example in which fracturing could be deviated and cross the boreholes at locations observed in the field.

From the simulations above, it is indicated that the stress conditions and discrete discontinuities affect fracture propagation more than the inherent anisotropic properties of geological formations. The strength anisotropy can dominate the fracturing characteristics in specific cases, but our simulations show that for the conditions and properties corresponding to these hydraulic fracturing experiments, the strength anisotropy is not enough to determine the fracture propagation.

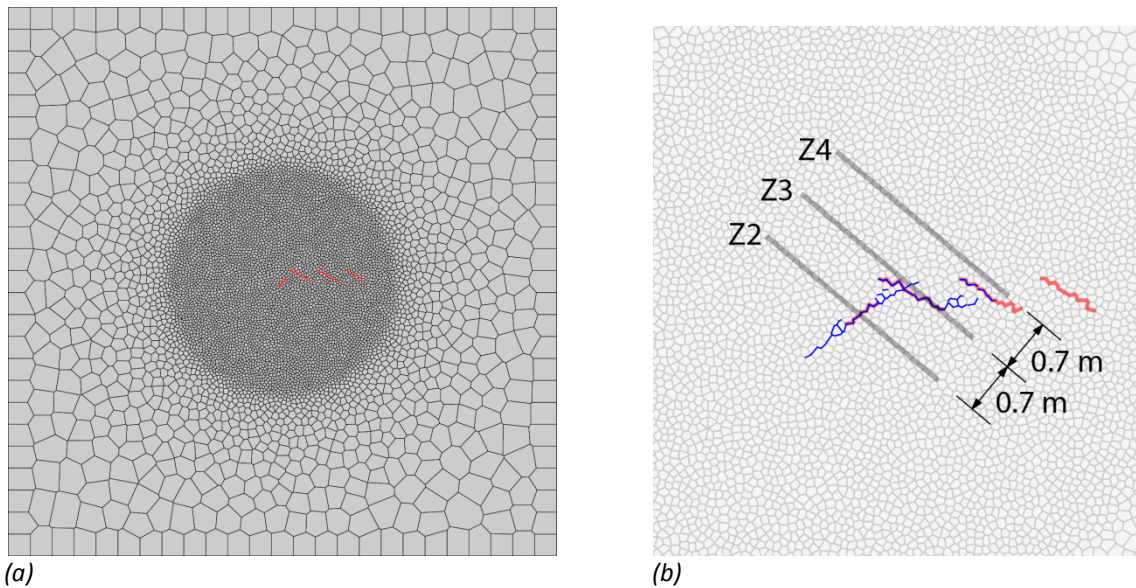


Figure 3.21. (a) Model discretization with prescription of discontinuities; (b) Resulting hydraulic fracture propagation overlaid onto the Voronoi grid.

2.3 Task 4.0 – Final Synthesis of Experimental and Numerical Modeling Results (Phase II)

In this task, the experimental and numerical modeling results are synthesized in terms of findings related to the fundamental processes of hydraulic fracture propagation in complex, anisotropic, and heterogeneous rock.

2.3.1 General remarks on the agreement and discrepancies between the laboratory experiments and numerical modeling

The numerical modeling results of fluid driven fracturing in heterogeneous low permeability medium with the TOUGH-RBSN code was consistent with that of the experiments showing that

- A pre-existing notch at the borehole wall will lower peak (fracturing) pressure and help to control the rate of fracture propagation
- A small volume injection system of small water storage will also help to control the rate of fracture propagation
- The fracture propagates along the direction of maximum principal stress and preferable along pre-existing fractures when they are weak, though could also cross intact rock parts

The numerical modeling results were not in complete agreement with experimental data related to the effect of injection rate and fluid viscosity. While the experimental data indicated more complex branching fracturing for low rate and high viscosity, the numerical modeling indicated that fractures dominantly follows one main path regardless of injection rate and viscosity. Moreover, the modeling did not indicate as dramatic difference in the peak pressure depending on viscosity. This indicates that the modeling did not capture correctly the fluid flow and deformation behavior at the crack tip. Apparently, in the experiment the high viscosity glycerol could not easily penetrate all the way to the crack tip, or showed much more resistance to flow then was captured in the modeling. In the modeling the only difference in modeling the two fluids was to increase the viscosity by a factor of 1000. With the 1000 times increase in fluid viscosity, the modeling showed that the fluid could still penetrated all the way crack tip as the injection took place over tens of minutes. There might be other processes providing shear resistance for the high viscosity glycerol to penetration through the very thin fractures in the glass sample which were not captured in the modeling.

The analysis and modeling for Mont Terri hydraulic fracturing experiments showed the following:

- The inferred fracturing path from the experiment could only be modeling if considering that fracture propagation follows pre-existing fractures or minor shear faults and other discrete fractures, whereas the strength anisotropy of intact Opalinus Clay could not explain the observed direction of fracture propagation.
- After active injection, once the well pressure is released the fracture flow ceased completely from hydraulic view point, which indicted significant effect of swelling clay that clogged the fractures.

In the current TOUGH-RBSN model, effects of matrix swelling on the fracture permeability is not considered and it is therefore not possible to model the pressure and flow behavior in detail. Adding such capabilities will be essential for modeling the long term behavior of fractures in ductile clays.

2.3.2 Remarks on fluid injection rate and hydraulic fracturing

Aside from the numerical modeling, laboratory experiments demonstrated that the injection rate of highly viscous fluids into rock (analogues) containing a large population of preexisting fractures can result in dramatically different fracture geometry. Slow injection of viscous fluid primarily activates partially open and weak fractures (hydroshearing), resulting in a wide distribution of the fracturing fluid in the rock, while fast injection produces well-defined, planar hydraulic fractures by fracturing intact rock matrix. (Note that these differences are the opposite of the dynamic fracturing using explosives and propellant, where faster application of gas pressure to the rock results in larger number of shorter fractures [or rock fragments] near the well.) This effect is possibly caused by the difference in the fluid pressure within a propagating hydraulic fracture. During slow injection, high fluid pressure near the leading edge of a hydraulic fracture can open intersecting fractures and weaknesses in rock. In contrast, the low fluid pressure near the tip of a hydraulic fracture produced by fast injection cannot activate them but the fracture propagates because of the “wedging” of the fluid in the fracture results in tensile stress concentration in the rock ahead of the fracture.

This result indicates a possibility of manipulating the geometry of subsurface fluid drainage footprint by altering the geometry of hydraulic fractures with varying fluid injection rate.

2.3.3 Remarks on the scaling—Applying laboratory experiments to the field, and changing scales in the numerical modeling.

In both laboratory experiments and numerical simulations, the test parameters need to be selected carefully so that the behavior of the hydraulic fracturing corresponds to fracturing in the field at an appropriate scale. This is particularly difficult for laboratory experiments in which the test capability and material properties limit the scales that can be properly simulated.

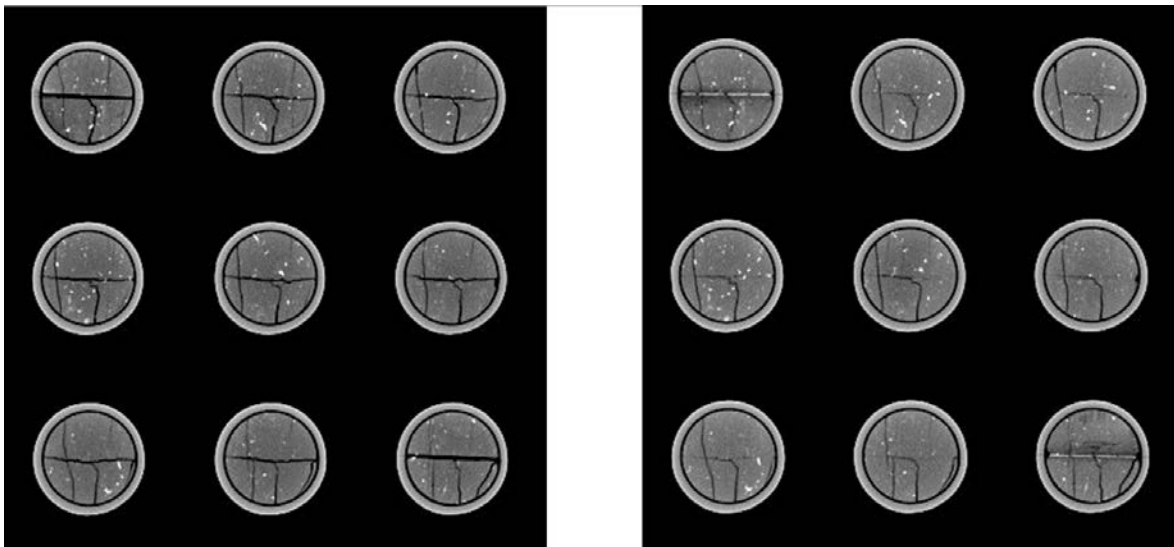
De Pater et al. (1994a,b) describe how the scale of field hydraulic fractures can be determined corresponding to laboratory experiments, for a limited set of experimental parameters such as borehole diameter, rock elastic moduli, fracture toughness, fluid viscosity, stress, rock permeability (leakoff), injection rate, and the test duration. This is based upon assumed, simple, circular plane fracture geometry. Five fundamental dimensionless parameters are identified (dimensionless time, crack energy, elastic deformation, leakoff, and confining stress parameters). In our lab and numerical experiments, the leakoff parameter was neglected, because of the small matrix permeability. An example of corresponding laboratory test conditions and field conditions are shown in Table 4.1. The analysis revealed that direct laboratory simulations of a reservoir-scale hydraulic fracturing is difficult for physically realizable test conditions in our laboratory samples, limiting the applicable sizes of the rock volume in the field (~1.7m block in this example). Therefore, for that purpose, numerical modeling must be employed to investigate the fracture behavior.

Table 4.1. An example of matched experimental conditions at different scales

	Young's modulus	Fracture toughness	Experiment time	Injection rate	Fluid viscosity
Lab (10 cm glass cube)	72 GPa	0.75 MPa m ^{0.5}	2 min	0.4 mL/min	1000 cP
"Field" (1.7m rock cube)	36 GPa	1.5 MPa m ^{0.5}	2 min	18.5 mL/min	500 cP

2.3.4 Remarks on fluid-sensitivity and swelling of shale

Our current numerical modeling does not consider time-dependent or fluid chemistry dependent behavior of shale. Clay-rich shales (particularly, swelling clays such as smectite and mixed-layer illite) exhibit ductile behavior and swelling of the rock matrix, which results in closure of hydraulic fractures and permeability losses. X-ray CT images in Figure 4.1 show experimentally observed fracture closure during exposure to brine in an Opalinus Clay core from Mont Terri URL. Although the amount of the swelling clay is much smaller, we also observed swelling-induced fracturing in relatively competent and strong Mancos shale block during the core preparation, causing severe problems in sample preparation. During hydraulic fracturing and following production of oil and gas from shale fractures, swelling and time-dependent deformation of shale can have a significant impact on the effectiveness of the fracturing operation and the sustainability of the permeability in the produced fractures.



(a) Before brine injection

(b) After brine injection

Figure 4.1. Swelling and fracture closure in a pre-fractured Opalinus Clay core sample. X-ray images of core cross sections are shown. Core length=4 inches (10.24 cm). The injected fluid is a synthetic in-situ brine. The vertical fractures in the core (which did not close in the after-injection images) are filled with epoxy (which do not show in the X-ray images because of its low density).

3. Publications and presentations (incl. planned)

Kim, K., J. Rutqvist, S. Nakagawa, J. Houseworth, and J. Birkholzer. 2015. Discrete modeling of hydraulic fracturing processes in a complex pre-existing fracture network, Fall American Geophysical Union Meeting, MR41A-2626, San Francisco December 14-18.

Kim, K., J. Rutqvist, S. Nakagawa, J. Houseworth, and J. Birkholzer. 2015. Simulations of fluid-driven fracturing within discrete fracture networks using TOUGH-RBSN, TOUGH Symposium 2015, Berkeley, September 28-30.

Kim, K., J. Rutqvist, S. Nakagawa, and J. Birkholzer. TOUGH-RBSN modeling of hydraulic fracture propagation within discrete fracture networks, Computers & Geosciences, In preparation.

Nakagawa, S., T.J. Kneafsey, and S. Borglin. 2015. Laboratory Visualization of Hydraulic Fracture Propagation and Interaction with a Network of Preexisting Fractures, Fall American Geophysical Union Meeting, MR41A-2615, San Francisco, December 14-18.

NOTE: The paper for which an abstract was generated for the ARMA/US Rock Mechanics Symposium was not submitted. Instead, an invited presentation on the laboratory experiments conducted in this project is planned to be given at the Geological Society of America meeting in Denver 25-28 September 2016 (<http://community.geosociety.org/gsa2016/home>).

4. Budget summary

Below is the spending for the entire period of the project including both Phase I and II.

LBNL PID	Activity	Activity Name	Total Project Budget (TPB)	Oct	Nov	Dec	Jan	Feb	Mar	Apr	May	Jun
102971	001	ES_Laboratory Hydraulic Frac	187,100	1,443	9,680	2,986	9,180	17,901	10,761	12,542	14,289	9,621
		Labor		1,443	9,680	2,885	8,381	7,638	10,728	10,800	14,119	9,621
		Procurement		-		85	799	10,263	33	1,742	170	
		Misc		-		16						
102971	002	ES_Modeling Hydraulic Frac	155,900	-	5,533	2,986	1,214	12,784	10,368	19,041	6,632	16,132
		Labor			5,533	2,986	1,214	12,784	10,368	19,041	6,632	16,132
		Procurement										

Jul	Aug	Sep	Oct	Nov	Dec	Jan	Feb	Mar	Apr	May	Jun	Total Spent to Date	Total Received	Amount remaining
3,428	2,095	2,801	10,475	12,937	4,885	16,338	13,067	16,187	-	4,216	12,190	187,022	187,100	78
3,355	2,095	2,841	9,787	12,347	4,698	12,810	13,054	16,187	-	4,216	12,190			
73		(40)	688	590	187	2,893	13							
						635								
3,650	5,364	4,562	4,592	3,456	6,313	5,345	26,330	14,414	-	(179)	7,275	155,812	155,900	88
3,650	5,364	4,562	4,592	3,456	6,313	4,740	26,330	14,414	-	(179)	7,275			
						605								

5. References

- Daneshy A., Blümling P., Marschall P., and Zuidema P. (2004) Interpretation of field experiments and observation of fracturing process. Paper presented at the SPE International Symposium and Exhibition on Formation Damage Control, Lafayette, Louisiana, U.S.A., 18–20 February 2004. Society of Petroleum Engineers, SPE 86486.
- de Pater C.J., Cleary M.P., Quinn T.S., Barr D.T., Johnson D.E., Weijers L. 1994a. Experimental verification of dimensional analysis for hydraulic fracturing, *SPE Prod & Fac*, 9(4),230-238.
- de Pater, C.J., L. Weijers, M. Savic, K.H.A.A. Wolf, P.J. van den Hoek, and D.T. Barr. 1994b. Experimental study of nonlinear effects in hydraulic fracture propagation, *SPE Prod & Fac*, 9(4),239-248.
- Enachescu C., Blümling P., Castelao A., and Steffen P. (2002) Mont Terri GP-A and GS Experiments Synthesis Report. NAGRA NIB 02-51.
- Geertsma J., and de Klerk F. (1969). A rapid method of predicting width and extent of hydraulically induced fractures. *Journal of Petroleum Technology*, (December 1969), 1571-1581.
- Perkins T.K. and Kern L.R. (1961) Widths of hydraulic fractures. *Journal of Petroleum Technology* (Sept., 1961) 937-949.
- Rasband, W. S. (2016). *ImageJ*, U. S. National Institutes of Health, Bethesda, Maryland, USA. 1997-2016.